NASA Contractor Report 182121

Propfan Test Assessment Testbed Aircraft Stability and Control/Performance 1/9-Scale Wind Tunnel Tests

B. H. Little, Jr., K. H. Tomlin, A. S. Aljabri, and
C. A. Mason

Lockheed Aeronautical Systems Company
Marietta, Georgia

May 1988

Prepared for
Lewis Research Center
Under Contract NAS3-24339

National Aeronautics and
Space Administration

(NASA-CR-182121) PROPFAN TEST ASSESSMENT TESTBED AIRCRAFT STABILITY AND CONTROL/PERFORMANCE 1/9-SCALE WIND TUNNEL TESTS Final Report (Lockheed Aeronautical Systems Co.) 157 p CSCL 01C G3/05

N88-26360

Unclas
0149521

FOREWORD

These tests were performed in three separate NASA wind tunnels and required the support and cooperation of many NASA personnel. Appreciation is expressed to the management and personnel of the Langley 16-Ft Transonic Aerodynamics Wind Tunnel for their forbearance through eight long months, to the management and personnel of the Langley 4M x 7M Subsonic Wind Tunnel for their interest in and support of the program, and to the management and personnel of the Lewis 8-Ft x 6-Ft Supersonic Wind Tunnel for an expeditious conclusion.

This work was performed under Contract NAS3-24339 from NASA-Lewis Research Center. This report is submitted to satisfy the requirements of DRD 220-04 of that contract. It is also identified as Lockheed Report No. LG88ER0056.

TABLE OF CONTENTS

PRECEDING PAGE BLANK NOT FILMED

TABLE OF CONTENTS (CONTINUED)

TABLE OF CONTENTS (CONTINUED)

LIST OF FIGURES

PRECEDING PAGE BLANK NOT FILMED

LIST OF FIGURES (CONTINUED)

LIST OF FIGURES (CONTINUED)

LIST OF FIGURES (CONTINUED)

LIST OF FIGURES (CONTINUED)

1.0 SUMMARY

Full-span wind tunnel model tests at 1/9-scale were performed to establish safety of flight and performance predictions for the PTA aircraft. Semispan model tests at the same scale were performed to measure flow field properties (local velocity and flow angularity) in the regions where the propfan operates. To understand and be able to scale data from the powered model tests, the 1/9-scale SR7L propfan rotor was also tested on an isolated nacelle.

The safety of flight and performance data were taken in the NASA-Langley 4M x 7M Subsonic Wind Tunnel at Mach 0.167 and 0.2 and in the NASA-Langley 16-Ft Transonic Aerodynamics Wind Tunnel at Mach 0.4 to 0.85. The flow survey data were taken in the NASA-Lewis 8-Ft x 6-Ft Supersonic Wind Tunnel at Mach 0.6 to 0.85. Reynolds numbers based on MAC ranged from approximately 0.2×10^6 to 5×10^6.

The models were full-span and sting-mounted for all tests except the high-speed flow survey tests. For the latter, the model was modified to a half-fuselage, semispan configuration and mounted from the tunnel side wall.

Major emphases in the flight safety/performance tests were on wing surface pressure distributions and aerodynamic forces and moments. The general philosophy of these tests was to obtain data from the GII airplane model for a baseline and establish increments from that baseline as the PTA installation was built up. These increments were then applied to established GII flight test data to predict PTA performance.

As expected, the addition of the PTA hardware to the GII aircraft:

- Increased drag significantly
- Increased wing lift and nose-up pitching moment (thereby slightly reducing pitch stability
- Increased side force due to sideslip
- Decreased yawing and rolling moments due to sideslip
- Slightly affected rudder and elevator effectiveness
- Significantly reduced roll control power
- Reduced maximum lift coefficients

Generally, wind tunnel data were predicted with good accuracy by the inviscid panel code QUADPAN. This was true not only of model forces and moments and surface pressure distributions but also of the flow field properties off the surface in the region of the propfan.

These model tests, together with supplementary QUADPAN analyses, provided the data to verify from stability, control, handling, and performance standpoints that the proposed PTA aircraft would be a suitable vehicle for flight research tests of the large-scale SR-7L propfan.

2.0 INTRODUCTION

The NASA-Lewis Propfan Test Assessment (PTA) Program was initiated in 1984 to develop and fly a testbed aircraft for evaluation of the Large-Scale Advanced Propeller (LAP) already under development at Hamilton Standard. A contract was awarded to the Lockheed-Georgia Company for the design and modification required to convert a Gulfstream Aerospace Corporation GII aircraft to the PTA configuration. The PTA configuration proposed consisted of installation of an engine nacelle on the left-hand wing of the GII, addition of an acoustic instrumentation boom outboard of the nacelle, and addition of wing tip booms for static and dynamic balance. These modifications in turn required configuration changes such as deactivation of some wing spoiler panels.

To assure safety of flight and validate performance predictions of the PTA aircraft, small-scale wind tunnel tests were planned. Tests were needed at low-speed flight conditions and at speeds up to Mach 0.85. Force and moment data were needed for performance and handling qualities evaluation, and surface static pressure data were needed to explain flow phenomena and validate loads predictions.

A major objective of the PTA Program is to measure vibratory stresses on the LAP rotor blades in flight and compare them with predicted values. Since the first step in the blade stress prediction process is to predict the blade flow environment, a further objective of the small-scale tests was to measure flow field data in the vicinity of the propfan rotor and compare those data with predicted values.

A new 1/9-scale model was built for these tests. Maximum scale was limited by the sizes of available wind tunnels and minimum scale by the difficulties of modeling small propfan rotors and drive systems. The 1/9-scale set the rotor diameter at one foot and resulted in a model small enough to fit into several suitable wind tunnels. For all except the flow survey tests, the model was sting mounted with compressed air brought aboard the model through the sting to power the air motor that drove the propfan. Availability of drive motors made it desirable to test the model with propfan on the right hand wing instead of the left hand as in full scale. This, however, creates no problems since a mirror image configuration of the full-scale aircraft was always used in the scale-model tests.

Tunnel availability time did not permit obtaining flow field data in the full-span, high-speed wind tunnel tests. Therefore, a second series of high-speed tests were performed in a smaller wind tunnel specifically to obtain flow field data. For these tests, a new half-fuselage was built, and a semispan model was assembled from parts of the full-span model.

The high-speed wind tunnel tests were conducted in the NASA-Langley 16-Ft Transonic Aerodynamics Wind Tunnel in the summer and fall of 1985. Low-speed tests were performed in the NASA-Langley 4M x 7M Subsonic Wind Tunnel in the summer of 1986. The high-speed flow survey tests were performed in the NASA-Lewis 8-Ft x 6-Ft Supersonic Wind Tunnel in January 1987. Test Mach numbers ranged from 0.16 to 0.85. Reynolds numbers, based on MAC, ranged from 0.2×10^6 in the low-speed wind tunnel to 5×10^6 in the high-speed wind tunnels.

PRECEDING PAGE BLANK NOT FILMED

All of the data collected in these tests have been stored in informal reports at the Lockheed Aeronautical Systems Company - Georgia as part of the PTA documentation.. This report presents analyses of those data and the major results from those tests. Where appropriate, the data are compared with predicted values from analytical codes. In the case of the flow field data, a major emphasis is placed on the correlation of experimental data with analyses and modification of the analytical methods needed to produce good correlation.

3.0 TEST APPARATUS

3.1 WIND TUNNEL MODELS

3.1.1 High-Speed Tests

A photograph of the sting-mounted, high-speed model assembly, as installed in the NASA-Langley 16-Ft Transonic Aerodynamics Wind Tunnel, is shown in Figure 1.

A cylindrical fairing was attached to the aft portion of the model as shown in Figure 2 to accept the support sting. This sting fairing method is commonly used in this facility and was recommended by facility personnel as the best method of minimizing sting attachment corrections.

The model was designed to measure propfan acoustics data as well as aerodynamics data. One wing contained an array of acoustics transducers and the other an array of pressure orifices. The propfan drive motor that was available at the start of the program and the matrix of propfan rotation directions desired in the tests made it expedient to dedicate the left-hand wing to acoustics instrumentation and the right-hand wing to pressure instrumentation. The aerodynamic data, therefore, are for a configuration that is a mirror image of the PTA configuration--that is, the nacelle is mounted on the right-hand wing instead of the left. In the tests, the tip booms (which are different for left and right wings) and the acoustic boom were always arrayed to maintain the mirror image configuration.

Dimensions and contours of the basic GII configuration were obtained from loft drawings provided by Gulfstream Aerospace. The 1/9-scale model thus derived had a wing span of 2.337m (92 inches) and length (to the end of the sting fairing) of 2.354m (92.67 inches). Model weight was approximately 544 kg (1200 pounds). Wing area was 0.918 m^2 (9.877 ft^2), and the MAC was 0.416m (16.364 inches).

Figure 3 presents cross sections through the fuselage to show the balance, compressed air ducts for the propfan drive motor, scani-valve locations, and other details of model construction. The balance, of course, separated the metric and non-metric parts of the model assembly.

Air for the drive motors flowed through the center of the sting, exited the sting through ports on either side of the adaptor at point (1), flowed through bypass lines around the balance (Section B), and into the forward plenum at point (2) (Section A). From the forward plenum, the air supply could be ported to either/or both wing root regions, then through passages in the wing to the propfan nacelles.

Scani-valves for pressure measurements were located in the nose portion of the model. Power and signal leads from the scani-valves passed loosely around the balance and were taped to the external surface of the sting to exit the test section.

The right-hand wing was fitted with an aileron that could be set at zero and ±10 degrees deflection by means of fixed brackets. An outboard spoiler (the only one active on the PTA aircraft) was provided with deflection angles of 10 and 35 degrees.

The PTA nacelle was constructed so that nacelle tilt angles of +2, -1, and -3 degrees could be simulated. On the PTA airplane the nacelle

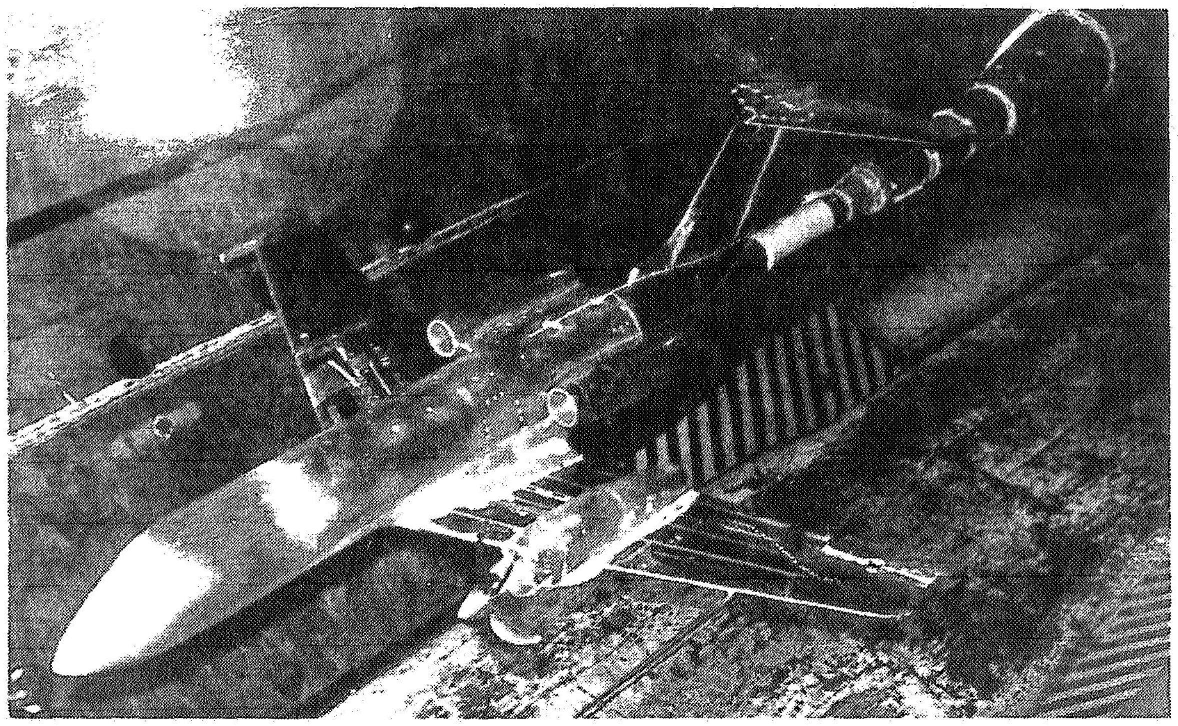

Figure 1. High Speed Model in 16' Transonic Tunnel

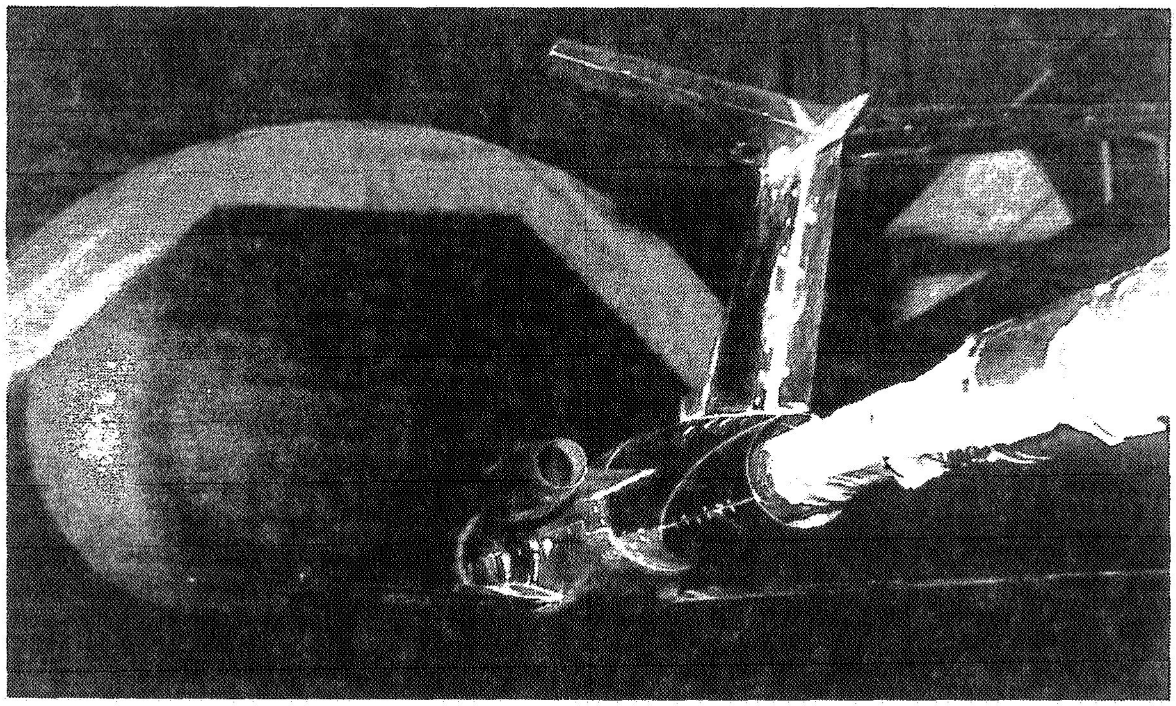

Figure 2. Sting Fairing - High Speed Model

ORIGINAL PAGE IS
OF POOR QUALITY

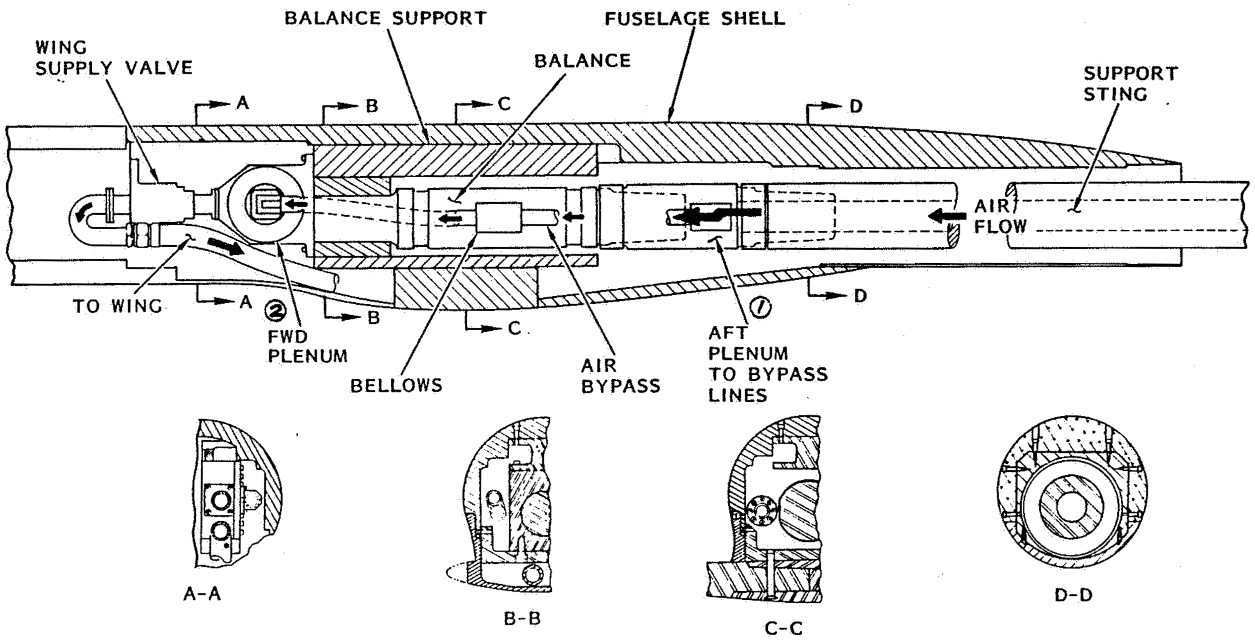

Figure 3. Fuselage Cross Sections - High Speed Model

breaks at the interface between the Quick-Engine-Change (QEC) assembly and the aft nacelle so that only the QEC is tilted. This was too difficult to model, however, because of the requirement for compressed air to a plenum in the model nacelle that extends fore and aft of the QEC break. Therefore, on the model the entire nacelle was tilted by putting wedges between the wing and the nacelle. On the model, the full-scale aft nacelle was simulated only for nacelle tilt of +2 degrees and was raised above the true full-scale position for -1 degree and -3 degrees. The nacelle pivot point on the model, however, was the same as for the airplane so that the forward nacelle (and propfan position) was properly simulated at all tilt angles.

The PTA nacelle contained a force balance between the drive motor and the propeller hub so that forces and moments on the propeller could be measured.

The horizontal stabilizer was made so that it could be positioned at incidence angles of 0, -1.5, -3, and -5 degrees. In addition, elevator deflection angles of +5, +10, -15, -20, and -25 degrees could be set. The rudder was made so that it could be set at deflection of ±5, ±10, ±15, ±20, and ±25 degrees.

Throughout the design phase of the PTA Program, there was concern that unforeseen and unpredictable transonic drag associated with the PTA nacelle installation might prevent attainment of the desired high-speed test conditions. To insure against this, a design study was performed to devise configuration changes that could be tested in the wind tunnel and then applied to the aircraft if needed. The most promising modification for dealing with excessive drag emerged as a wing leading edge extension (LEX) on the inboard side of the nacelle. This device was designed to extend the leading edge and camber it so that the upwash induced by propeller slipstream swirl would not result in excessive velocity peaks on the wing. A more detailed discussion of the LEX design is presented in Appendix A.

3.1.2 Low-Speed Tests

The model and its installation in the 4M x 7M Subsonic Wind Tunnel are shown in Figure 4. The sting support and balance system are different from those used in the high-speed tests because these items are generally unique to the test facility. In the low-speed tests, the sting contained a tube, with bellows at either end, that carried compressed air to the model. As shown in Figure 5, the air passage led straight into the model, and the balance was offset from the sting centerline. This arrangement required different adapters and sting attachment fittings in the model from those used in the high-speed tests.

The only other difference between high-speed and low-speed models was that the low-speed model contained provisions for wing flap extensions. Flaps were made for each wing with brackets for flap deflections of 10 degrees, 20 degrees, and 40 degrees. It was necessary to disconnect pressure orifice tubes to the aileron and spoiler when the flaps were deflected.

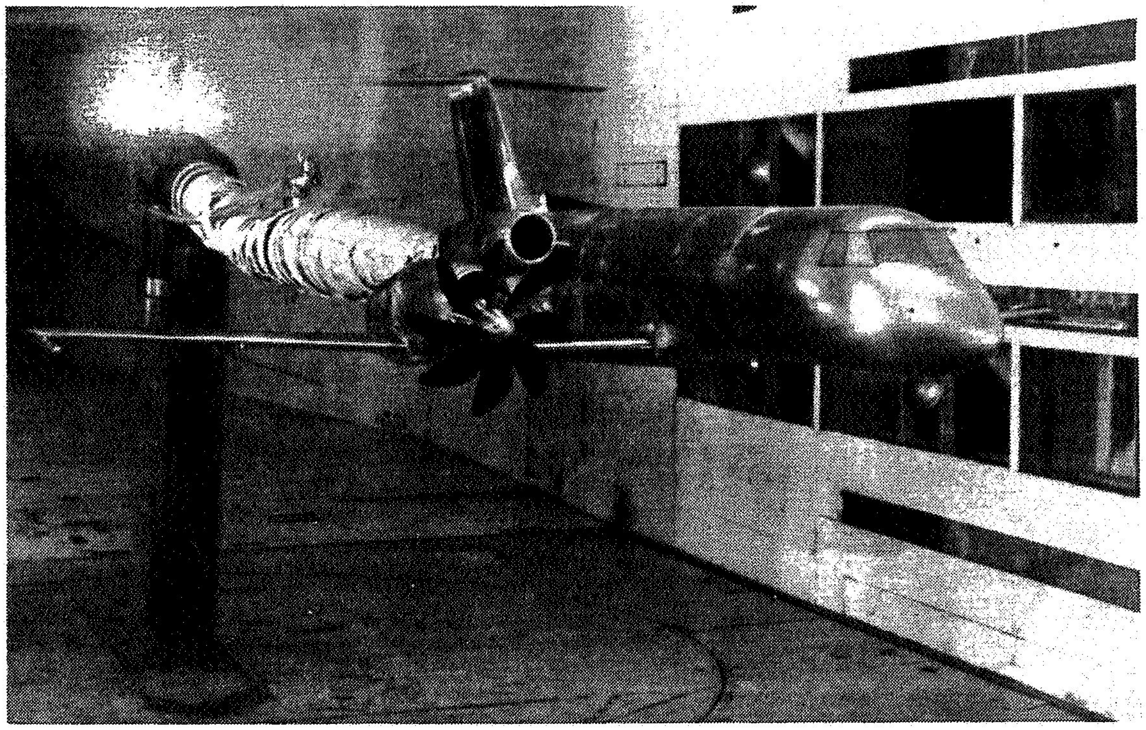

Figure 4. Low Speed Model in 4M x 7M Wind Tunnel

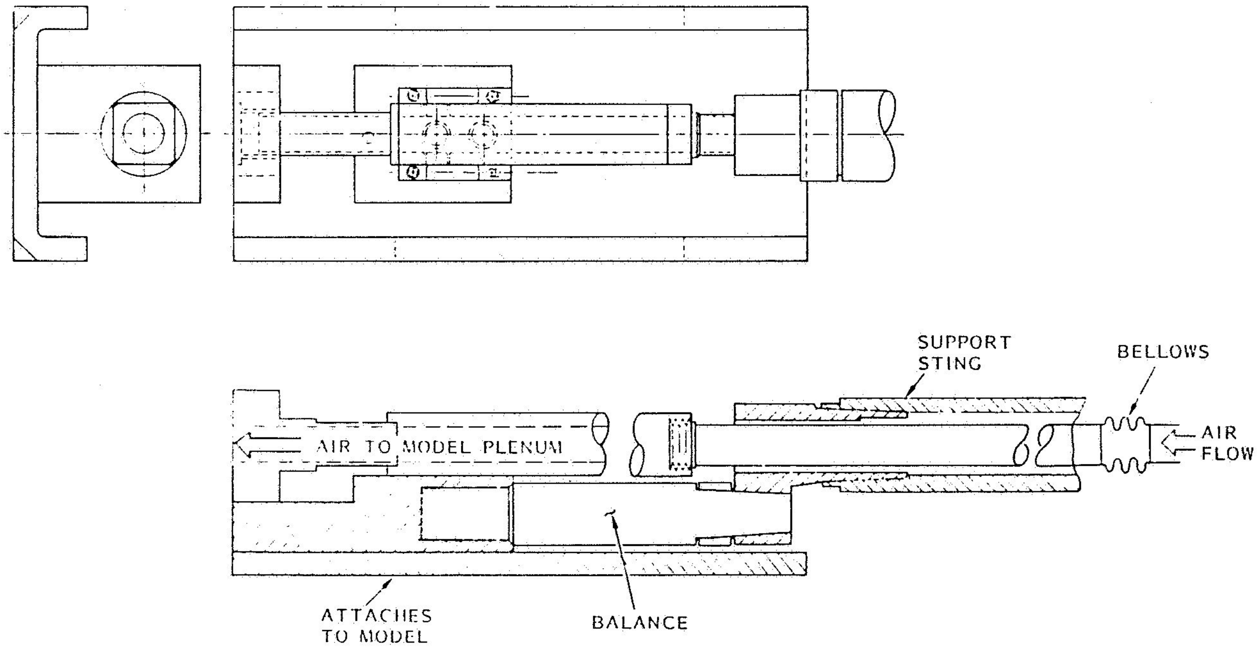

Figure 5. Balance Installation - Low Speed Model

3.1.3 High-Speed Flow Field Semispan Model

The model for the high-speed flow field tests (Figure 6) in the NASA-Lewis 8-Ft x 6-Ft Supersonic Wind Tunnel was a half-model version of the full-span model used in the aerodynamic tests. A new half-fuselage was built with provisions for attachment to a model-centerline reflection plane, which, in turn, was mounted on one tunnel sidewall. Since the model wing was built in separate left-hand and right-hand parts, it was a simple matter to build an adaptor to mount only the right-hand wing to the half-fuselage and sidewall plate. The Spey engine nacelle was retained as an essential part of this model, but vertical and horizontal tail components were omitted. The latter were judged to have little influence on the flow in the region around the front of the PTA nacelle.

The PTA nacelle and other right-hand wing accouterments were attached as in the full-span model. Since the objectives of the test were to obtain flow field data without the propfan, no provisions were made to bring compressed air aboard the model.

The sidewall mounting plate (provided by the test facility) was designed to fit the left hand tunnel wall (as viewed from upstream). To test the right-hand half of the model, it was necessary to mount the model inverted. The model was attached to a turntable imbedded in the sidewall plate (as shown in Figure 7) that could be rotated to change model angle of attack. The model was rotated about the .25 MAC point.

3.2 MODEL PROPFAN BLADES

The objective in design of the model propfan blades was to produce small-scale rotors that would perform aerodynamically like the full-scale Hamilton Standard SR-7L propfan. The full-scale blades are flexible enough so that they twist and bend under flight loads. The small-scale blades, on the other hand, are relatively stiff. The design procedure chosen was to make the small-scale blades in the shape of the loaded full-scale blade in the design cruise condition. Coordinates of the full-scale blades in this flight condition were reduced to model scale by Hamilton Standard and provided for blade design.

The small size of the model blades resulted in a situation at the blade leading and trailing edges where departures from scale were necessitated by the fabrication technique. Metal blades were not allowed in the 16-Ft Transonic Aerodynamics Wind Tunnel for fear of the damage potential if a blade were lost at the high rotational speeds (to about 19,000 rpm) during the high-speed tests. The blades were fabricated, therefore, of carbon fiber composite material.

The best available material was graphite-epoxy tape in 0.0076 cm (0.003-inch) thickness. Strength considerations required that the model blades in their thinnest regions contain at least two tape layers with the plies oriented at some angle relative to one another. Therefore, the minimum blade element thickness was of the order of 0.0152 cm (0.006 inch). A typical blade is shown in Figure 8.

Figure 9 shows leading edge radii and trailing edge thickness of the LAP blades reduced to 1/9-scale. It can be seen that for a minimum material thickness of 0.0152 cm (0.006 inch), the leading edge radii goes out of scale outboard of the 80-percent span station, and the trailing

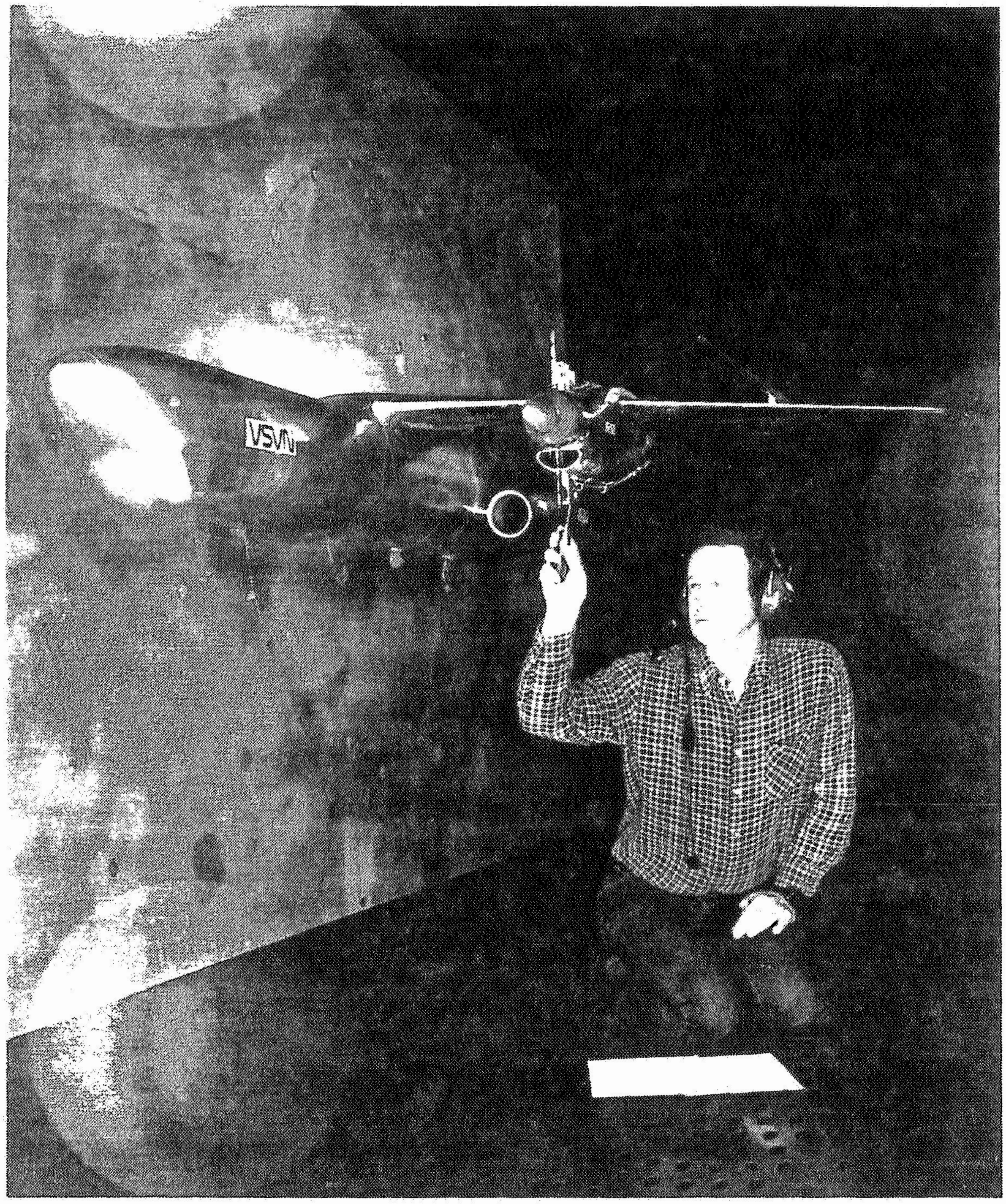

Figure 6. High Speed Flow Field Model

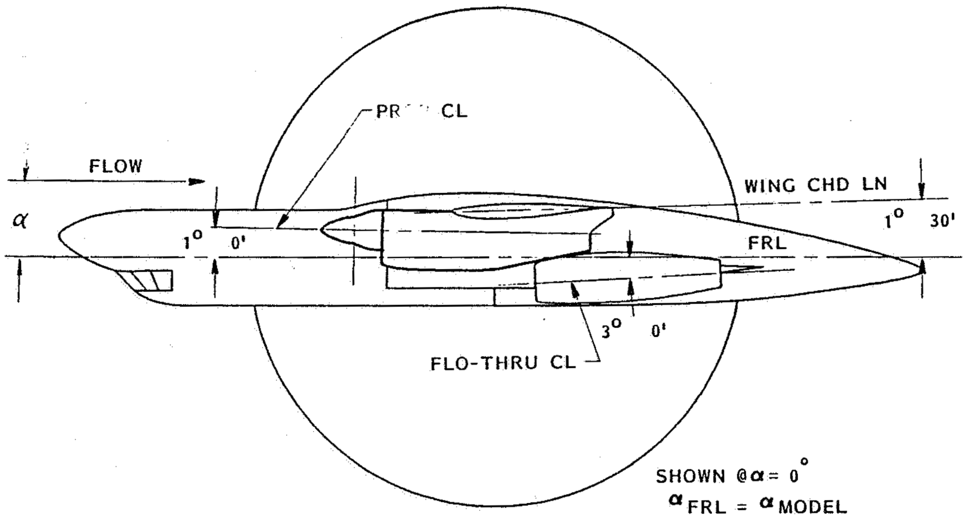

Figure 7. Flow Field Model on Tunnel Side Plate

ORIGINAL PAGE IS
OF POOR QUALITY

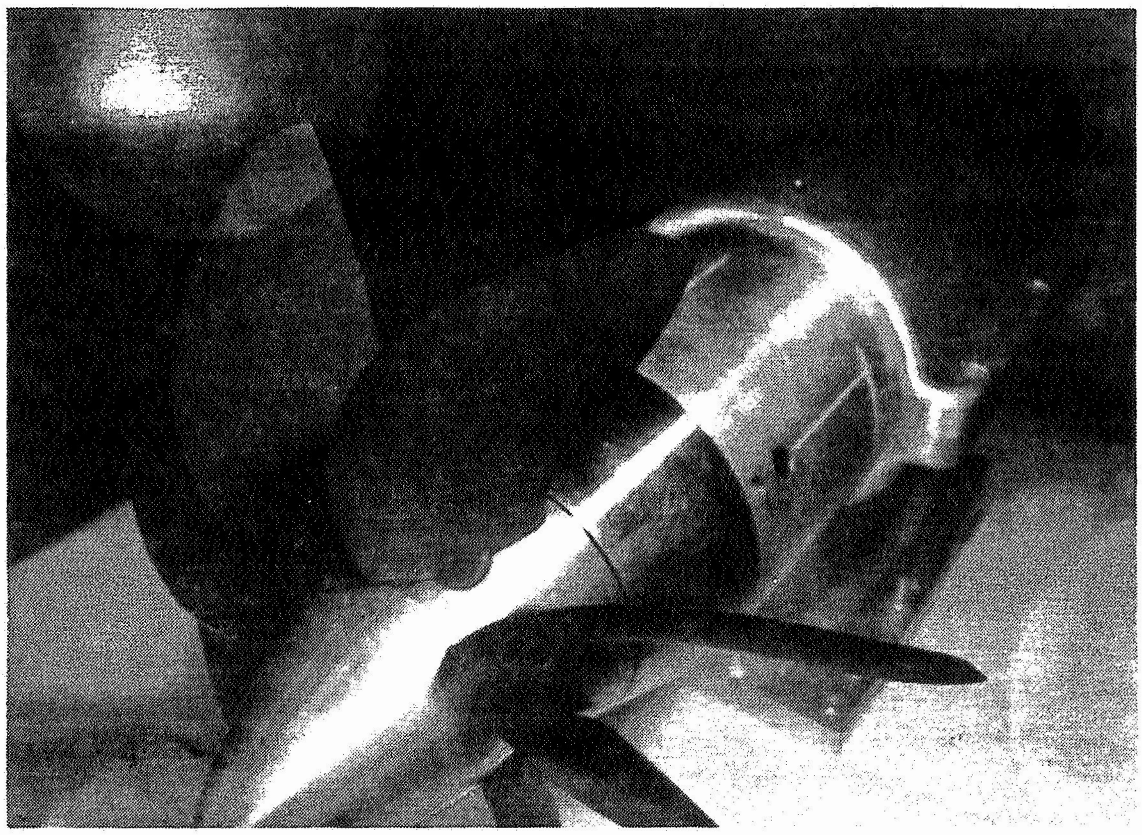

Figure 8. Model Propfan Blade

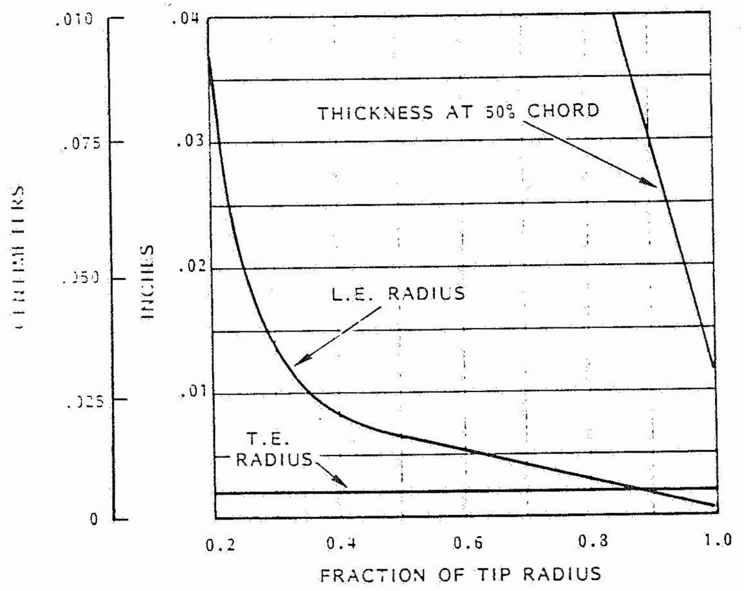

Figure 9. Profan Blade Edge Thicknesses

edge thickness is out of scale over the whole blade span. It was expected that the excess leading edge thickness would be more critical than the excess trailing edge thickness and that the major impact would be on rotor efficiency at high speeds. Because this is the speed region where propfan power effects on the aircraft are likely to be smallest, it was believed that the out-of-scale thickness could be tolerated.

During the course of the high-speed tests, there were two rotor failures. This resulted ultimately in a redesign of the blades to thicken the region near the shank where failures were believed to initiate. These blades were used in the low-speed wind tunnel tests, and there were no more blade failures.

The best measure of how well the blades were scaled derives from results of the isolated propeller tests. It will be shown in discussion of those results that the model propfan rotors simulated the full-scale article reasonably well.

3.3 ISOLATED PROPELLER MODEL

The objective in designing apparatus for isolated propeller tests was to produce a test nacelle and support that interferes minimally with the propeller. Apparatus for the high-speed isolated nacelle tests is shown in Figure 10. The hub, spinner, balance, and motor were the same units used on the aircraft model installation. The nacelle, however, was a streamlined axisymmetric cylinder supported by an aerodynamically contoured, swept strut connected to the model support sting. Drive motor air was routed through the sting and support strut to the forward part of the nacelle, through the motor, and then out the aft portion of the nacelle.

To measure the aerodynamic forces on the propeller, the nacelle was fitted with the same hub balance used in the aircraft model--located between the propeller hub and the drive motor.

Other instrumentation included static pressure ports upstream and downstream of the motor to measure static pressure drop across the motor, a total pressure rake at the nacelle exit, and thermocouples at the motor inlet, motor outlet, and downstream of the choke plate.

The apparatus used for the low-speed isolated propeller tests is shown in Figure 11. Design requirements for the low-speed tunnel dictated a stiffer nacelle support than that used in the high-speed tests. Thus, the configuration shown in Figure 11 used two cylindrical halves to clamp the nacelle. The lower half was welded to an aerodynamically contoured vertical strut with a bottom plate that bolted directly to the NASA model support fixture. The bulkiness of the isolated nacelle model for these low-speed tests was greater than desired, but was deemed acceptable because it was a low speed test.

Instrumentation was the same as for the high-speed installation.

3.4 INSTRUMENTATION

3.4.1 Model Pressure Instrumentation

The right-hand wing of the model was instrumented with 196 static pressure orifices as shown in Figure 12. These were located at spanwise stations such that the effect of the propeller, the nacelle, and their

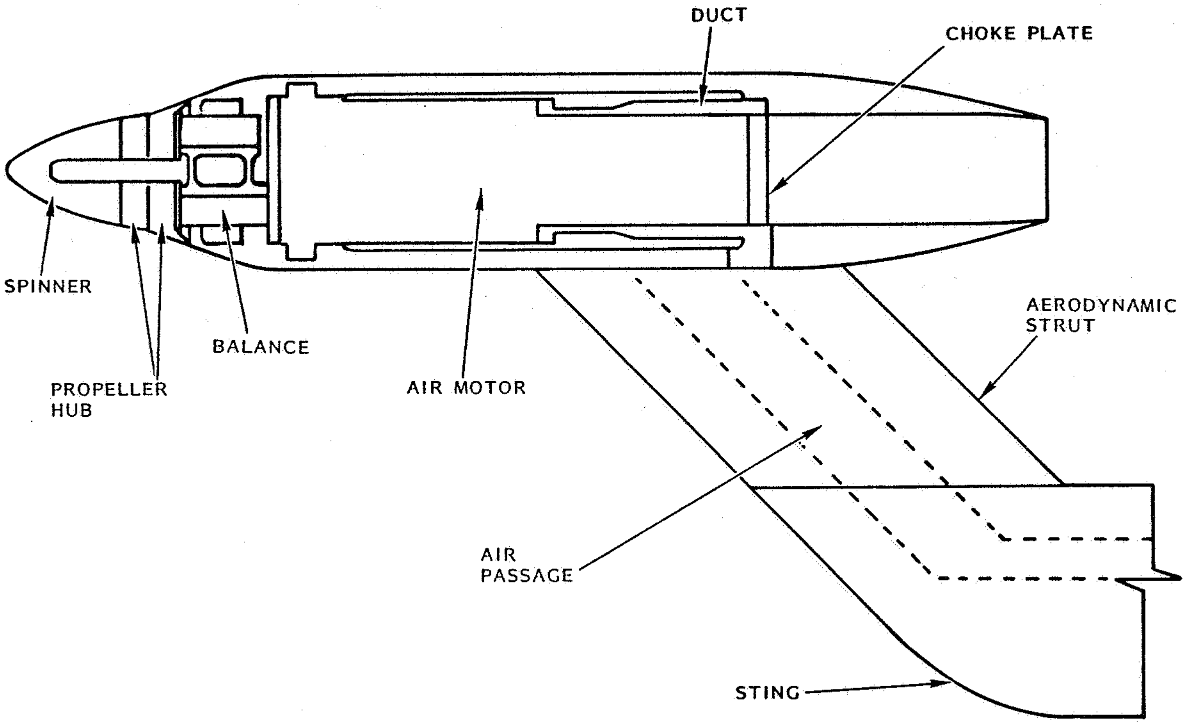

Figure 10. Isolated Propeller Apparatus - High Speed Tests

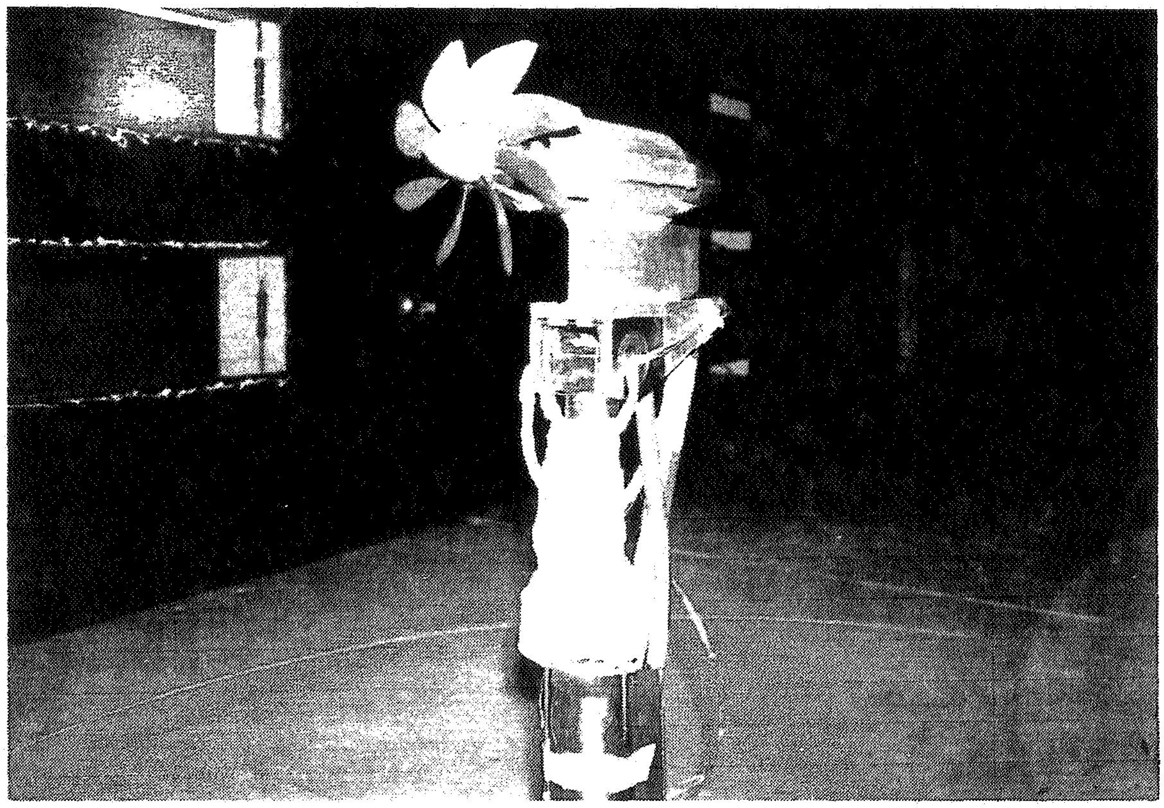

Figure 11. Photograph of Isolated Propeller Model in Low Speed Wind Tunnel

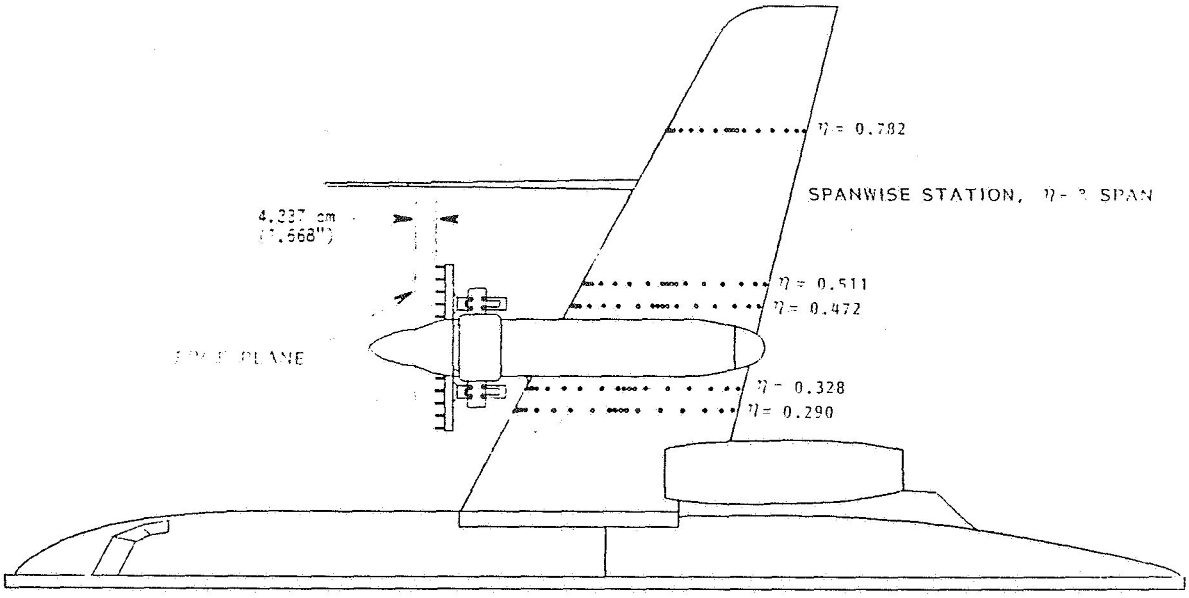

Figure 12. Model Wing Pressure Instrumentation

ORIGINAL PAGE IS
OF POOR QUALITY

interaction on the aerodynamic loading of the wing could be determined. Two chordwise rows were located on either side of the nacelle, at non-dimensional semispan stations η = 0.290, 0.328, 0.472, and 0.511. These positions correspond to distances from the propfan centerline of 85-percent and 55-percent of the propeller tip radius on either side of the nacelle. A fifth chordwise row was located near the wing tip at η = 0.782 to obtain wing surface pressure data outside the influence of the propeller and nacelle. Each row contained 18 orifices on the upper surface and 14 on the lower surface. The chordwise locations of the orifices were closely spaced at the leading edge to capture the high pressure gradients and also in the 50-percent chordwise region to determine the shock location at transonic speeds.

Four additional spanwise orifice stations were located at η = 0.231, 0.256, 0.545, and 0.569 to help define wing loads. These were limited to eight orifices in each row, two each on the upper and lower surfaces at the leading edge, and two each on the upper and lower surfaces at the trailing edge.

There were 24 static pressure orifices on the nacelle. Eight were located along the centerline of the cowl on top of the nacelle. On each side of the nacelle, eight orifices were located as shown in Figure 13.

Figure 12 also shows pressure rakes just aft of the prop plane. These rakes were used to obtain flow field data on the semi-span model in the NASA-Lewis 8-Ft x 6-Ft Supersonic Wind Tunnel as discussed in Section 3.4.6.

3.4.2 Total Pressure Rakes

Inlet total pressure rakes were located in both the PTA and Spey engine nacelles to evaluate internal drag. The Spey inlet rake was also designed to measure flow distortion, if any, caused by the PTA installation. On the PTA nacelle, the flow-through duct on top of the nacelle contained 5 total pressure probes and 4 static pressure orifices. The Spey nacelle inlet had 12 total pressure probes and 4 static pressure orifices.

An external rake consisting of 29 total pressure probes was mounted at the exit plane of the PTA nacelle duct so that the jet thrust from the air turbine could be measured. The probes in this rake were arranged in three horizontal rows and one vertical row on the nacelle exit centerline.

3.4.3 Propfan Hub Balances

The propfan hub balance (Figure 14) was a non-rotating balance that measured five components: axial force, normal force, pitching moment, and to a limited accuracy, side force and yawing moment. The balance was located between the drive air-motor and the propeller hub. The balance consisted of two half-cylinders (one metric and one non-metric) connected by four beams, and a shaft located by two bearings in the metric half-cylinder of the balance. A flexure element that transmits only torque connected the shaft to the drive motor.

After an equipment failure in the high-speed tests that resulted in balance failure and loss of model hardware, a fail-safe redesign was developed. To ensure retention in the hub in the event that the beams or

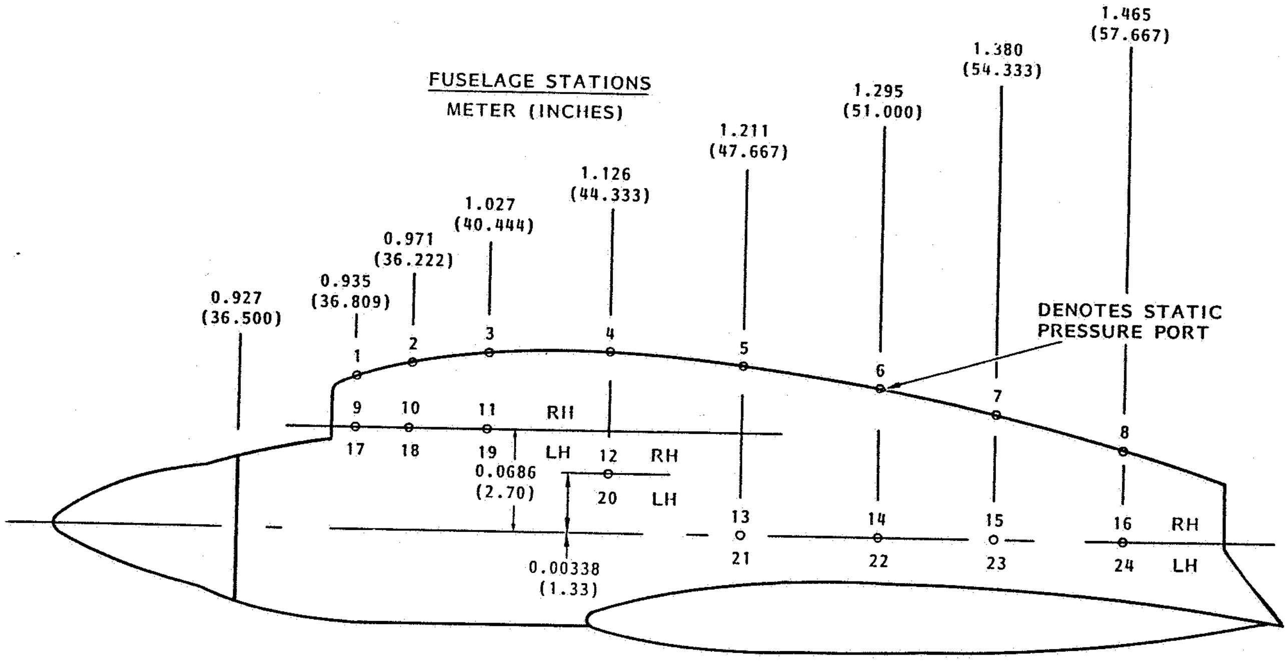

Figure 13. PTA Nacelle Pressure Instrumentation

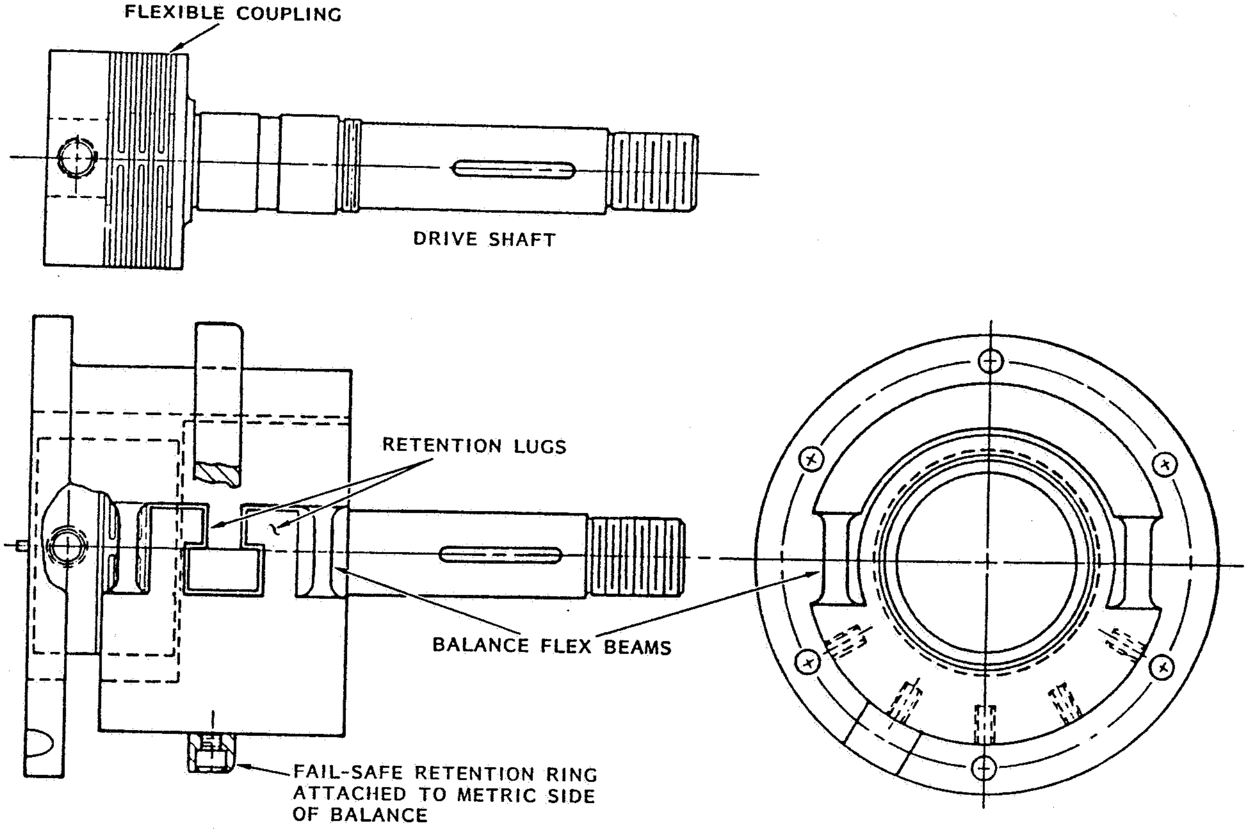

Figure 14. Propfan Hub Balance

the flex coupling were broken, a retention ring was machined onto the metric half of the balance, and the two cylinder halves were made to interlock by forming a 'T' shaped tongue on the non-metric portion of the cylinder half and a corresponding cutout on the metric cylinder half with a 0.102 cm (0.040 inch) clearance allowed between the two. The hardware shown in Figure 14 includes the elements of the redesign.

3.4.4 Low-Speed, Six-Component Force Balance

Six-component force and moment data were recorded on all runs using a 5.08 cm (2.0-inch) diameter internal balance. The balance was a NASA-Langley balance designated as Balance 748. It was an orthogonal type such that each load component was measured by a separate strain gage bridge. The force and moment limits of the balance were:

NF ± 8,007 N (1,800 lb)

AF ± 2,224 N (500 lb)

PM ± 791 m-N (7,000 in.-lb)

SF ± 4,448 N (1,000 lb)

YM ± 339 m-N (3,000 in.-lb)

RM ± 452 m-N (4,000 in.-lb)

The balance was attached to a NASA-Langley offset adapter which mounts to a sting passing through the lower aft fuselage. NASA-Langley provided the balance calibration and the corrections necessary to account for the mechanical bridging of the balance by the air supply line and the instrumentation wire/tube bundle.

3.4.5 High-Speed, Six-Component Force Balance

The six-component balance used in the high-speed tests was a 4.0-inch diameter internal balance built by Modern Machine and Tool Company and designated as Balance 984. This balance was also an orthogonal type. The force and moment limits of the balance were:

NF ± 24,465 N (5,500 lb)

AF ± 2,224 N (500 lb)

PM ± 4,519 m-N (40,000 in.-lb)

SF ± 6,672 N (1,500 lb)

YM ± 2,824 m-N (25,000 in.-lb)

RM ± 3,954 m-N (35,000 in.-lb)

3.4.6 Flow Survey Rakes

To determine velocities and flow angles in and around the propeller plane a special flow survey rake was employed. This rake, as shown in Figure 15, contained five, 5-hole probes one inch apart on each of two arms. For surveys around the PTA nacelle, the rake was mounted on a collar that attached to the nacelle just behind the inlet cowl. This collar allowed the rake to be positioned at four azimuthal locations, and at each location the rake could be positioned radially at two locations so that points one-half inch apart could be obtained. The rake mount also allowed a certain amount of fore-and-aft positioning.

Design of the 5-hole probes was based on extensive experience with such flow field measurements. Reference 1 presents typical results from such instruments. Effective use of these probes, however, depends on a calibration to define the angular sensitivity of the probes. Such a calibration of these rakes was performed in a small transonic wind tunnel at Mach numbers to 0.95 and is described later.

3.5 CALIBRATIONS

3.5.1 Propfan Airmotor Calibration

Because propfan torque could not be measured with the hub balance, a calibration was performed to determine air motor torque as functions of drive pressure into the motor and motor rotational speed. The calibration was performed on a hydraulic dynamometer test rig for two nacelle configurations: the PTA nacelle and the isolated nacelle.

The calibration curves were of excellent quality. It is believed that horsepower values for the wind tunnel data are accurate within about 0.447 kw (0.6 HP) or, at maximum power, about 0.4-percent.

3.5.2 Flow Survey Probe Calibration

Details of a 5-hole probe are shown in Figure 16. Each probe consisted of four pitot tubes soldered around a central pitot tube and a cone static probe offset to one side. The central tube in the bundle was flat-faced, and the side tubes were chamfered at 45-degree angles. The rakes were calibrated in the Lockheed-Georgia Compressible Flow Wind Tunnel (CFWT) by placing each rake, in turn, in known flow conditions and measuring the pressure at each orifice on the rake. The flow conditions were varied by changing the roll and pitch angle settings of the rake and varying the test section Mach number.

This calibration and the 5-hole probe data reduction procedures are described in Appendix B.

3.6 WIND TUNNEL AND MODEL INSTALLATIONS

3.6.1 High-Speed Tests - Langley 16-Ft Transonic Aerodynamics Wind Tunnel

The NASA-Langley 16-Ft Transonic Aerodynamics Wind Tunnel is a single return atmospheric wind tunnel with Mach number range from 0.2 to 1.3. The slotted octagonal test section nominally measures 4.72m (15.5 feet) across the flats and has a usable test section length of 6.71m (22 feet).

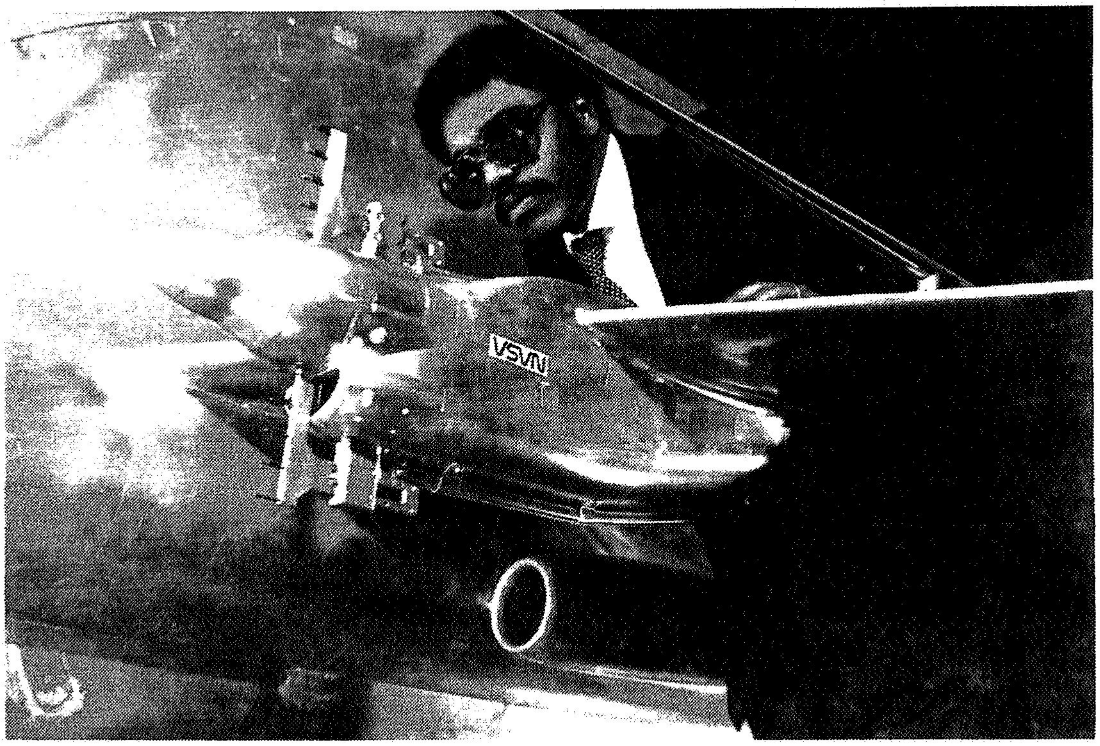

Figure 15. Flow Survey Rake

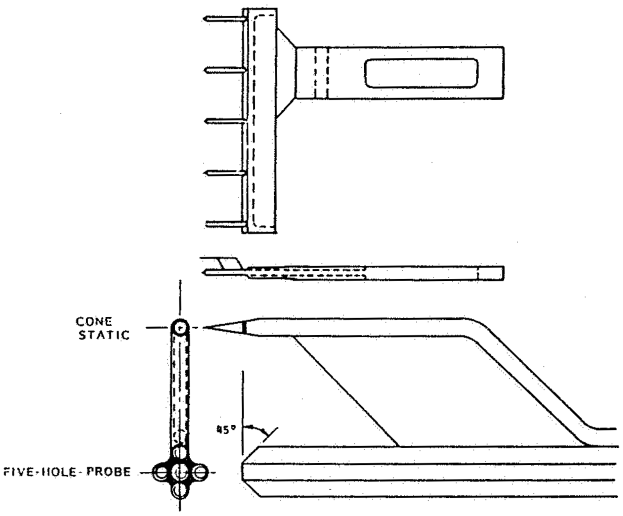

Figure 16. 5-Hole Probe

The PTA model was sting-mounted in the tunnel as shown in Figure 1. Model blockage based on maximum frontal area was less than 1 percent. Reynolds numbers, based on MAC ranged from about 1.8 million at Mach 0.2 to about 5 million at Mach 0.8.

Temperature in the 16-ft Transonic Aerodynamics Wind Tunnel normally increased with operating time so that the model seldom, if ever, arrived at thermal equilibrium. Unfortunately, the balance and air bypass system was sensitive in the drag direction to thermal gradients. Even though an attempt was made to measure model, balance, and bypass line temperatures and compensate for the temperature gradients, this was not completely successful. Errors in axial force measurements for the powered runs were, therefore, higher than desired. With this exception, the flow quality in this facility was good, and data from the tests were of high quality.

3.6.2 Low-Speed Tests - Langley 4M x 7M Subsonic Wind Tunnel

The NASA-Langley 4M x 7M Subsonic Wind Tunnel is a single return subsonic wind tunnel with Mach numbers to about 0.3. The test section is 4m (14.5-feet) high and 7m (21.75-feet) wide. The PTA model was sting-mounted in the test section as shown in Figure 4. Tests were run primarily at $M = 0.165$ and $q = 1915\ N/m^2$ (40 psf) although a few runs were made at $M = 0.2$ and $q = 2873\ N/m^2$ (60 psf). Reynolds numbers based on mean aerodynamic chord ranged from 1.6×10^6 to 2×10^6.

Although the balance/air bypass system was different from that used in the high-speed tests, problems were again encountered with measuring power-on drag. Power-off drag was reliable as were all other forces and measurements with power on, but the power-on drag data were not good--apparently due to interference between the sting and the air bypass line.

3.6.3 High-Speed Flow Survey Tests - Lewis 8-Ft x 6-Ft Supersonic Wind Tunnel

The NASA-Lewis 8-Ft x 6-Ft Supersonic Wind Tunnel, in its aerodynamic cycle, is operated as a closed system with dry air added as required to maintain the desired tunnel condition. The tunnel is capable of operating in the Mach number range from 0.36 to 2.0, but for these tests was operated at Mach numbers from 0.6 to 0.85. Reynolds number, based on MAC, ranged from about 4.7×10^6 to 5.6×10^6.

The test section is 2.44m (8 feet) high, 1.83m (6 feet) wide, and 7.16m (23.5 feet) long. It is perforated on all four walls to provide approximately 6-percent porosity.

The half-fuselage, semispan PTA model was mounted on a flat plate which in turn was installed along one sidewall as shown in Figure 6. The sidewall plate is displaced 15.24 cm (6 inches) from the tunnel wall to minimize wall boundary layer contamination of flow around the semispan model.

Blockage of the model in the tunnel was 1.87 percent of the tunnel cross-sectional area.

4.0 TEST PROCEDURES

In the wind tunnel environment, tests are generally conducted with Reynolds numbers about one order of magnitude lower than in full scale flight. The major impact of this Reynolds number disparity is on viscous phenomena like boundary layer growth, transition from laminar to turbulent flow, and boundary layer separation. In full-scale flight, the boundary layer is turbulent over most of the aircraft surface; on the models, however, the boundary layer will usually be laminar unless it is artificially tripped. Special care must be exercised in the wind tunnel to attain the boundary layer conditions that give proper simulation of flight.

For high-speed wind tunnel tests, experience has shown that it is important to produce the thinnest possible turbulent boundary layer on wing surfaces. If the boundary layer is thicker than for full-scale simulation, strong adverse pressure gradients such as those associated with transonic shock waves may cause the boundary layer to separate ahead of the position where it would separate in flight. In some cases, this has caused wind tunnel forces and moments to be much different from those experienced in flight. It is something of an art, therefore, to trip the laminar boundary layer at the place where the best simulation of flight characteristics is achieved.

In the wind tunnel, if the boundary layer is tripped too far forward, it will thicken disproportionately in the low Reynolds number environment and be too thick in the aft regions of the wing. Standard procedure, therefore, is to place the boundary layer trip as far aft as possible and still be assured that the turbulent boundary layer will be well-developed in the regions where it will be subjected to strong adverse pressure gradients. Usually, the test personnel at a given facility will have had enough experience with models of a given type to have a good "feel" for location of transition trips, and considerable reliance is placed on their judgement.

In low-speed wind tunnel tests, there are no strong shock-wave-induced adverse pressure gradients to contend with, and generally in low-speed wind tunnels, the data are much less sensitive to boundary layer simulation procedures. Again, however, the personnel of a given facility are usually the best source of guidance in this matter.

These and other factors pertinent to the process of obtaining good flight data in PTA scale model wind tunnel tests are discussed in the following sections.

4.1 HIGH-SPEED TESTS - 16-FT TRANSONIC AERODYNAMICS WIND TUNNEL

High-speed tests were performed with the GII model and with the model configured in the PTA configuration. In each case, runs were made with tail on and off. Configuration variables on the PTA model included the effects of spoiler, aileron, and rudder deflection. Data were also obtained for feathered propeller, windmilling propeller, and powered propeller. Propeller motor power limitations were such, however, that in these high-speed tests, thrust coefficients were limited to about 0.10.

A series of tests were run to determine the effects of boundary layer tripping technique. Figures 17 and 18 show results at Mach 0.85 of

PRECEDING PAGE BLANK NOT FILMED

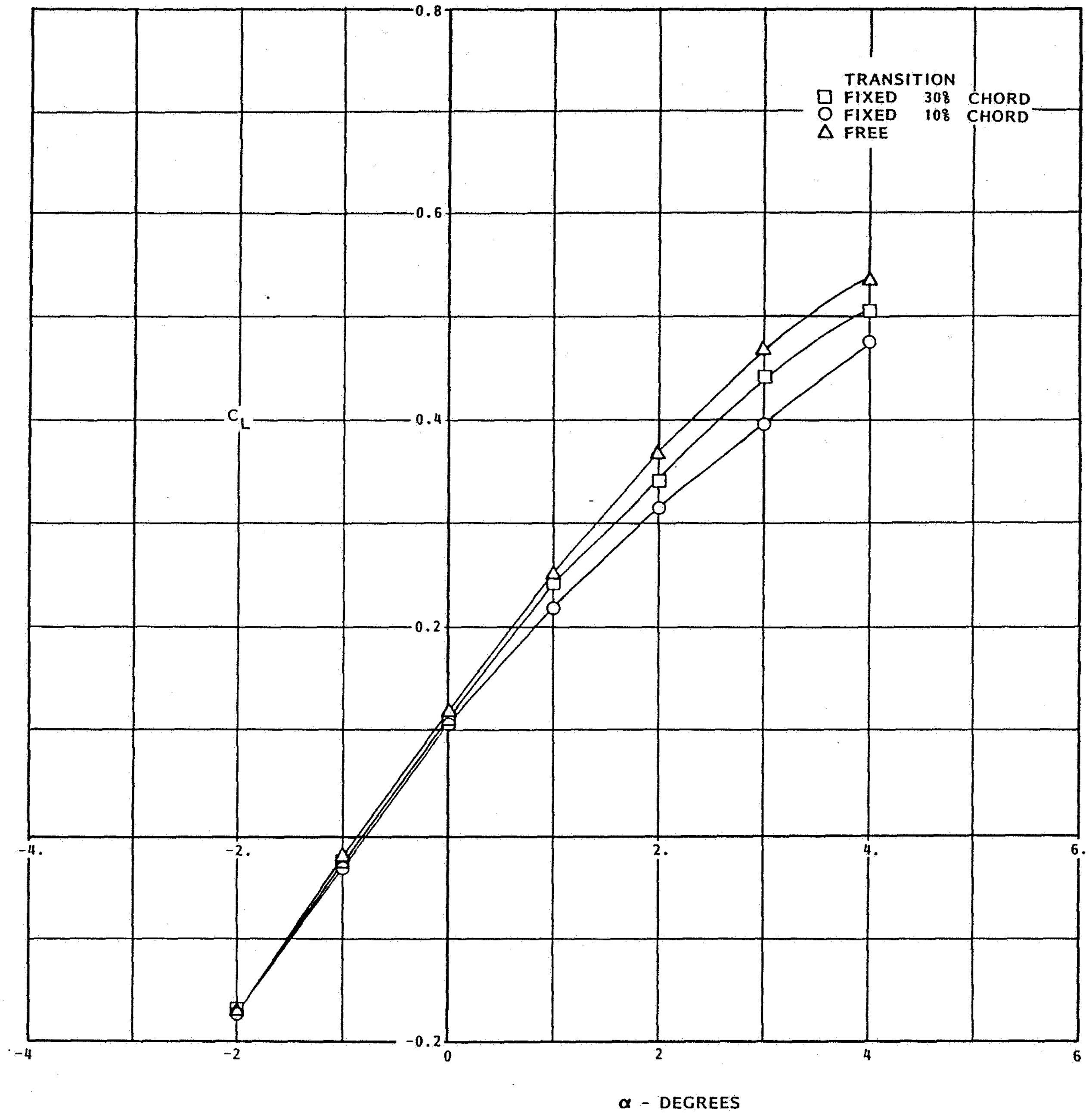

Figure 17. Effects of Transition Fix on Lift

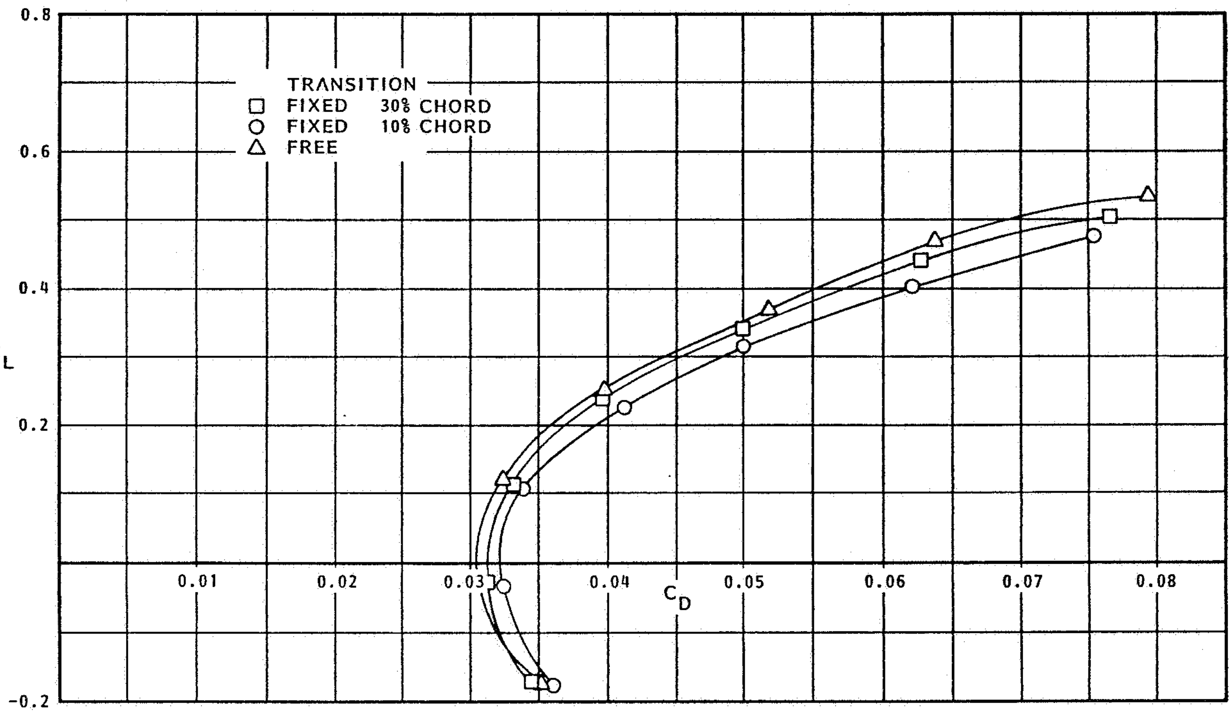

Figure 18. Effects of Transition Fix on Drag

several trip locations on lift curves and drag polars. Transition was fixed by gluing small glass spheres (Ballotini balls) in a narrow strip on the wing surface. Fixing transition at 10-percent chord resulted in higher drag than at the 30-percent chord location and also resulted in a break off of the lift curve slope at a lower angle of attack. This implies that the boundary layer was unnecessarily thickened by tripping at the 10-percent chord location. Furthermore, since there is no indication that tripping at 30-percent chord produced any premature separation or unnecessary drag, these data indicate that the 30-percent location is preferable. Most of the high-speed wind tunnel data, therefore, were obtained with transition fixed at the 30-percent chord location.

Test conditions included Mach numbers of 0.4, 0.7, 0.8, and 0.85, and angles of attack ranging from -2 degrees up to the angle of attack for buffet onset. Two propeller advance ratios were set for each combination of Mach number and blade pitch angle. Table I summarizes the test conditions.

4.2 LOW-SPEED TESTS - 4M X 7M SUBSONIC WIND TUNNEL

Low-speed tests were performed in a manner similar to that of the high-speed tests. The basic GII model was tested with tail off and on; and with runs to measure the effects of flaps, spoilers, aileron, rudder, and elevator. For the PTA configuration, in addition to the above, variables included tip booms, the acoustic boom, PTA nacelle incidence, and propfan with and without power. The propfan was also tested on the isolated nacelle. Flow survey tests were made on the model in the propeller plane (prop-off) and on the isolated nacelle rig both in the propeller plane and behind the powered propeller.

All of the model tests in the low-speed tunnel were made with transition free on the advice of the facility test personnel. Most of the tests were run at a Mach number of 0.165. Model angles of attack ranged from -2 degrees to at least the stall condition, and, when model vibration was not excessive, to several degrees beyond stall. Some tests were performed at Mach 0.2 with propeller powered in order to get a more appropriate range of advance ratios. The same was true for the isolated propeller tests. Two blade angle settings were used for all of the powered propeller tests.

Run conditions for the low-speed tests are summarized in Table II.

4.3 HIGH-SPEED FLOW SURVEY TESTS - 8-FT X 6-FT SUPERSONIC WIND TUNNEL

For the high-speed flow survey tests on the semispan model, all of the flow surveys were made in the propeller plane with the propeller off. Mach numbers were varied from 0.60 to 0.85; nacelle tilt angles tested were -3, -1, and +2 degrees; and model angle of attack ranged from -2 to +6 degrees. In addition to flow survey rake pressures, pressure distributions on the wing were measured to compare with those from other scale tests.

Run conditions for these tests are summarized in Table III.

TABLE I.
HIGH SPEED TEST CONDITIONS

(a) No Power On Propfan

CONFIGURATION	PROP	BL TRANSITION	MACH NO.					
			.4	.7	.78	.8	.82	.85
GII - Upright	--	B	X	X		X		X
GII - Inverted	--	B	X	X		X		X
GII - Tail On	--	B	X	X		X		X
		Free	X	X		X		X
		A	X	X	X	X	X	X
GII - Tail Off	--	B	X	X		X		X
PTA - Tail Off	Off	B	X	X		X		X
PTA - Tail On	Off	B	X	X		X		X
PTA - W/O Acoustic Boom	Off	B	X	X		X		X
PTA - No Booms	Off	B	X	X	X	X	X	X
		Free	X	X	X	X	X	X
		A	X	X	X	X	X	X
PTA to LEX	Off	A	X	X	X	X	X	X
PTA + LEX + Nacelle Bump	Off	A			X	X	X	X

<u>Transition</u>

A - Fixed at 10% Chord
B - Fixed at 30% Chord

TABLE I.
HIGH SPEED TEST CONDITIONS

(b) Powered Propfan

CONFIGURATION	PROPFAN ADVANCE RATIO, J	BL TRANSITION	MACH NO.	δ_R	δ_A	δ_S
PTA - Tail On	1.7	B	.4			
	2.9	B	.7			
	2.9	B	.7			
	3.3	B	.8			
	3.06	B	.8			
	3.06	Free	.8			
Rudder Deflection	1.8	B	.4	+5°		
	2.9/3.2	B	.7	+5°		
	3.2/3.37	B	.8	+5°		
	1.8	B	.4	-5°		
	2.9/3.2	B	.7	-5°		
	3.2/3.37	B	.8	-5°		
Aileron Study	1.7/1.8	B	.4		-10°	
	2.9/3.2	B	.7		-10°	
	3.2/3.37	B	.8		-10°	
Spoiler Study	1.7/1.8	B	.4			-10°
	2.9/3.2	B	.7			-10°
	3.6	B	.8			-10°
	3.2/3.37	B	.8			-10°
Aileron & Spoiler	1.8	B	.4		-10°	-10°
	2.9/3.2	B	.7		-10°	-10°
	3.2/3.37	B	.8		-10°	-10°
PTA & LEX	1.8	B	.4			
	2.9/3.06/3.2	B	.7			
	3.3/3.4	B	.8			
	3.2/3.37	B	.8			

TRANSITION

A - Fixed at 10% Chord
B - Fixed at 30% Chord

TABLE II.
LOW SPEED TEST CONDITIONS

Transition Free

MODEL CONFIGURATION	α	β	q	PROP OFF	PROP WINDMILL	PROP FEATHER	J	EFFECTS/STUDIES
Tail Off	Sweep	-5, 0, +5	(1)	X		X	.85-1.8	
Horizontal Stabilizer Off	Sweep	-5, 0, +5	(1)	X		X	.85, 1.8	
Tail On	Sweep	-5, 0, +5 0	(1) (2)	X		X	.85-1.8 .85-1.8	
Spoiler Study (-35°)	Sweep	Sweep	(1)	X		X		
Aileron (-10°) + Spoiler (-35°)	Sweep	Sweep	(1)	X			.85, 1.8	
Rudder (-25°)	Sweep	Sweep	(1)				.85, 1.8	
Elevator (-25°, +10°)	Sweep		(1)				.85, 1.8	
Prop Pitch = 38°	Sweep		(1) (2)				.85-1.8	
Nacelle Tilt (-3°, -1°, +2°) (Tail Off & On)	Sweep	Sweep	(1)	X		X	.85-1.8	
Takeoff Flaps	Sweep	Sweep	(1)	X		X		Tail-Off, Horiz Stab Off, Tail-On, Spoiler, Aileron & Spoiler, Rudder, Elevator, Nacelle Incidence
Landing Flaps	Sweep	Sweep	(1)	X	X	X		
GII	Sweep	Sweep	(1)					Tail On & Off, Spoiler, Aileron & Spoiler, Rudder, Elevator
GII - Takeoff Flaps	Sweep	Sweep	(1)					Tail On & Off, Spoiler, Aileron & Spoiler, Rudder, Elevator
GII - Landing Flaps	Sweep	Sweep	(1)					Tail On & Off, Spoiler, Aileron & Spoiler, Rudder, Elevator

(1) $q = 1915\ N/m^2$ (40 psf)

(2) $q = 2873\ N/m^2$ (60 psf)

TABLE III.
HIGH SPEED FLOW SURVEY TEST CONDITIONS

NT	α	M_0	COLLAR
-1°	-2° to +6°	.6 - .85	On
+2°	-2° to +6°	.6 - .85	On
+2°	-2° to +6°	.6 - .85	Off

4 Horizontal Rake Positions and
4 Vertical Rake Positions for
Each Point

4.4 FORCE MEASUREMENT TARES, CALIBRATIONS, AND CORRECTIONS

In preparation for the PTA wind tunnel tests, several important calibrations were performed. The first of these was the propeller drive motor calibration described earlier. This calibration was needed because there were no provisions on the model for measuring propeller torque.

The exhaust from the propeller drive motor provided a significant thrust component that required special calibrations in the wind tunnel. First, a static tare calibration was performed with the PTA nacelle replaced by a calibrated jet nozzle. This test determined the interactions between nozzle thrust and other forces and moments measured during wind tunnel tests. A second static tare was performed with the PTA nacelle on the wing and the drive motor pinned to prevent rotation in order to determine the residual jet thrust of the PTA nacelle. Finally, with wind on, the same model set-up was tested with and without jet flow to provide a jet thrust calibration that included interference effects with the tunnel flow.

In the powered wind tunnel tests, propeller thrust was measured with the propeller hub balance between the drive motor and the propeller. To obtain drag, this thrust was corrected for base and forward surface pressure forces on the hub and added to force balance measurements.

As mentioned earlier, the force balance used in the high-speed wind tunnel was sensitive to temperature effects in the drag direction. This sensitivity originated in the high pressure air lines (for propeller drive) that passed around the balance. The bellows used in these lines were not sufficiently flexible to compensate for thermal expansion forces at high pressures. The problem was aggravated by the operational characteristic of the wind tunnel that resulted in a continuously increasing air temperature with increasing run time. An attempt was made to calibrate this force by instrumenting the balance with a number of thermocouples. This effort was unsuccessful, however, so the powered drag data for the high-speed tests was not reliable. This thermal expansion effect did not, however, degrade other force measurements (lift, side force) since the bypass lines were sufficiently flexible in all directions except along the balance axis.

In the low-speed wind tunnel, a different balance system was used but again the drag measurements with the propfan powered were erratic and generally unreliable. These disappointing results highlight the difficulties involved in obtaining good drag data when high pressure air lines must bypass a force balance in a relatively small model. Time constraints in this test program did not permit the development needed to solve these measurement problems.

5.0 DATA ACCURACY

The following examples provide estimates of data accuracy in the measurement and calibration of test parameters and performance coefficients. All pressures are normalized with reference to standard atmospheric pressure, 101,325 N/m² (2,116 psf).

Freestream Mach Number

- $$M_0 = \left\{\frac{2}{\gamma - 1}\left[\left(\frac{H_0}{P_0}\right)^{\frac{\gamma-1}{\gamma}} - 1\right]\right\}^{\frac{1}{2}}$$

  Assume $M_0 = 0.6094$, $\gamma = 1.4$

  Static Pressure Error = Total Pressure Error = ±.002362

  Let $H_0 = 1.2141$ and $P_0 = 0.9448$

- Max/Min Error Analysis

  With the above pressures:

  $M_{0_{max}} = 0.6149$

  $M_{0_{min}} = 0.6038$

  $\Delta M_0 = \pm 0.9\%$

- RMS Error Analysis

  $$\text{RMS Error} = \left[\left(\frac{\partial M_0}{\partial H_0} H_{0_{error}}\right)^2 + \left(\frac{\partial M_0}{\partial p_0} p_{0_{error}}\right)^2\right]^{\frac{1}{2}}$$

  $$\frac{\partial M_0}{\partial H_0} = 1.037; \quad \frac{\partial M_0}{\partial p_0} = 1.334$$

  $$\text{RMS Error} = [(1.037*.002362)^2 + (1.334*.002362)^2]^{\frac{1}{2}}$$

  $$= .00399 \quad \text{or} \quad 0.65\%$$

PRECEDING PAGE BLANK NOT FILMED

Freestream Dynamic Pressure

- $q_0 = \frac{\gamma}{2} p_0 M_0^{\,2}$

  For $p_0 = 0.9448$ and $M_0 = 0.6094$

  $q_0 = 0.2456$

- Max/Min Error Analysis

  For the pressure errors cited earlier (±.002362)

  $q_{0_{max}} = .2507$

  $q_{0_{min}} = .2405$

  $\Delta q_0 = \pm 2.1\%$

- RMS Error Analysis

$$\text{RMS Error} = \left[\left(\frac{\partial q_0}{\partial p_0}\, p_{0_{error}}\right)^2 + \left(\frac{\partial q_0}{\partial M_0}\, M_{0_{error}}\right)^2\right]^{\frac{1}{2}}$$

$$\frac{\partial q_0}{\partial p_0} = 0.260; \quad \frac{\partial q_0}{\partial M_0} = 0.806$$

$$\text{RMS Error} = \left[(0.26 * .002362)^2 + (0.806 * .0054)^2\right]^{\frac{1}{2}}$$

$$= 0.004396 \quad \text{or} \quad 1.79\%$$

Model Static Pressure Coefficient

- $Cp = \dfrac{p - p_0}{q_0}$

  Assume:

  $p_0 = 0.9448 \pm .002362$

  $p = 1.1810 \pm .00142$

  $q_0 = 0.2456 \pm .004724$

- Max/Min Error Analysis

$$C_{p_{nominal}} = 0.962$$

$$C_{p_{max}} = 0.998$$

$$C_{p_{min}} = 0.927$$

$$\Delta C_p = \pm\ 3.7\%$$

- RMS Error Analysis

$$\text{RMS Error} = \left[\left(\frac{\partial C_p}{\partial p}\, p_{error}\right)^2 + \left(\frac{\partial C_p}{\partial p_0}\, p_{0_{error}}\right)^2 + \left(\frac{\partial C_p}{\partial q_0}\, q_{0_{error}}\right)^2\right]^{\frac{1}{2}}$$

$$\frac{\partial C_p}{\partial p} = 4.072; \quad \frac{\partial C_p}{\partial p_0} = -4.072; \quad \frac{\partial C_p}{\partial q_0} = -3.915$$

$$\text{RMS Error} = [(4.072*.00142)^2 + (-4.072*.002362)^2 + (-3.915*.004724)^2]^{\frac{1}{2}}$$

$$= 0.0216 \quad \text{or} \quad 2.24\%$$

The measurement system for the flow survey rakes used the same transducer, so that pressure coefficients were subject to the same errors.

Balance Uncertainties

The balance accuracies for each component are given in Table IV.

Aerodynamic Coefficient Uncertainties

The uncertainties in the balance when combined with uncertainties in the freestream dynamic pressure give the following uncertainties in lift coefficient and drag coefficient.

Assume a cruise condition of Mach = 0.8, freestream dynamic pressure of q = 29,686 ± 574.6 N/m² (620 ±12 psf), and drag force of D = 1010 ± 11 N (227 ± 2.5 lb). The maximum uncertainty in drag coefficient would be 0.0004 or 4 counts (about 1.1 percent of cruise drag coefficient). For a lift force, L = 9261 ± 122 N (2,082 ± 27.5 lb) the maximum uncertainty in lift coefficient would be 0.004 (about 1.4 percent of cruise lift coefficient).

TABLE IV.
BALANCE ACCURACIES

COMPONENT	LOW SPEED BALANCE LIMITS	LOW SPEED UNCERTAINTIES	HIGH SPEED BALANCE LIMITS	HIGH SPEED UNCERTAINTIES
Normal Force	8,007 N (1,300 lb)	±40.0 N (9.0 lb)	24,465 N (5,500 lb)	±122.0 N (27.5 lb)
Axial Force	1,010 N (500 lb)	±11.0 N (2.5 lb)	2,224 N (500 lb)	±11.0 N (2.5 lb)
Pitching Moment	791 m-N (7,000 in-lb)	±4.0 m-N (35.0 in-lb)	4,519 m-N (40,000 in-lb)	±25.0 m-N (200.0 in-lb)
Side Force	4,448 N (1,000 lb)	±10.0 N (5.0 lb)	6,672 N (1,500 lb)	±33.0 N (7.5 lb)
Yawing Moment	339 m-N (3,000 in-lb)	±1.7 m-N (15.0 in-lb)	2,824 m-N (25,000 in-lb)	±14.0 m-N (125.0 in-lb)
Rolling Moment	452 m-N (4,000 in-lb)	±2.3 m-N (20.0 in-lb)	3,954 m-N (35,000 in-lb)	±20.0 m-N (175.0 in-lb)

6.0 ANALYTICAL PREDICTIONS

The CATIA code (Reference 2) was used to manipulate and store configuration geometry for the models. This code allowed simple and rapid configuration changes to be input to the flow prediction codes. A typical panel model of a PTA configuration is shown in Figure 19.

Well developed analytical codes were available to predict aerodynamic and stability and control characteristics of the PTA model. The basic code was QUADPAN (Reference 3)--an advanced, low order, three-dimensional panel code that has been widely used in aircraft design studies. QUADPAN, while not effective in supersonic flow regions, does incorporate compressibility corrections so that it is reasonably accurate for transonic flows if imbedded supersonic regions are not dominant. A propeller performance code, PROPVRTX, was used to predict slipstream properties. This code and its validation are described in Reference 4. PROPVRTX was interfaced with QUADPAN by restating QUADPAN surface boundary conditions to include velocity perturbations calculated with PROPVRTX, and then correcting surface pressures washed by the slipstream for the pressure rise across the propeller disc. The efficacy of this technique was demonstrated in Reference 5.

The proper level of slipstream thrust was set by scaling axial and tangential velocity distributions to correspond to the desired propfan Cp and J values. The basic slipstream model was derived from flow survey tests reported in Reference 6.

Special consideration was required and given to: treatment of the aircraft wake, simulation of the PTA nacelle exhaust, and accounting for internal flow through the engine nacelle inlets. These and other aspects of the analytical predictions are discussed in Appendix C.

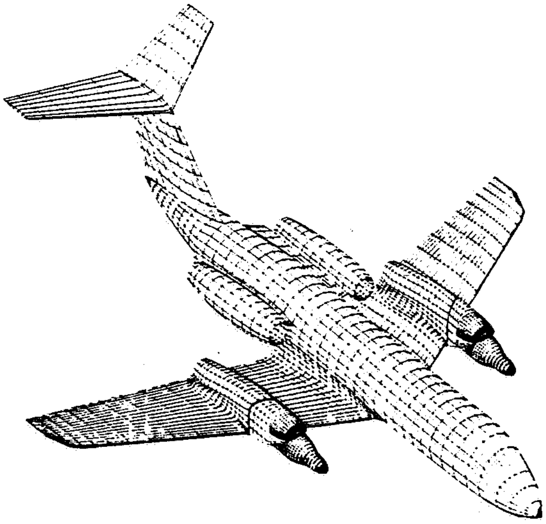

Figure 19. QUADPAN Panel Model of PTA Configuration

7.0 RESULTS AND DISCUSSION

7.1 PERFORMANCE DATA

The nature of the PTA aircraft and the PTA program objectives resulted in the following emphases in the wind tunnel program:

- No powered wind tunnel tests with flaps extended were performed because propfan operation with flaps extended was prohibited on the aircraft.
- A heavy emphasis was placed on high-speed drag because the major aircraft performance concern was on attainment of Mach 0.8 design cruise speed and speeds to Mach 0.85, if possible.
- A strong emphasis was placed on stability and control at low speeds because low altitude flyovers for noise measurements were required.

The PTA model was complicated by the powered nacelle which had a separate force balance for propeller forces and moments, and an air exhaust nozzle that produced significant thrust when the air motor was operating to drive the propfan. A description of model force bookkeeping methods and considerations for drag scaling are given in Appendix D. Drag coefficients presented in this discussion, unless otherwise noted, are defined as follows:

C_D = Model Balance Drag + Propeller Thrust + Powered Nacelle Jet Thrust

7.1.1 Lift/Pitching Moment

7.1.1.1 Data Correlation With Theory

The basic tool used for aerodynamic analysis in the PTA Program was QUADPAN. It was first validated by comparing predicted performance with published GII aircraft data. Such a comparison is shown in Figure 20. It can be seen that QUADPAN predicts the C_L versus α curve extremely well, while a good prediction is obtained for the C_L versus C_m curve. Figure 21 shows a comparison of results from the QUADPAN analytical code with wind tunnel data for the GII model. Again, there is excellent agreement between theory and experiment for the $C_L - \alpha$ curve and good agreement for the C_L-C_m curve. The divergence of data and predicted curves for pitching moment implies that the neutral point for the QUADPAN prediction was slightly aft of that measured in the wind tunnel.

The correlation shown in Figure 21 is for a Mach number of 0.4. Even though QUADPAN is basically an incompressible code, it is still quite effective at higher Mach numbers as shown in Figure 22. In this figure, data and predictions are shown for the PTA model at Mach 0.7. It can be seen that the lift curve is not predicted quite so precisely as for the simpler configuration at the lower Mach number, but the disagreement is

PRECEDING PAGE BLANK NOT FILMED

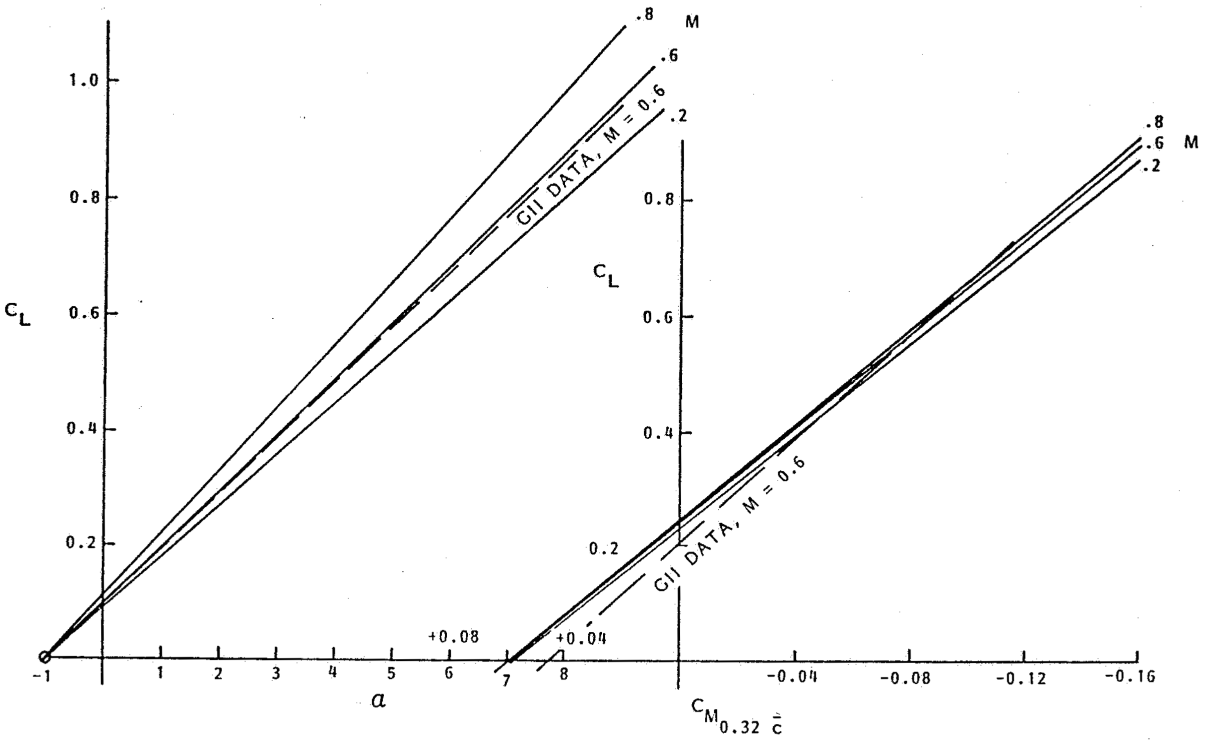

Figure 20. Comparison of QUADPAN Predictions with GII Data

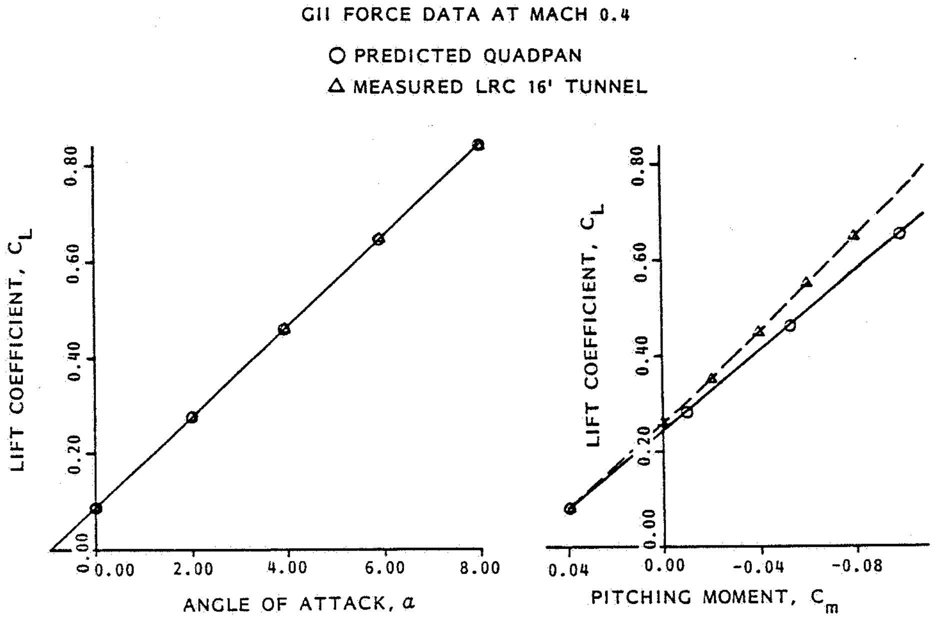
GII FORCE DATA AT MACH 0.4

Figure 21. Lift/Pitching Moment Correlation with Theory - GII

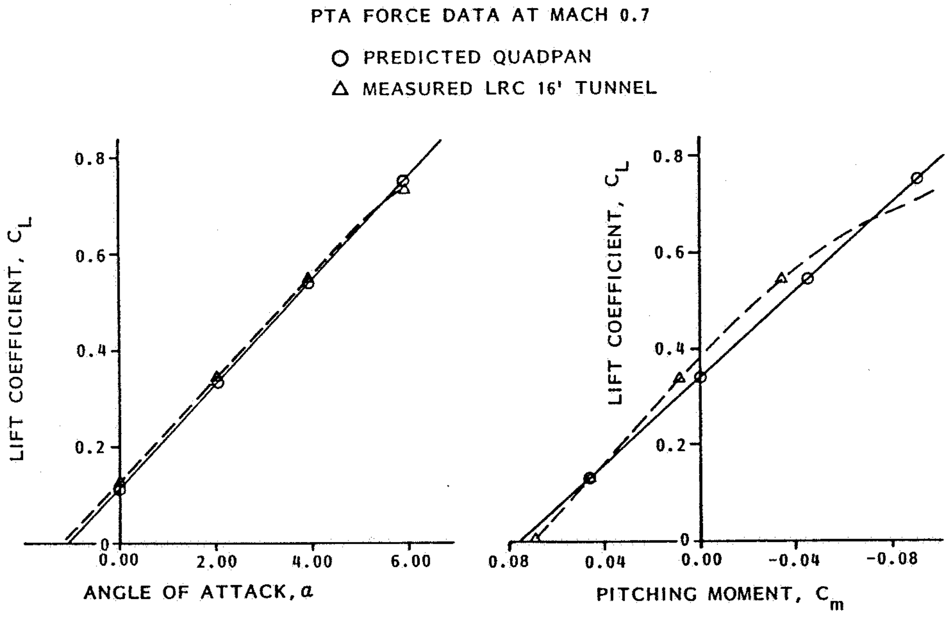
PTA FORCE DATA AT MACH 0.7

Figure 22. Lift/Pitching Moment Correlation with Theory - PTA

believed to be due more to the additional complexity of the PTA model than to the higher Mach number. Again, the pitching moment curve is not predicted as well as the lift curve, but the agreement is still good.

The excellent correlations of Figures 20 through 22 give confidence in the validity of the wind tunnel data and the ability of the QUADPAN code as a tool for interpretation and extrapolation of data.

7.1.1.2 Configuration Buildup

Figure 23 shows the manner in which buildup of the model from the GII to the PTA configuration affects lift. The data are shown for Mach 0.8 where the effects of tip and acoustic booms, if any, would be expected to be evident. The data of Figure 23 show that only the addition of the nacelle to the GII wing has any noticeable effect on the lift characteristics. The PTA nacelle increases configuration lift slightly at low angles of attack, and decreases lift slightly at angles of attack above 3 degrees.

Figure 24 shows that the trend observed at Mach 0.8 appeared at lower Mach numbers also. At Mach 0.4 and 0.17 the PTA nacelle increased lift at low angles of attack but resulted in a slight loss of lift at the higher angles.

The effects of flaps on lift are shown for the GII model in Figure 25 and for the PTA model in Figure 26. The adverse effect of the PTA configuration on maximum lift coefficient is evident for takeoff flaps but is not seen for landing flaps.

7.1.1.3 Effects of Mach Number

The effects of Mach number on the lift characteristics of the PTA model are summarized in Figure 27. Increasing Mach number increased α for zero lift, increased the slope of the lift curve, and decreased lift at the higher angles of attack.

7.1.1.4 Effects of the Propfan

Thrust coefficients available for the high-speed tests were low, and the propfan effects on lift that were measured were insignificant. At low speeds, however, a wide range of thrust coefficient values were available, and significant effects were observed. These will be discussed fully in Section 7.3 STABILITY AND CONTROL. Suffice it to say in this section that both lift and lift curve slope increase with increasing propfan thrust with most of this increase in lift attributed to the effect of increased velocities in the slipstream.

7.1.2 Drag

Drag polars for the GII model in the low-speed wind tunnel are shown in Figure 28. The several curves show the model in the tail-off, vertical-tail-only, and tail-on configurations. Also plotted in Figure 28 is a drag polar from published GII aircraft flight performance data at Mach 0.20. In the range of lift coefficients from 0.1 to 0.6, it can be seen that the low-speed wind tunnel data give GII drag about 10 to 40

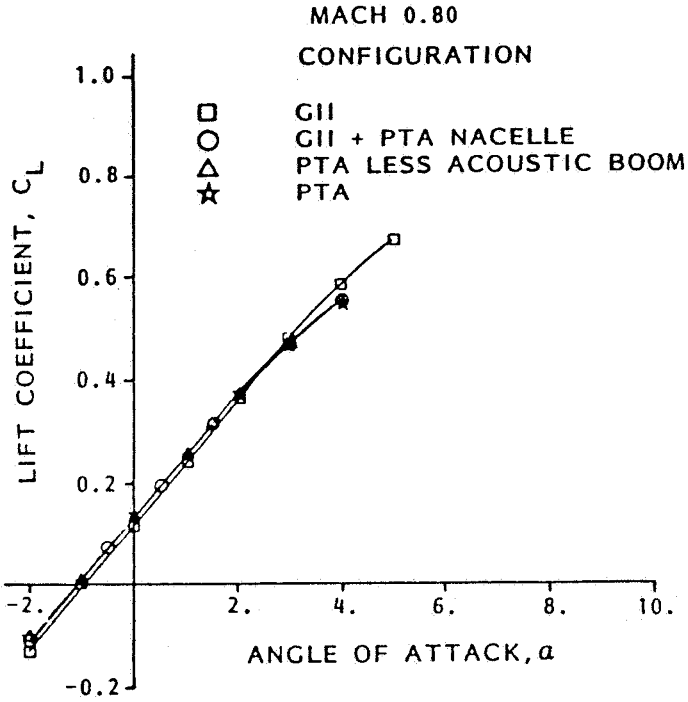

Figure 23. Lift Curves for PTA Buildup

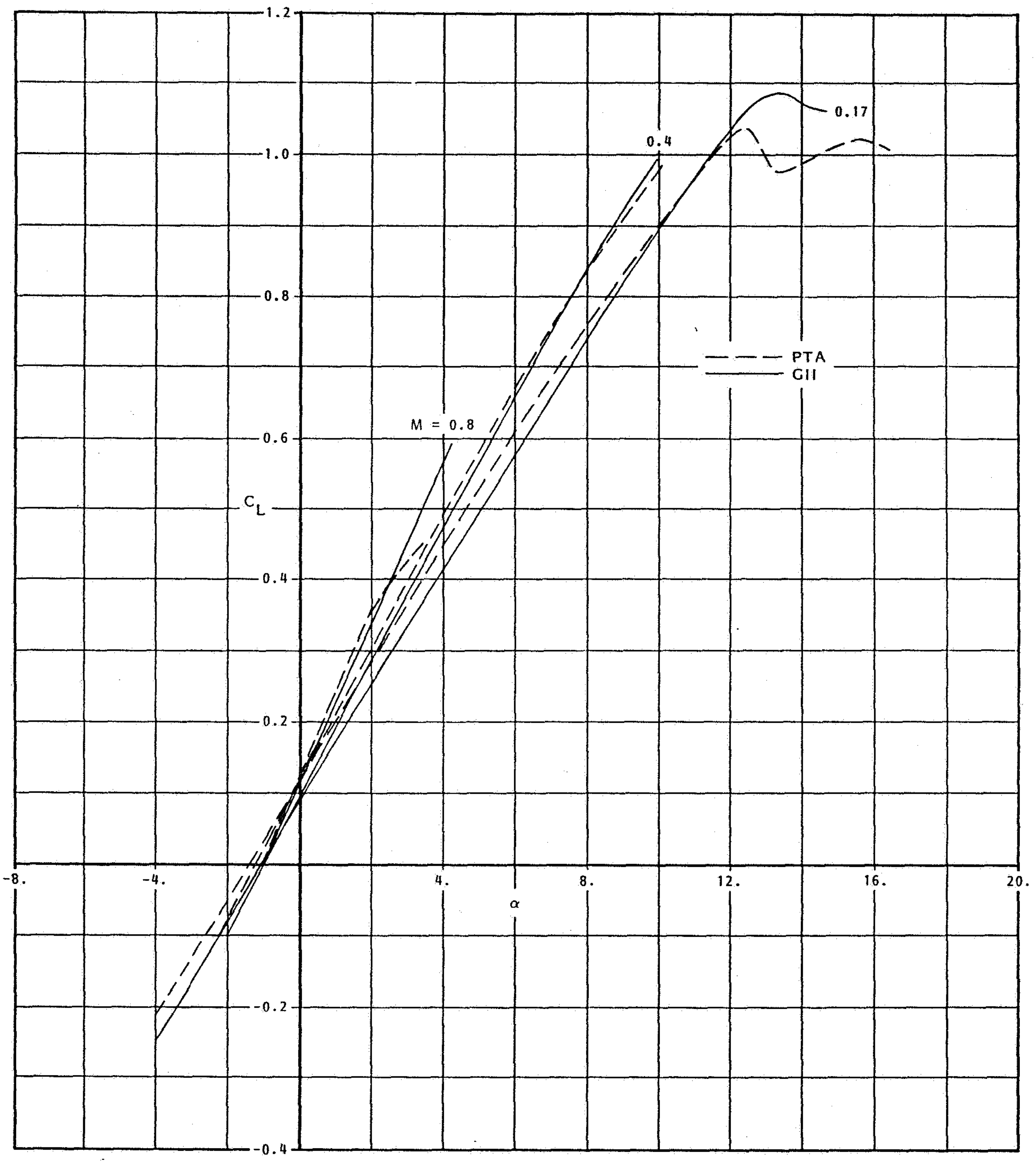

Figure 24. PTA Lift Coefficients at Several Mach Numbers

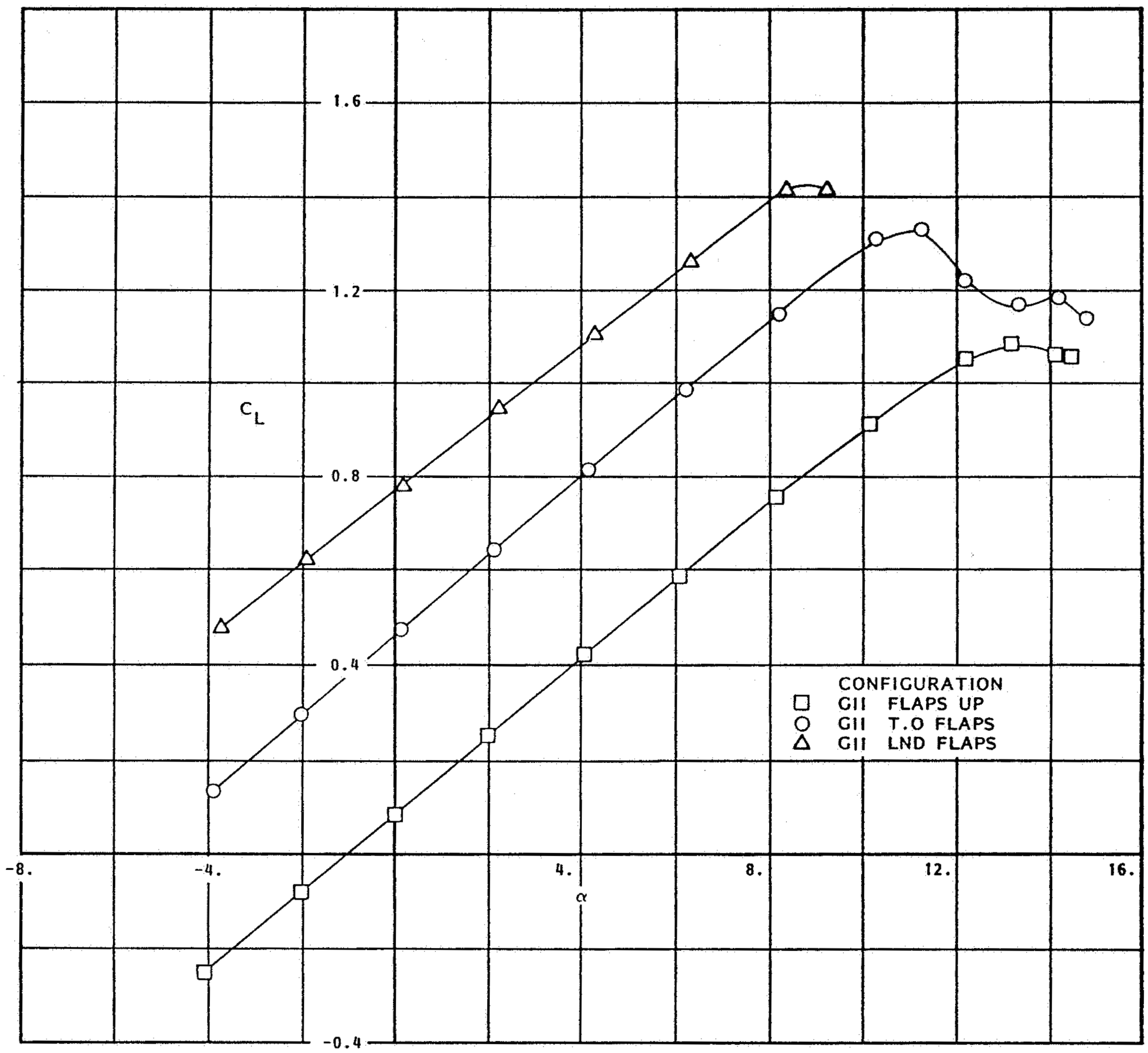

Figure 25. Effect of Flaps on Lift - GII

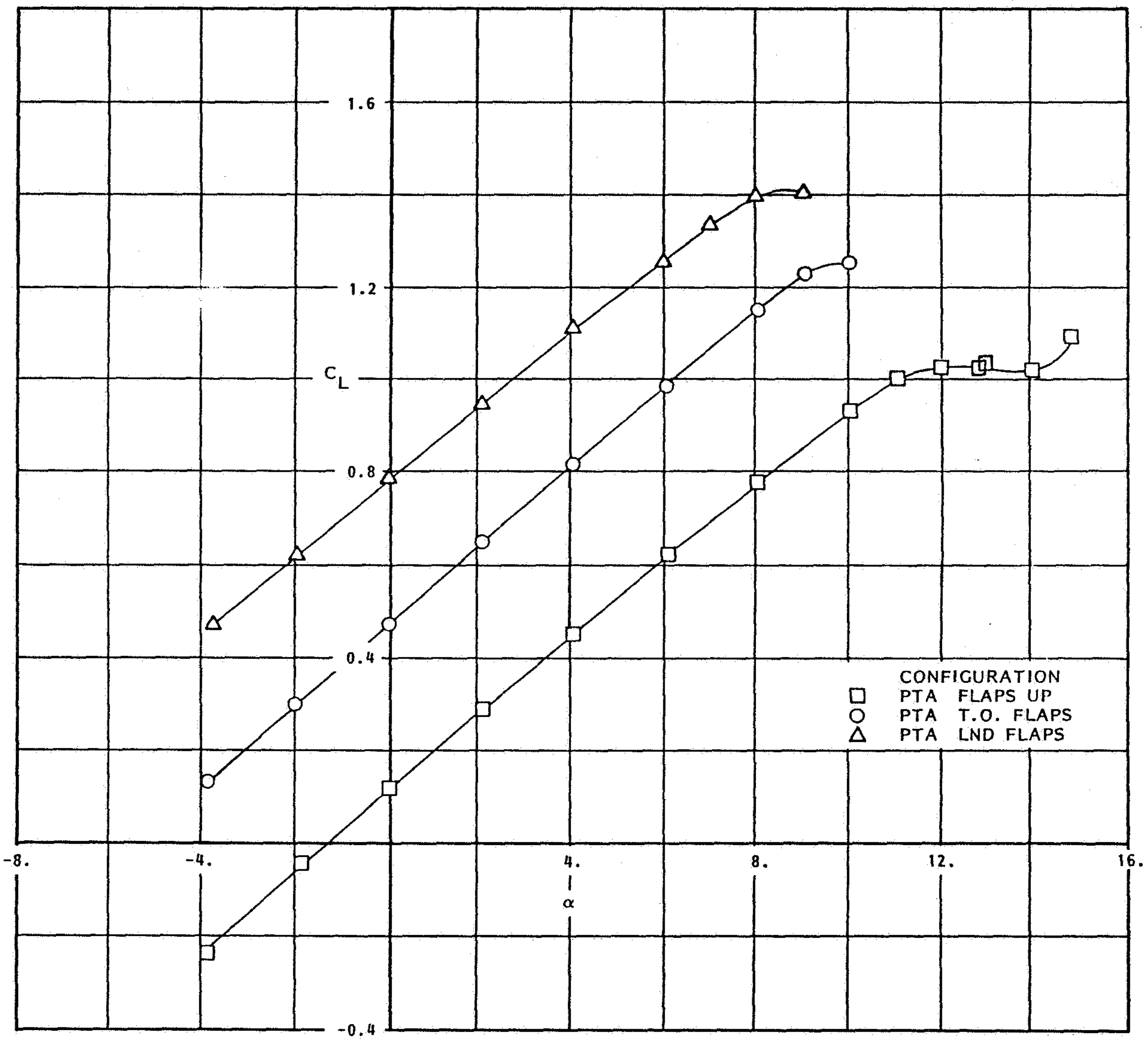

Figure 26. Effect of Flaps on Lift - PTA

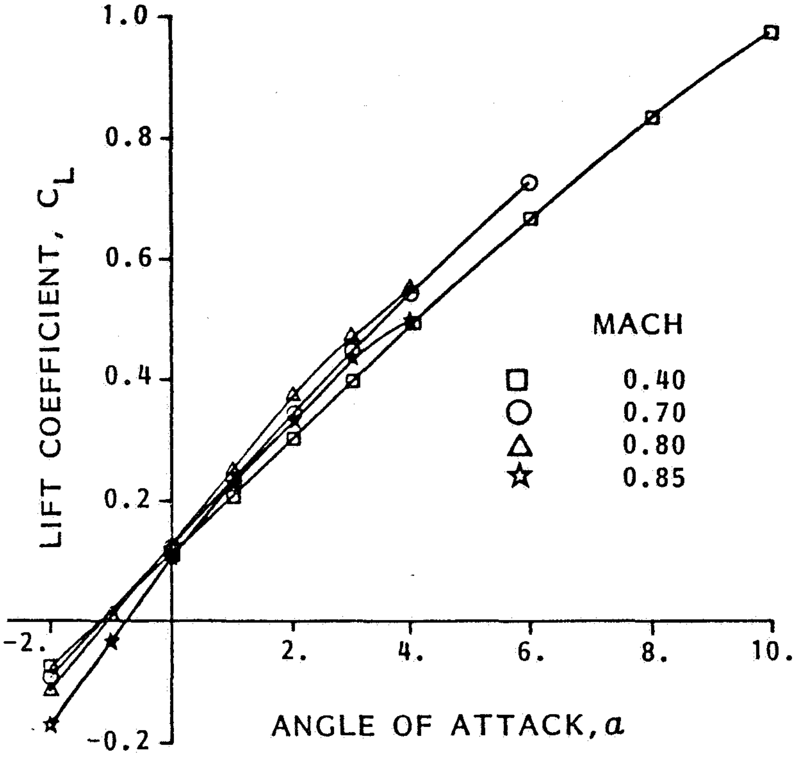

Figure 27. Effect of Mach Number on PTA Lift

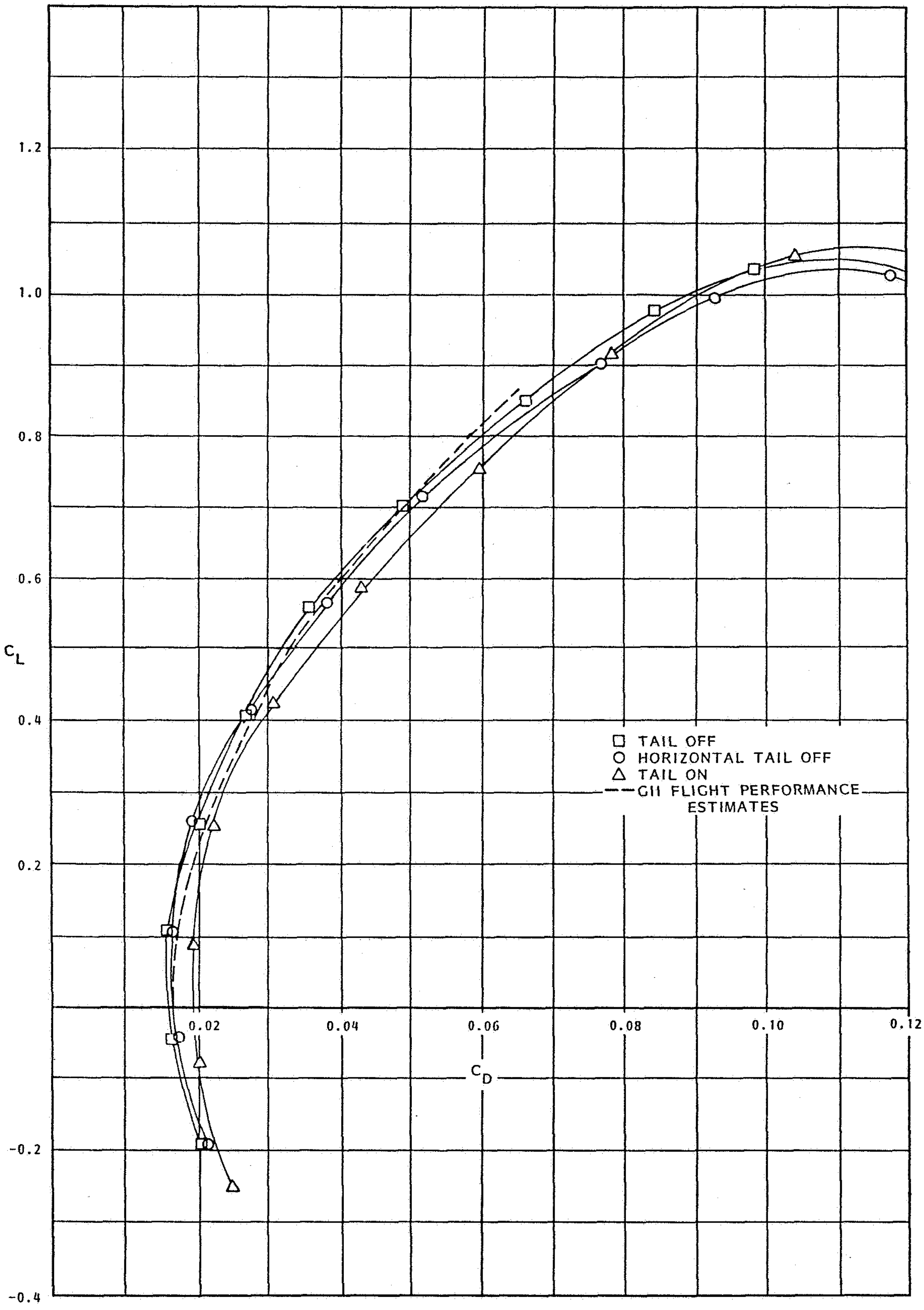

Figure 28. Drag Polars for GII

counts higher than the flight estimates. This is considered to be reasonable agreement. It shows the wind tunnel drag to be higher than flight drag as would be expected, but at approximately the same level. An increment of about 20 counts would be expected for the difference in Reynolds numbers between the two cases.

The effects of adding the PTA nacelle to the GII aircraft are shown in Figure 29. At zero lift, the impact of the nacelle is to add about 30 counts of drag, but in the range of lift coefficients from 0.1 to 0.3, the nacelle adds about 20 to 25 counts of drag.

Figure 30 shows the additional drag increment due to the addition of the wing tip booms. Over the range of moderate lift coefficients, the booms add about 20 counts of drag. The acoustic boom was not added to the low-speed model because results from the high-speed tunnel tests had already shown the drag of this addition to be negligible. The total increment due to PTA modifications from the low-speed wind tunnel tests is approximately 40 to 45 counts of drag.

Because Reynolds numbers were higher in the high-speed wind tunnel tests, it would be expected that drag increments from the high-speed tests would be smaller than those from the low-speed tests. This can be seen in Figure 31 where drag increments for the PTA buildup are plotted against Mach number. These data show a drag creep effect at Mach numbers above 0.6 and a sharp transonic drag rise above Mach 0.7.

The effect of Mach number on drag polars for the PTA model is shown in Figure 32. In this figure, the influence of lift coefficient on the onset of transonic drag rise can be seen.

In the PTA Program, provisions were made for varying nacelle incidence in order that inflow angle to the propfan could be varied over a wide range. The effects of nacelle incidence on drag are shown in Figure 33. Drag appears to be unaffected by changes in nacelle incidence from -1 to +2 degrees, but increases significantly when nacelle tilt is changed to -3 degrees.

The effects of flaps on PTA model drag are shown in Figure 34 where drag polars are shown for flap angles of 0, 20, and 40 degrees, and for both the GII and the PTA models. Drag performance with flaps is not greatly affected by the addition of the PTA modifications.

7.2 PRESSURE DISTRIBUTIONS

The flow field around a propeller nacelle installed on a swept wing is quite complex. Therefore, the PTA model was instrumented with a number of pressure ports on the nacelle and on the wing near the nacelle, so that the flow fields could be interpreted and the analytical tools used in design could be evaluated.

Figure 35 shows a comparison of predicted and measured pressures on the nacelle. The wire diagrams at the top of the figure show the analytical model, and the shaded areas show the location of panels where pressure was computed. For this propeller-off, Mach 0.4 condition, it can be seen that the analytical method did an excellent job of predicting experimental results.

Figure 36 shows a comparison of prop-on wind tunnel data with predicted values for pressures on the wing just inboard and just outboard of the nacelle. On the inboard side, the additional upwash caused by the

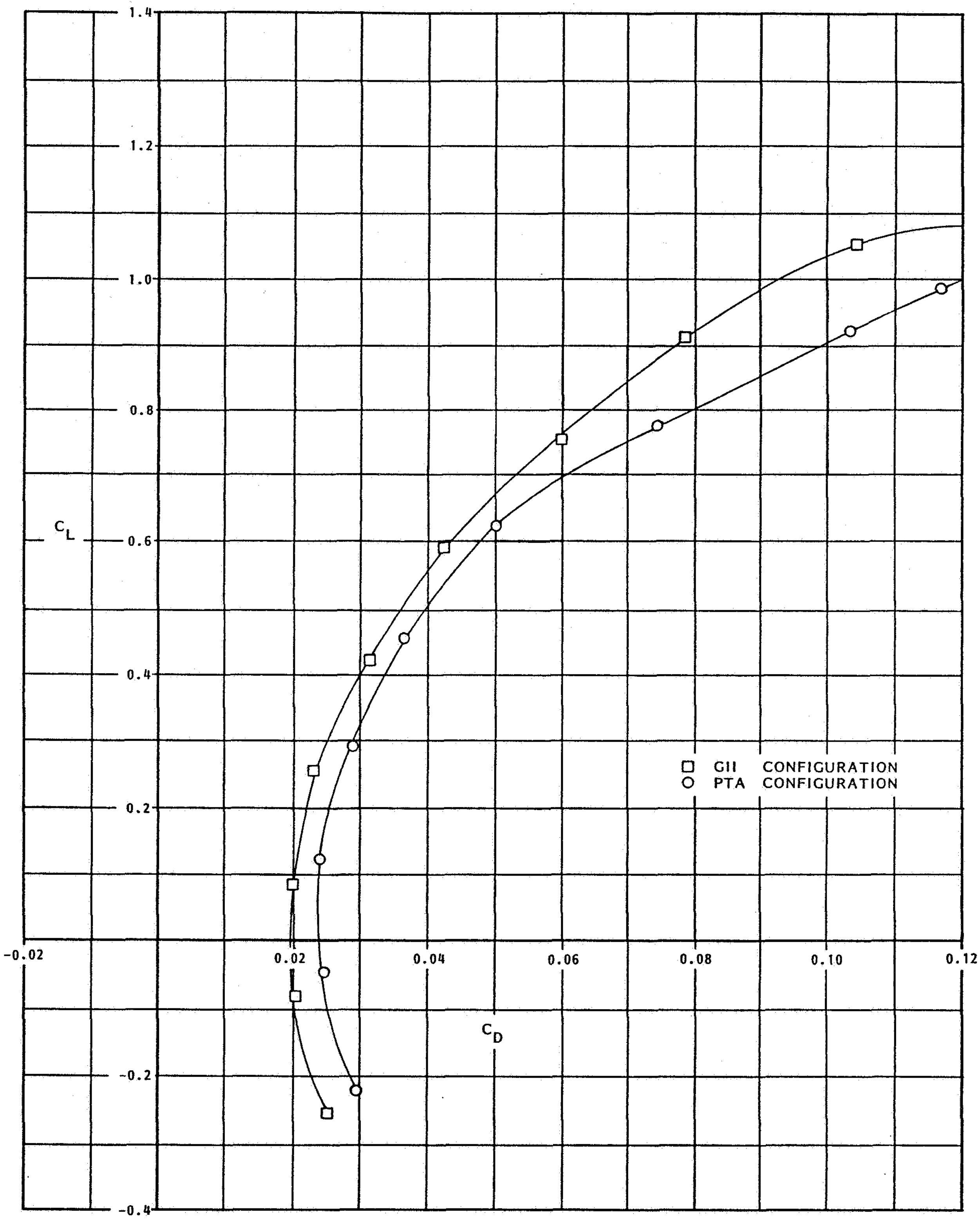

Figure 29. Power-Off Drag of PTA Nacelle

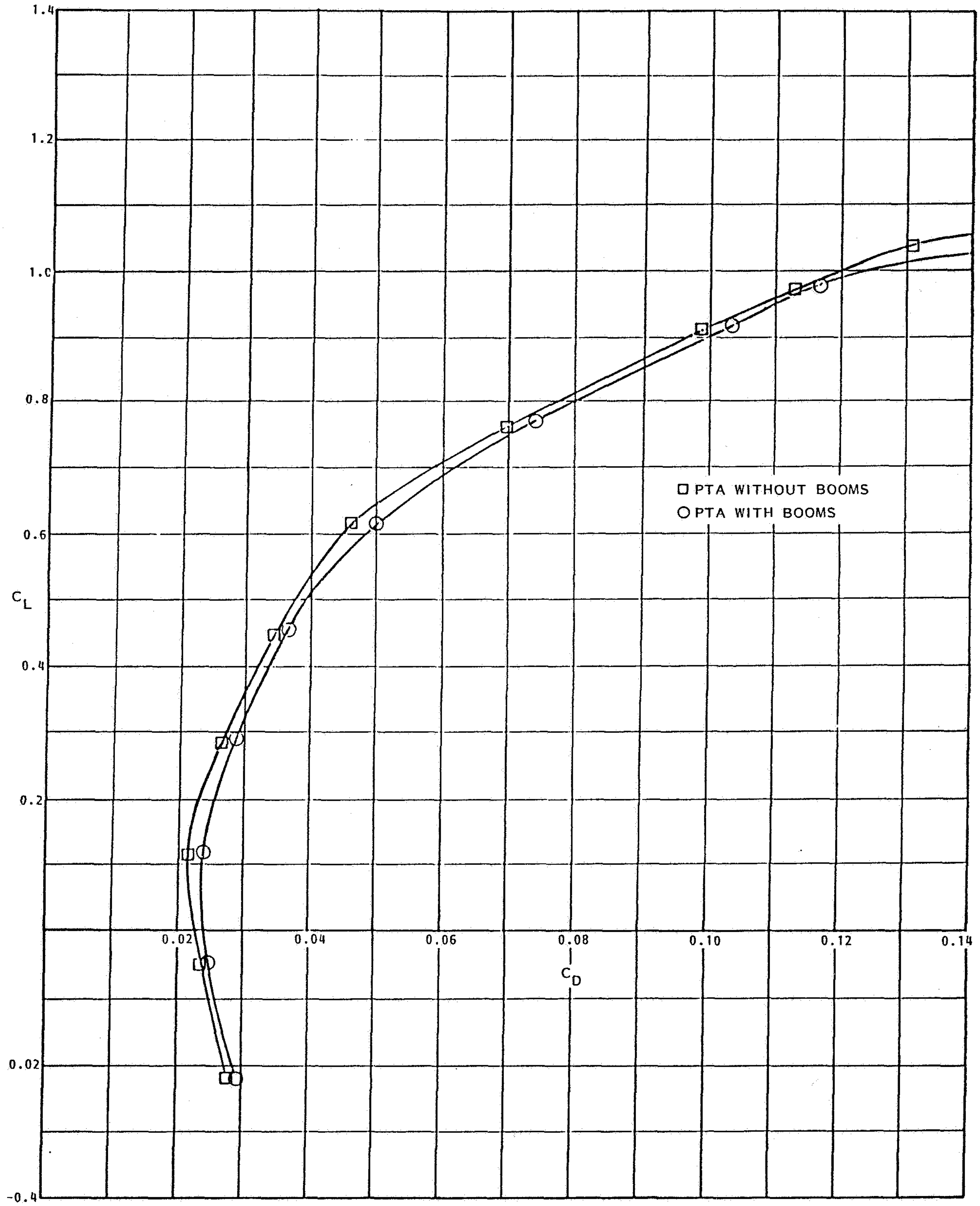

Figure 30. Drag of Tip Booms

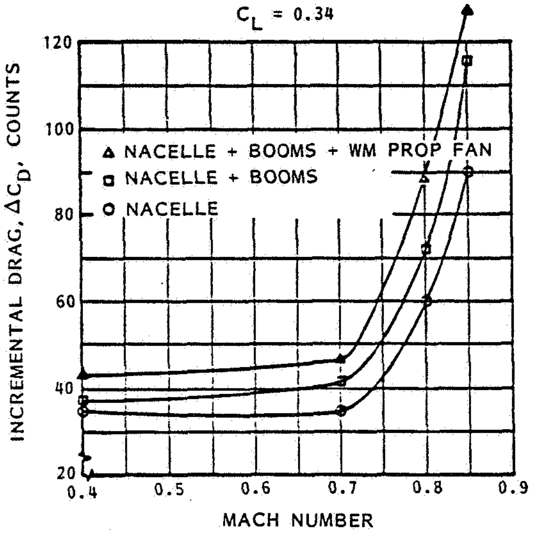

Figure 31. Drag of PTA Components at High Speed

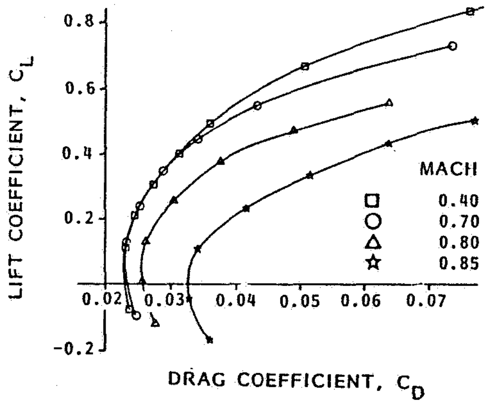

Figure 32. Effect of Mach Number on PTA Drag Polars

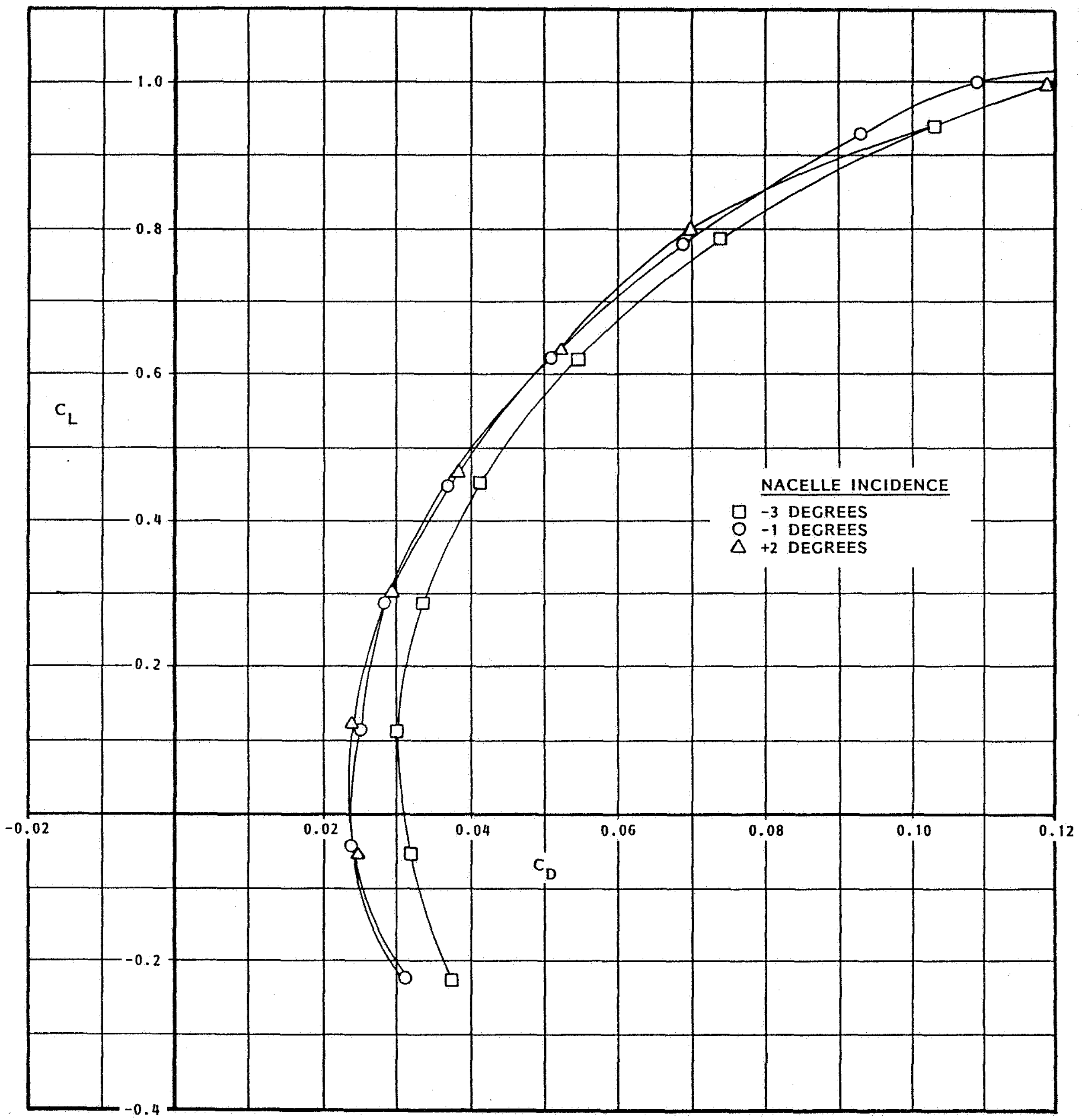

Figure 33. Effect of Varying Nacelle Incidence on Drag

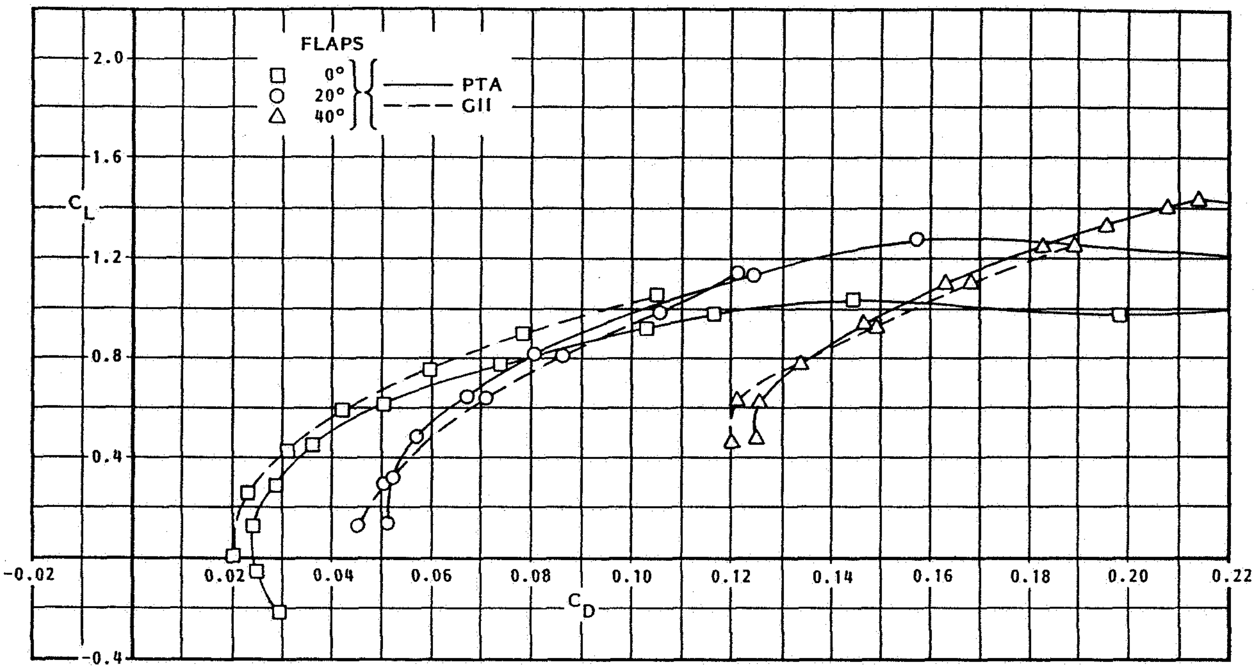

Figure 34. Effects of Flap Deflection on Drag

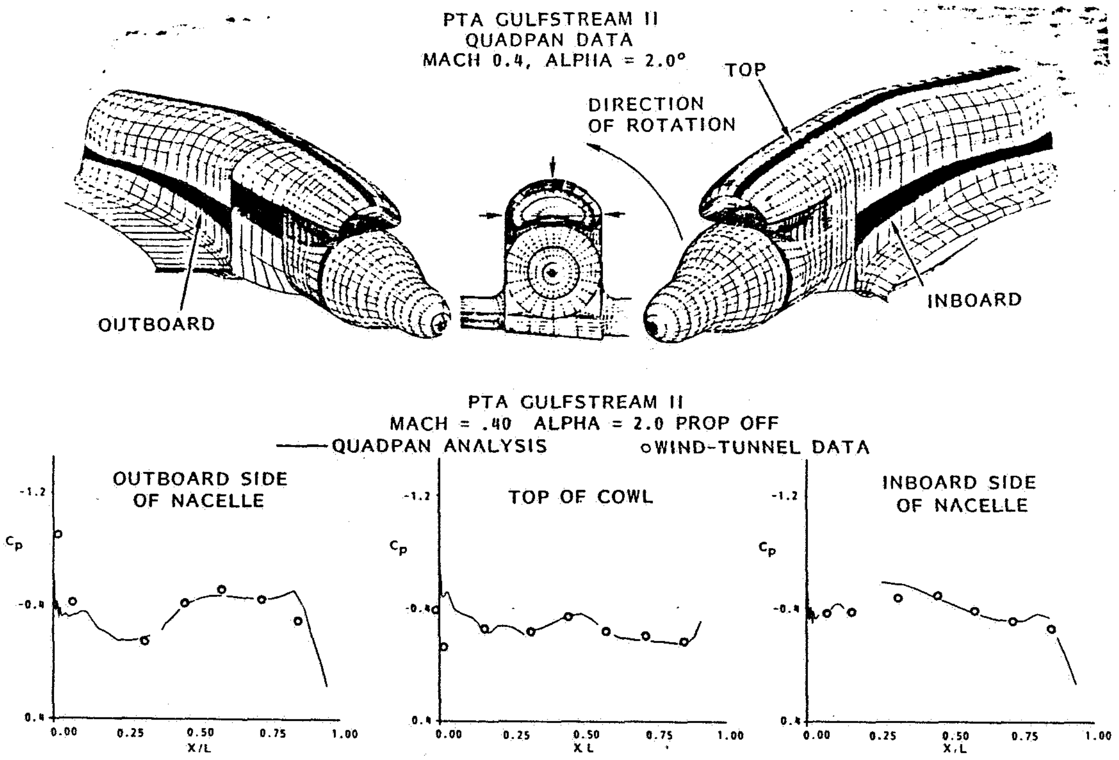

Figure 35. Nacelle Surface Pressure Distributions - Prop-Off

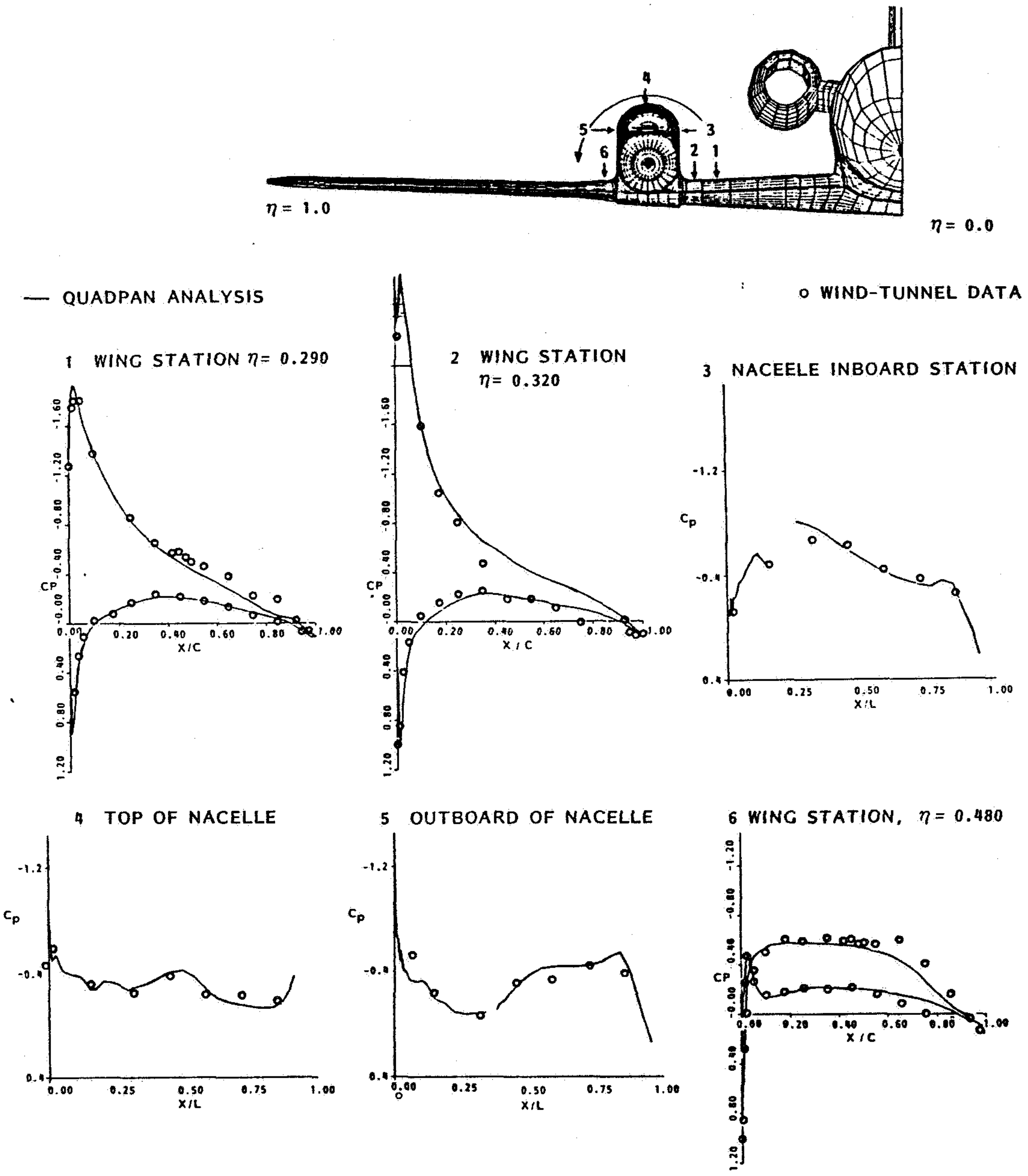

Figure 36. Wing Surface Pressure Distributions - Mach 0.4

slipstream swirl gives rise to pressure suction peaks in the leading edge region of the wing. On the outboard side the downwash on the lower surface gives rise to suction peaks in the lower surface leading edge region. Predictions at Mach 0.4 are in excellent agreement with the test data. On the inboard side, the magnitude of the suction peak is accurately predicted. The inadequacies of QUADPAN paneling at the trailing edge with vanishing strips, however, gives localized erroneous pressure coefficients.

Outboard of the nacelle, correlation of theory and experimental data is equally good. This correlation shows that the QUADPAN analysis predicts quite accurately the flowfield at subsonic Mach numbers on the complex geometry of the integrated wing/nacelle combination. In addition, the agreement indicates that the predicted slipstream has the correct induced velocity and swirl distribution for the operating advance ratio and blade angle setting.

At the higher Mach number of 0.7, Figure 37 shows that the velocity in the channel between the nacelle and the fuselage accelerates to supersonic values with the pressure peak moving aft and then decelerates through a weak shock wave. QUADPAN predicts the suction peak, but cannot predict the supersonic flow behind the peak.

Figures 38 and 39 show that the analysis program was effective for predicting prop-on flow around the nacelle at Mach numbers of 0.7 and 0.8, respectively. Again, however, since QUADPAN is not a transonic code, the flow prediction on the inboard side of the nacelle is not so good where the swirling slipstream increases local angle of attack and creates local regions of supersonic flow.

Figure 40 shows wing surface pressures just inboard and just outboard of the PTA nacelle location for the GII and PTA models. On the inboard side of the nacelle, the effect of the nacelle causes a local acceleration near the wing leading edge. There is, however, no evidence of any significant flow separation. On the outboard side of the nacelle, the primary effect of the nacelle appears to be a lowering of the local angle of attack and a slight reduction in lift.

Similar data are shown in Figure 41 for a Mach number of 0.8. Here it can be seen that some shock waves are formed on both inboard and outboard sides of the nacelle. The higher local Mach numbers on the inboard side of the nacelle result in part from the unsweeping effect of the nacelle on the wing and in part from the acceleration in the channel formed by the nacelle, wing, and fuselage. These effects probably account for most of the PTA drag increment at the higher Mach numbers.

The effects of angle-of-attack change on the PTA wing chordwise pressure distributions at Mach 0.8 are shown in Figure 42. As is normal with an increase in angle of attack, flow velocities are increased over the wing and decreased under the wing--resulting in increased circulation lift. It would be expected that an increase in drag would accompany this lift increase--moderate at low angles of attack but increasing rapidly as angle of attack increases. Calculations confirm that, in the angle of attack range from zero to about three degrees, the lift-to-drag ratio was approximately 10, but dropped to 8.5 at angle of attack of 4 degrees.

The effect of increasing Mach number is shown in Figure 43. Below the critical freestream Mach number, the suction peak is close to the wing leading edge and increases with Mach number. In this range, the flow

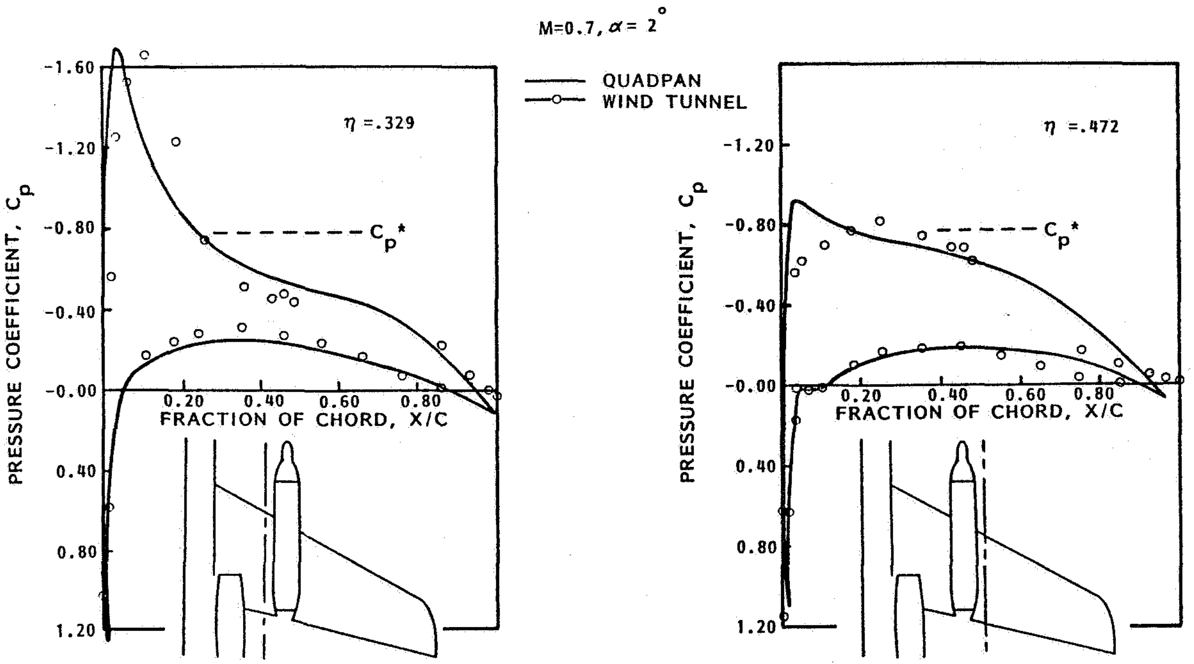

Figure 37. Wing Surface Pressure Distributions - Mach 0.7

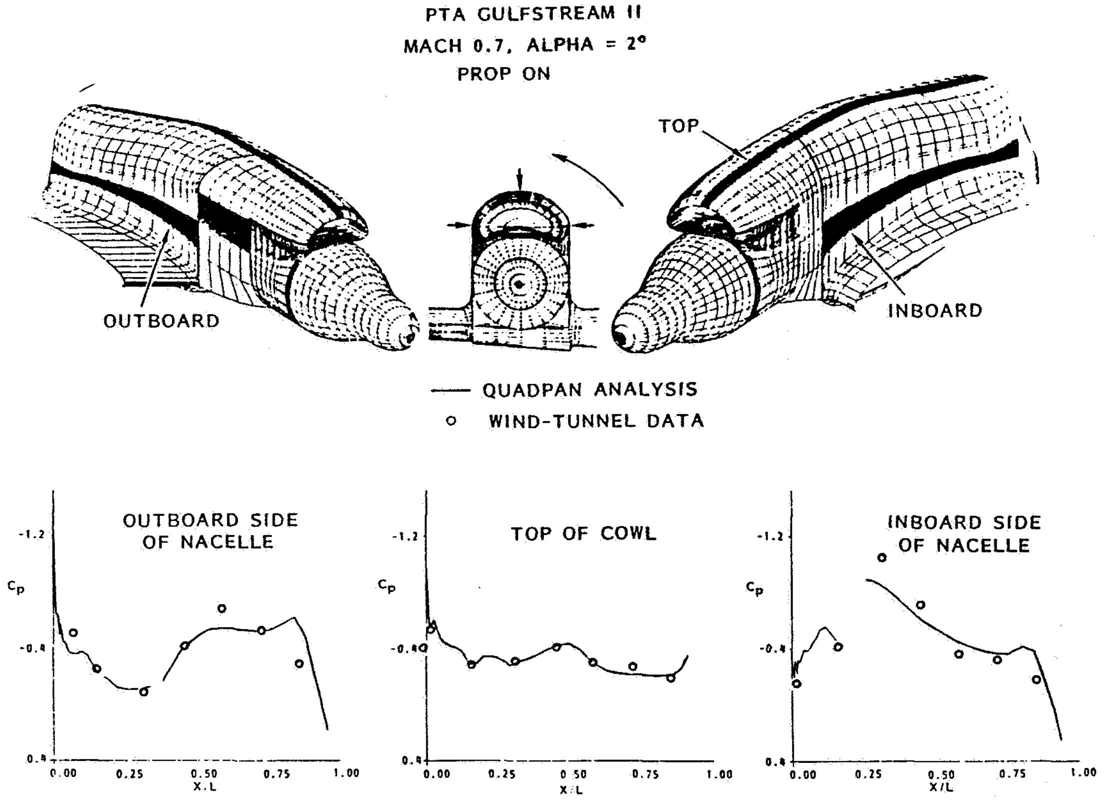

Figure 38. Nacelle Surface Pressure Distributions - Prop-On, Mach 0.7

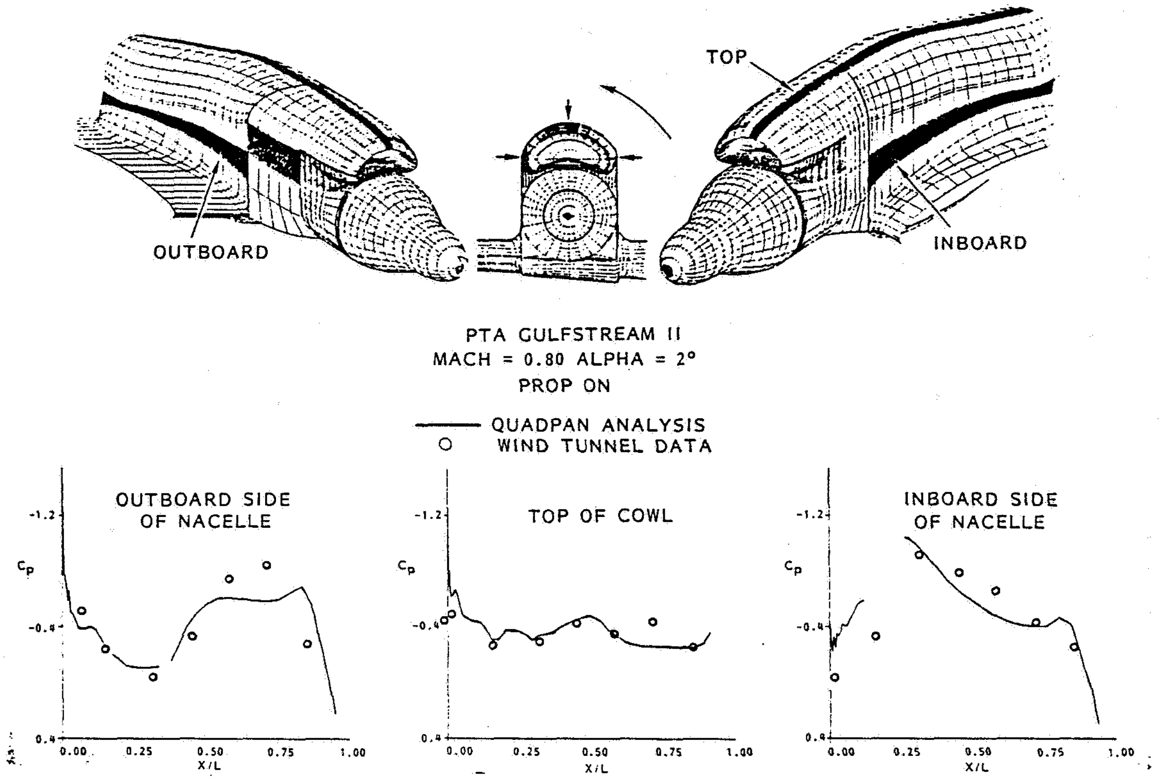

Figure 39. Nacelle Surface Pressure Distributions - Prop-On, Mach 0.8

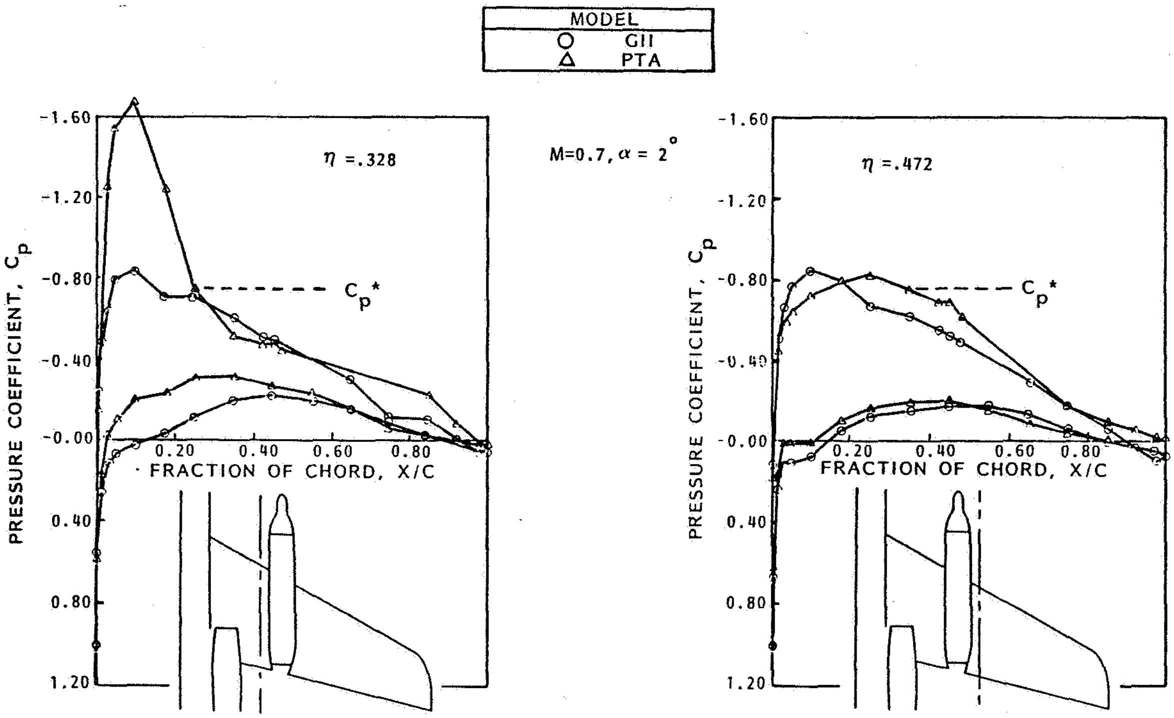

Figure 40. Effect of PTA Nacelle on Wing Section Pressures-Mach 0.7

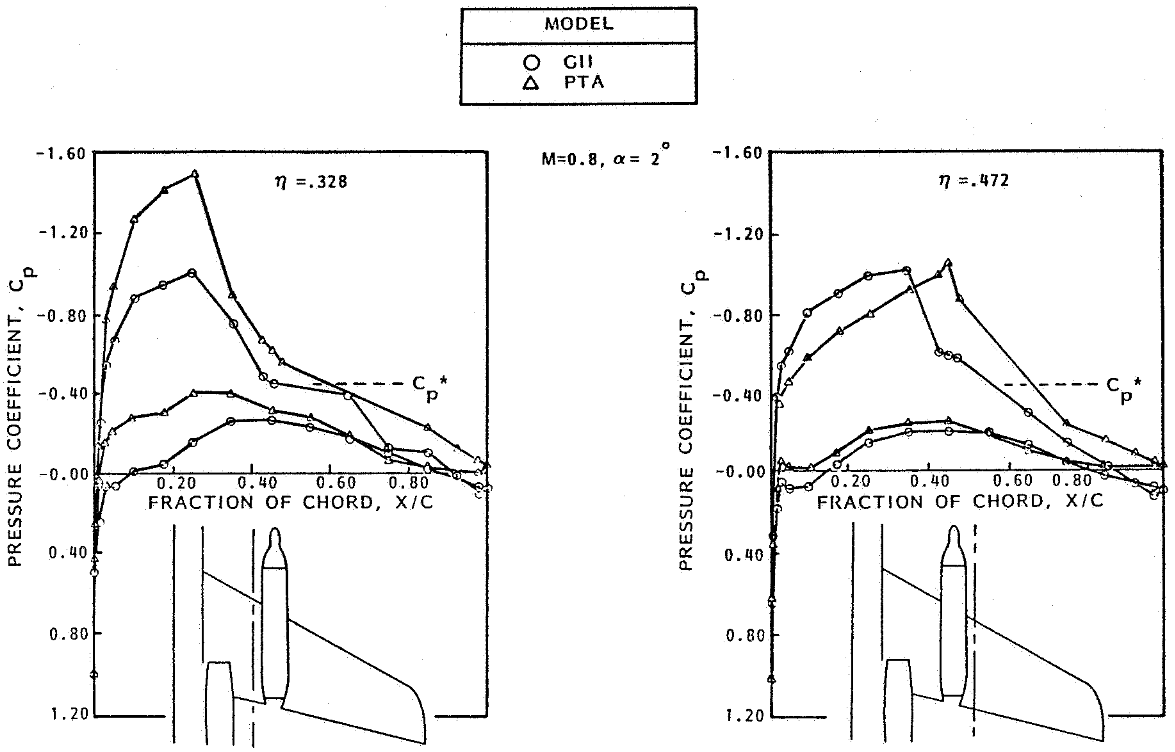

Figure 41. Effect of PTA Nacelle on Wing Section Pressures-Mach 0.8

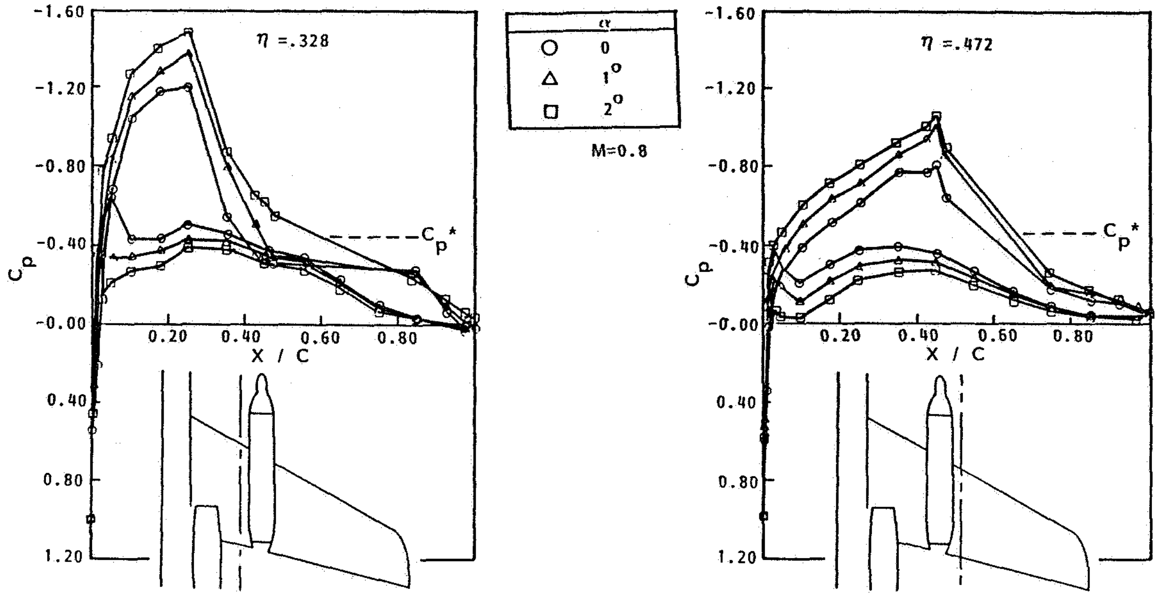

Figure 42. Effect of Angle of Attack on Wing Section Pressures

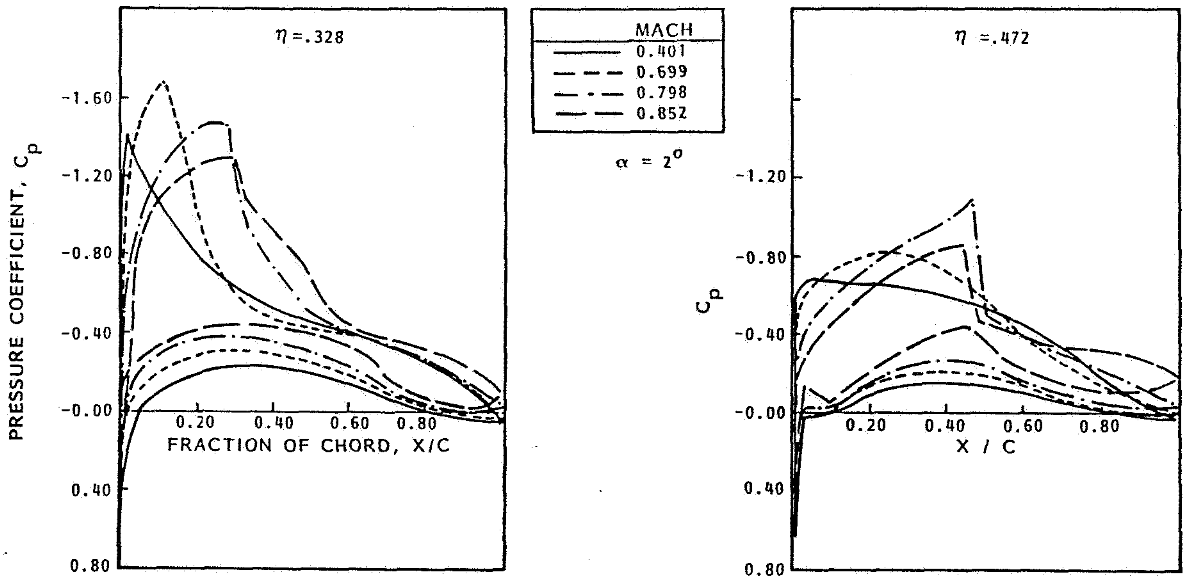

Figure 43. Effect of Mach Number on Wing Section Pressures

behind the peak recompresses gradually with no signs of flow separation. Above the critical Mach number, however, the suction peak moves aft and the flow recompresses through a shock wave that becomes stronger with increasing Mach number. In this range, there is danger of flow separation due to the strong interaction between the shock wave and the boundary layer. At Mach 0.8, there is no evidence of extensive separation, although there may be some locally at the foot of the shock. At Mach 0.85, however, there is evidence of separation at the trailing edge that causes the shock wave to move forward. This is evident in the pressure distributions on the outboard side of the nacelle where separation first occurs. The wing lower surface pressures also decrease with increasing Mach number, and at Mach 0.85, sonic velocities are reached outboard of the nacelle and terminate through a shock wave. This transonic behavior is responsible for the drag rise that starts at about Mach number 0.7.

7.3 STABILITY AND CONTROL

In this section, aerodynamics data from the wind tunnel tests are presented and discussed from the standpoint of the impact of these data on stability and control of the PTA configuration. It was intended that wind tunnel data would be used in the PTA aircraft design by adding the wind-tunnel-derived force and moment increments to full-scale GII data supplied by Gulfstream Aerospace Corporation. In the analysis and discussion, therefore, major emphasis is placed on increments between GII and PTA models. It should be remembered that the PTA wind tunnel model was a mirror image of the PTA aircraft--with the nacelle on the right-hand wing in the wind tunnel instead of the left.

7.3.1 Lift and Pitch - Low Speed

The low-speed lift and pitching moment coefficients for the PTA model in the clean, takeoff, and landing configurations, in the "ferry" mode, and with a feathered propfan, are compared with the GII in Figure 44.

In the clean configuration, the major changes due to the PTA installation were an almost constant increase in lift coefficient, over the operational range of angle of attack, and a small reduction in maximum lift coefficient at a lower angle of attack. Very little effect is shown due to the addition of a feathered propeller. The pitching moment data show no effect on C_{MO} but a significant destabilizing effect on dC_M/dC_L that is further increased by the feathered propeller. These effects are a result of lift generated on the nacelle forward of the center of gravity and the resultant changes in wing lift due to the nacelle and tip booms.

In the takeoff flap configuration, a similar lift increase occurred due to the PTA installation and a similar loss of maximum lift coefficient at a lower angle of attack. The feathered propeller reduced the lift increment in the operational angle of attack range and also further reduced the maximum lift coefficient. This reduction in lift decreases the stability level with a feathered propeller at the higher lift coefficients. A small destabilizing change in tail lift due to the nacelle contributes to this effect, but the major changes occur on the wing and nacelle.

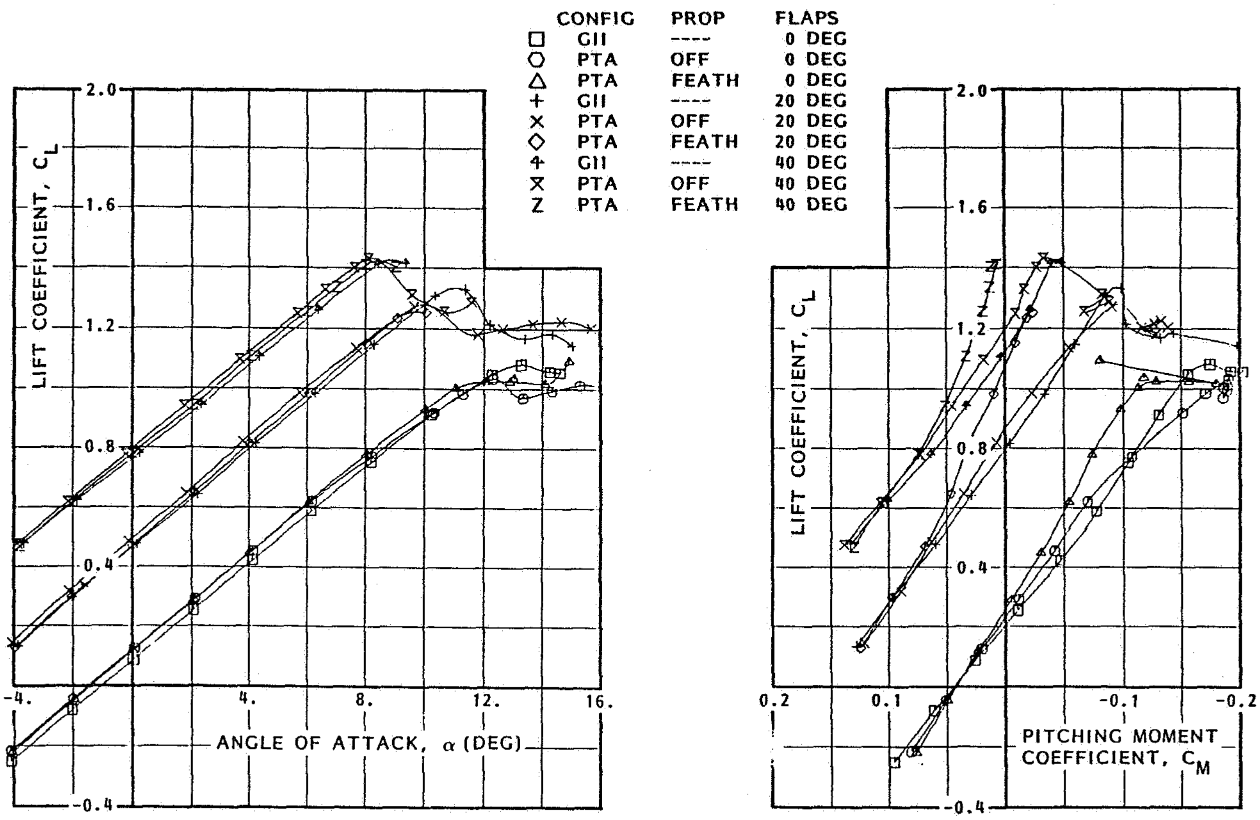

Figure 44. Effects of PTA Modifications on Lift and Pitching Moment

In the landing configuration, the lift increase due to the PTA installation remained the same as the takeoff mode, and the effect of adding feathered propellers was also the same. The maximum lift loss due to the nacelle and booms was reduced, and stall occurred at a slightly lower angle of attack. The stability decrease relative to the GII is very small, and the effect of feathered propellers is less destabilizing than the takeoff flap level.

The reduced level of static stability for the PTA configuration at all flap settings is almost exactly balanced by a forward shift in the center of gravity envelope relative to the GII. Thus, the actual minimum static stability margin remains the same as the GII at the design aft center of gravity. The reduction in maximum lift coefficient results in a slight increase in minimum operational speeds relative to the GII. These increases are of little consequence.

The effect of propfan power on lift and pitching moment, flaps up, is shown in Figure 45. The lift increment due to power increased with angle of attack and the maximum lift coefficient increased. The angle of attack for maximum lift did not change relative to the prop-off value. This effect is the result of propeller normal force and the slipstream effect on the nacelle and wing. The incremental effect of power on lift would be less than shown here for full-scale aircraft due to the change in Reynolds number, but the same trends will prevail. Pitching moment becomes more positive with power, and the stability level decreases: these levels will be slightly less at full-scale Reynolds number.

7.3.2 Lateral-Directional - Low Speed - Zero Sideslip

The low-speed side force variation with angle of attack, at zero sideslip, is shown in Figure 46 for the GII and the PTA configurations, flaps up. Small side forces are apparent for the basic GII and can be attributed to the effects of the support system and tunnel asymmetries. The addition of the nacelle and booms created a negative sideforce increment at angles of attack above zero. This increment has contributions from the nacelle, the booms, and from flow changes at the fin. The addition of the feathered propfan resulted in an increase in positive sideforce that is due to wing-body changes and a small flowfield change at the fin.

Yawing moment variation with angles of attack, at zero sideslip, was essentially zero for all operational angles of attack. The yawing moment due to nacelle drag was offset by the yawing moment due to induced side loads on the fin. The high angle of attack yawing moments are a result of low Reynolds number wing separation and would shift to higher angles at full-scale conditions.

The rolling moment effect is largely due to the lift on the nacelle and the lift induced on the wing. This rolling moment is essentially constant with angle of attack and could be easily balanced by aileron deflection for trimmed flight. On the PTA, the nacelle weight is not completely balanced, and the aircraft center of gravity is displaced to the same side as the nacelle, creating a rolling moment in the opposite direction. This mass imbalance tends to counter the aerodynamic effect so that the aircraft is self-trimming at intermediate speeds.

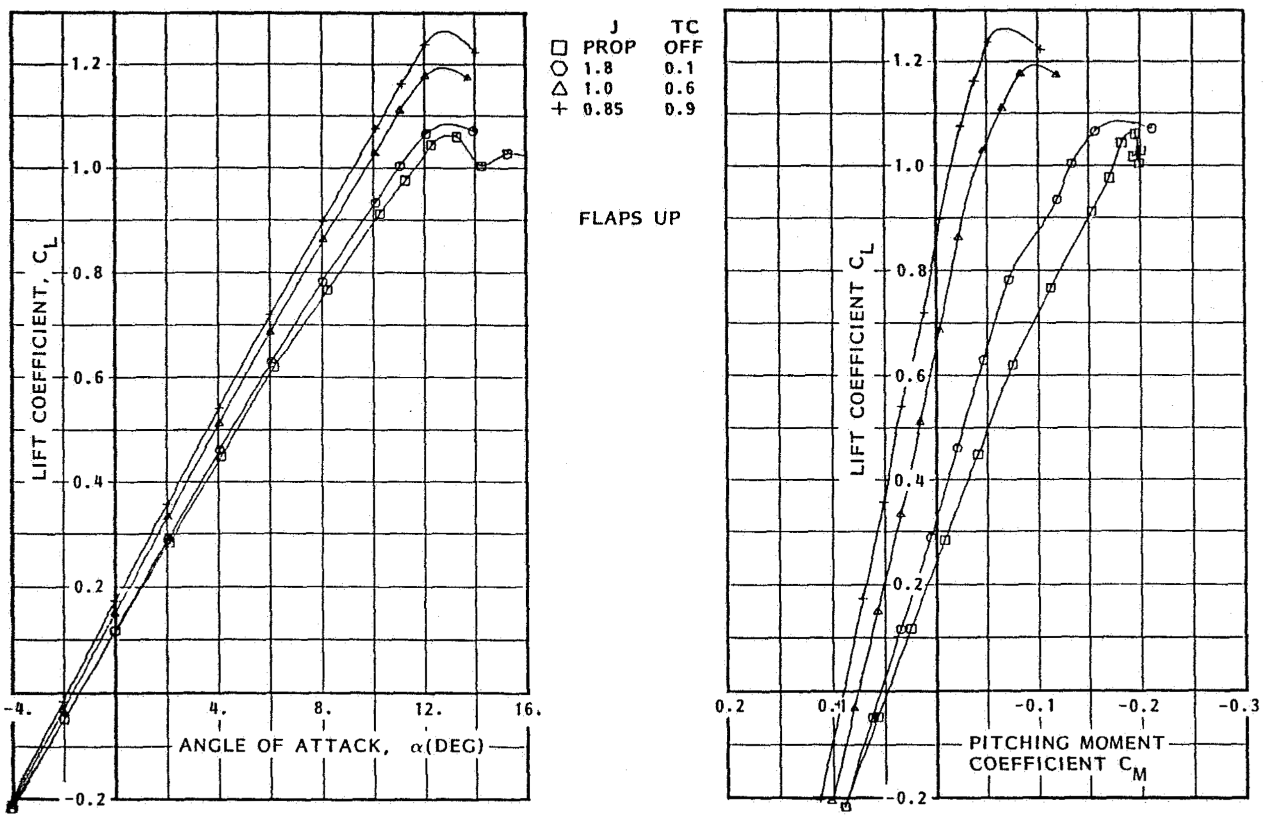

Figure 45. Effects of Propfan Power on Aerodynamic Characteristics in Pitch - Flaps Up

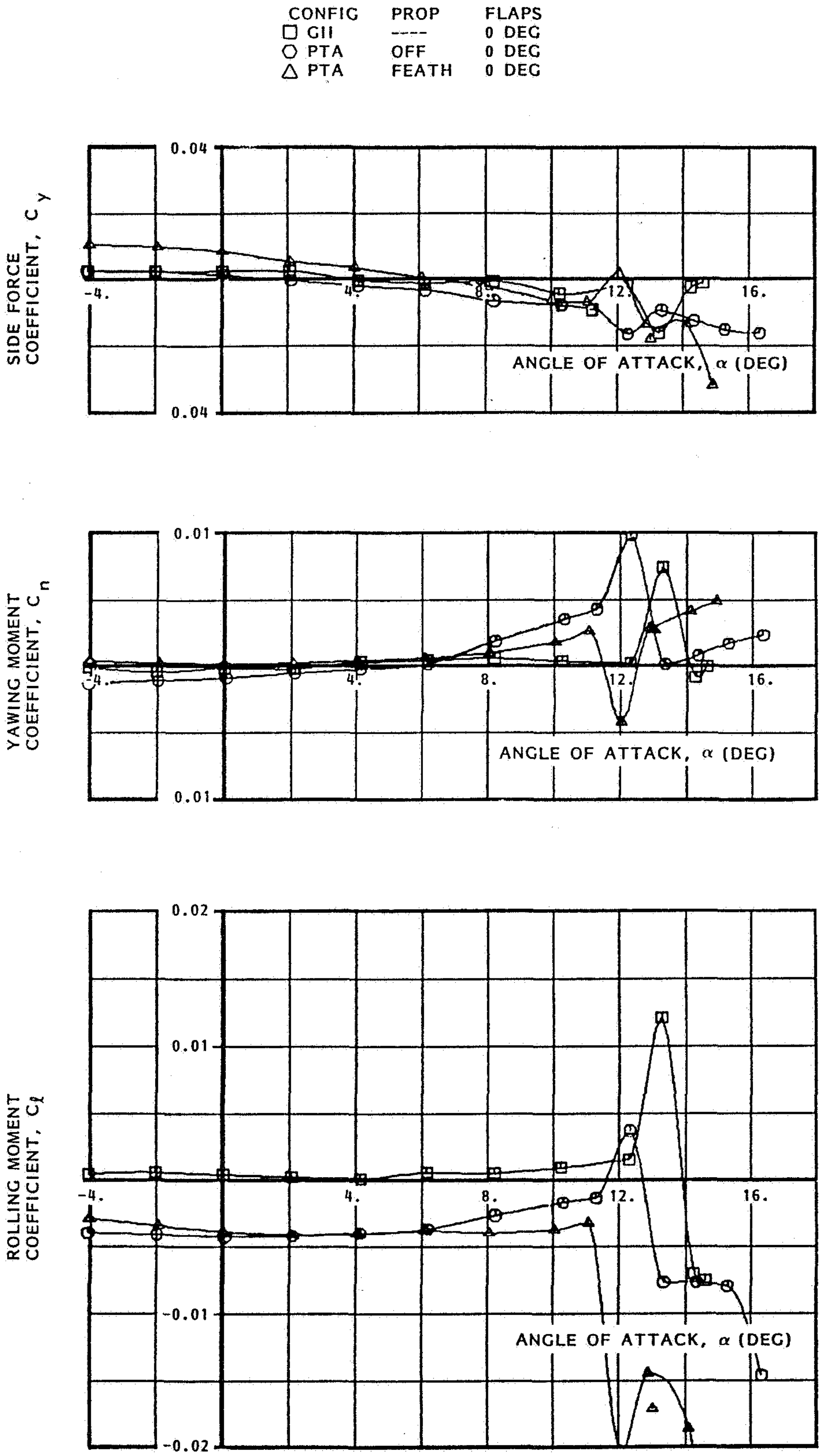

Figure 46. Effects of PTA Modifications on Side Force, Yawing Moment, and Rolling Moment - Flaps Up

With flaps down in the takeoff and landing modes, the effect of the nacelle relative to the GII is very small as shown in Figures 47 and 48. There are effects in side force and rolling moment for the GII that are the result of an unidentified asymmetry in the flap configuration that should not unduly influence the incremental effect of the PTA installation.

The effect of power on sideforce, yaw, and rolling moment as a function of angle of attack at zero sideslip is shown in Figure 49. The small offset in sideforce with propellers off rotated about an angle of attack of 4 degrees as power increased. Normal cruise angle of attack is around 3 to 4 degrees at the lower speeds associated with high power coefficients; hence, the change in bank angle required to balance the sideforce at zero sideslip would remain quite small. The data show an increase in sideforce in the negative direction with power increase that flattens to a constant value at high T_C.

The yawing moment change with power follows the increase in thrust very closely with little net aerodynamic influence. The level of yawing moment coefficient shown here at a T_C of 0.9 is very close to the maximum yawing moment available from the rudder and would therefore provide a limit on the minimum flight speed with full propfan power. However, the rolling moment due to power reached a limiting condition at a T_C of 0.6.

The rolling moment data shown in Figure 49 is made up of propeller normal force, sideforce, propeller-slipstream-induced lift on the wing, and induced loads on the fin and horizontal tail. The level increased with both angle of attack and T_C and is therefore critical to low-speed flight. For the PTA aircraft, the limiting condition for low-speed flight is based on the trim condition of no more than 50-percent wheel throw to balance the offset roll.

7.3.3 Lateral-Directional - Low Speed - Variable Sideslip

The variation of sideforce, yawing moment, and rolling moment with sideslip angle, shown in Figure 50, demonstrates the small influence of the nacelle and booms on aircraft lateral-directional stability. Relative to the GII, the sideforce variation with sideslip increased, and the yawing moment and rolling moment variation decreased. These effects are primarily due to the added nacelle side area with little or no influence from the vertical fin. The non-linearity in the rolling moment curves is a normal effect of wing load distribution changes with sideslip that decrease with increasing Reynolds number for the full-scale aircraft. The offset in roll at zero sideslip is the value for 3-degrees angle of attack and is discussed in the previous section.

The effect of power on the low-speed, lateral-directional data is shown in Figure 51. The sideforce due to sideslip (dCy/dB) was increased by propfan power due to slipstream effects on the wing and nacelle. Yawing moment due to sideslip (dCn/dB) was slightly decreased by propfan power primarily due to change in the wing loading and direct propeller effects. Rolling moment due to sideslip was reduced slightly with propfan power as a result of wing load changes. The offsets at zero sideslip in sideforce, yawing moment, and rolling moment are appropriate for 3 degrees of angle of attack and are discussed in the previous section.

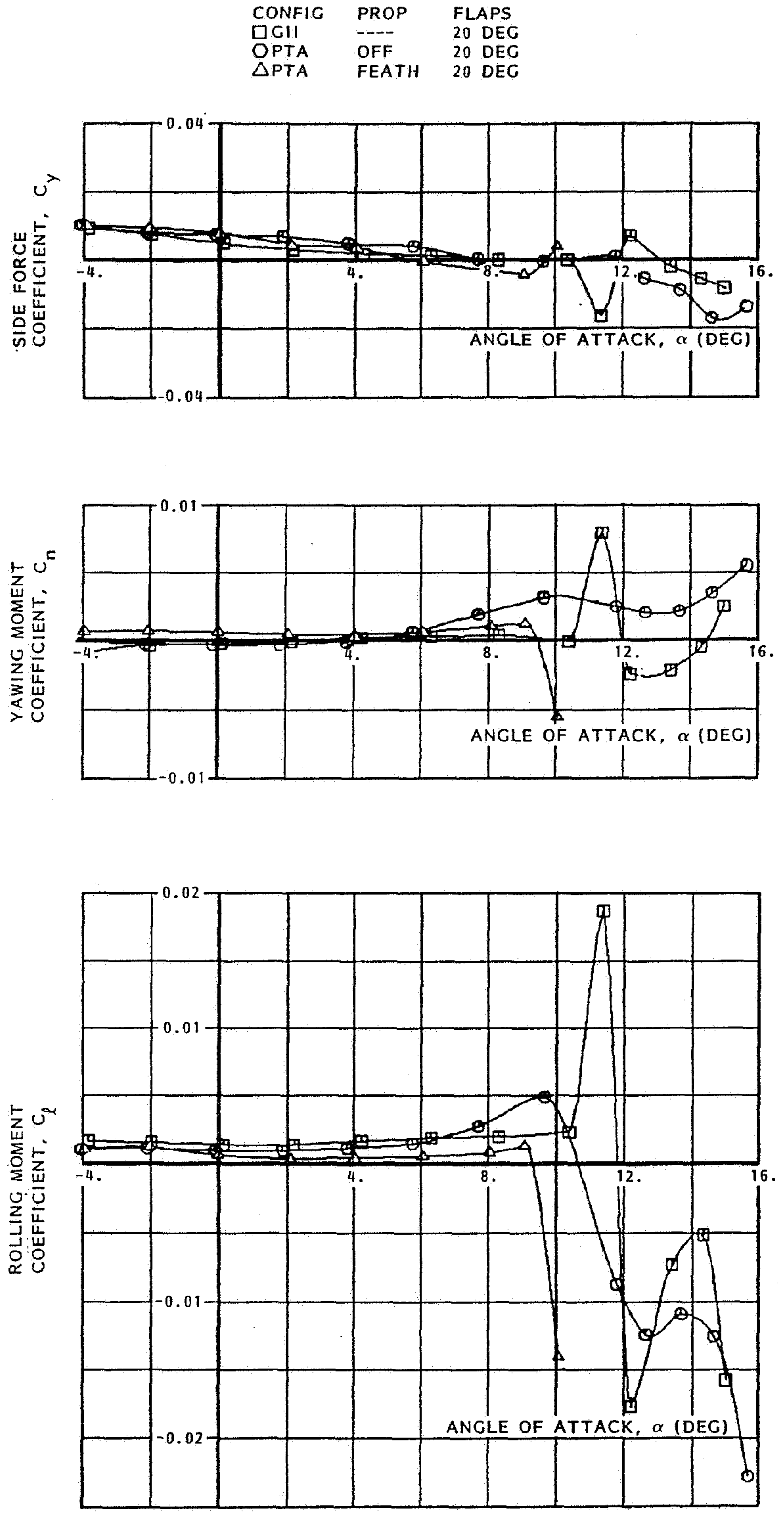

Figure 47. Effects of PTA Modifications on Side Force, Yawing Moment, and Rolling Moment - Flaps 20-Degrees

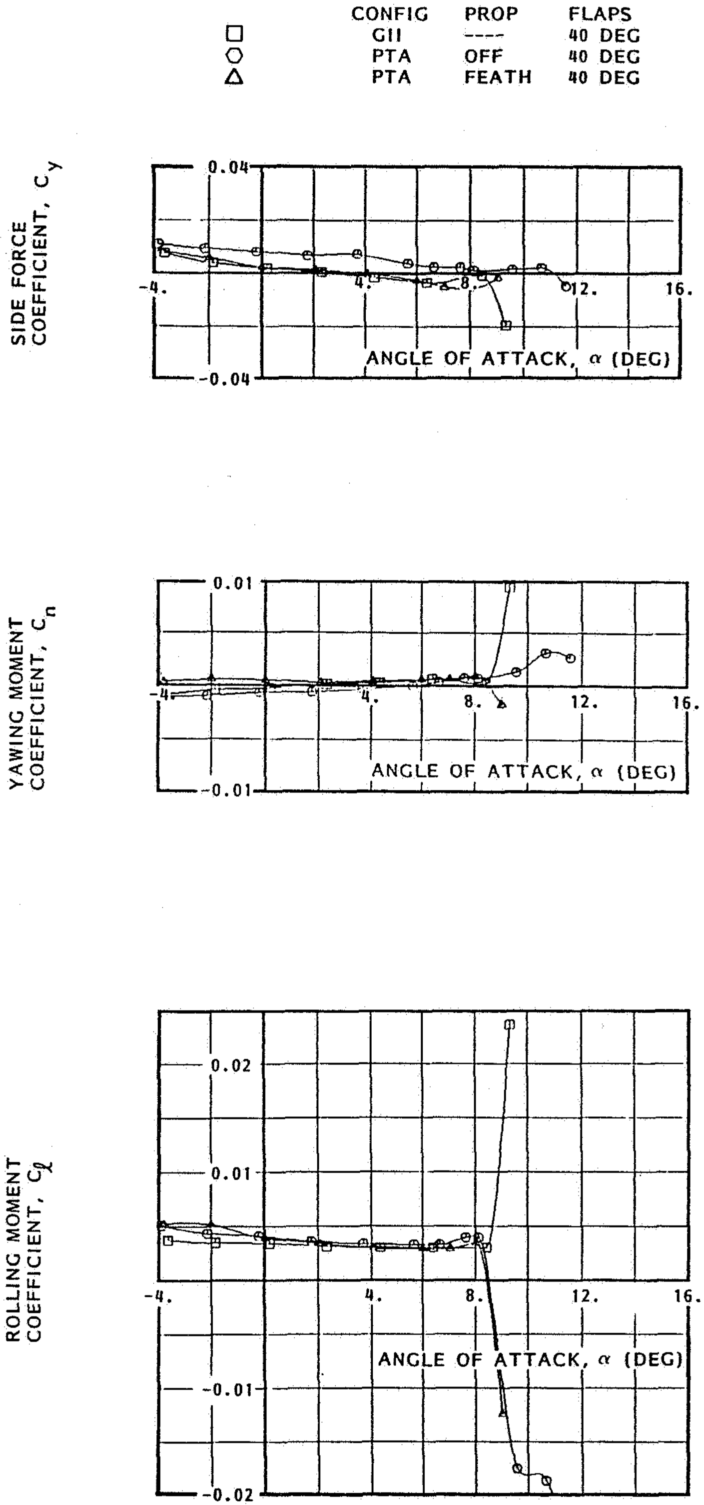

Figure 48. Effects of PTA Modifications on Side Force, Yawing Moment, and Rolling Moment - Flaps 40-Degrees

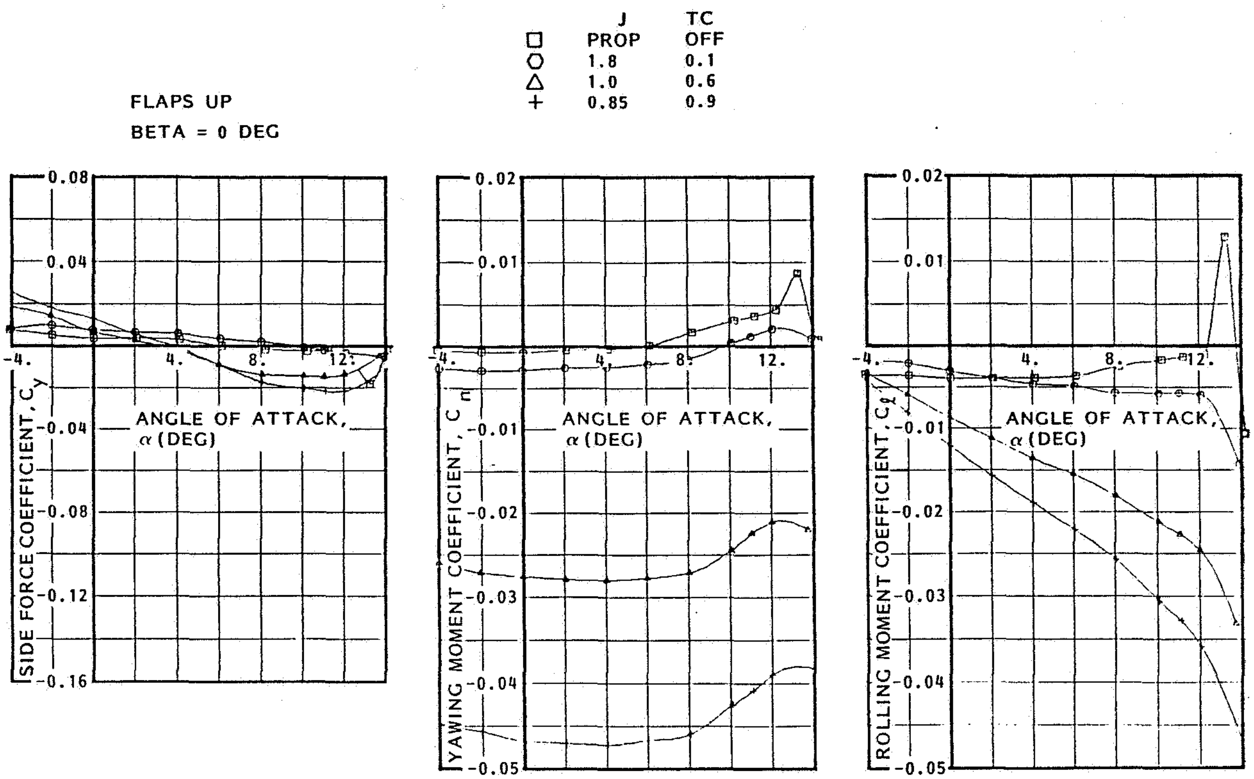

Figure 49. Effects of Power on Aerodynamic Characteristics in Pitch - Flaps Up

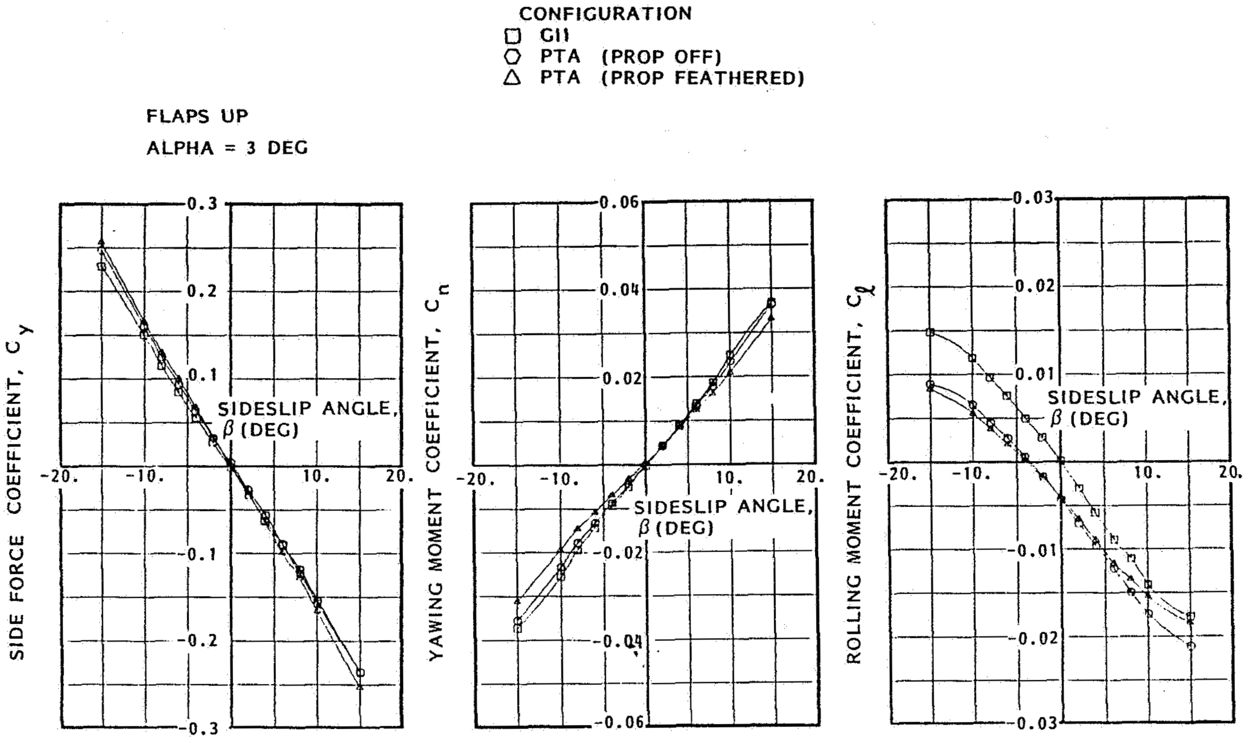

Figure 50. Effects of PTA Modifications on Sideslip Characteristics-Flaps Up

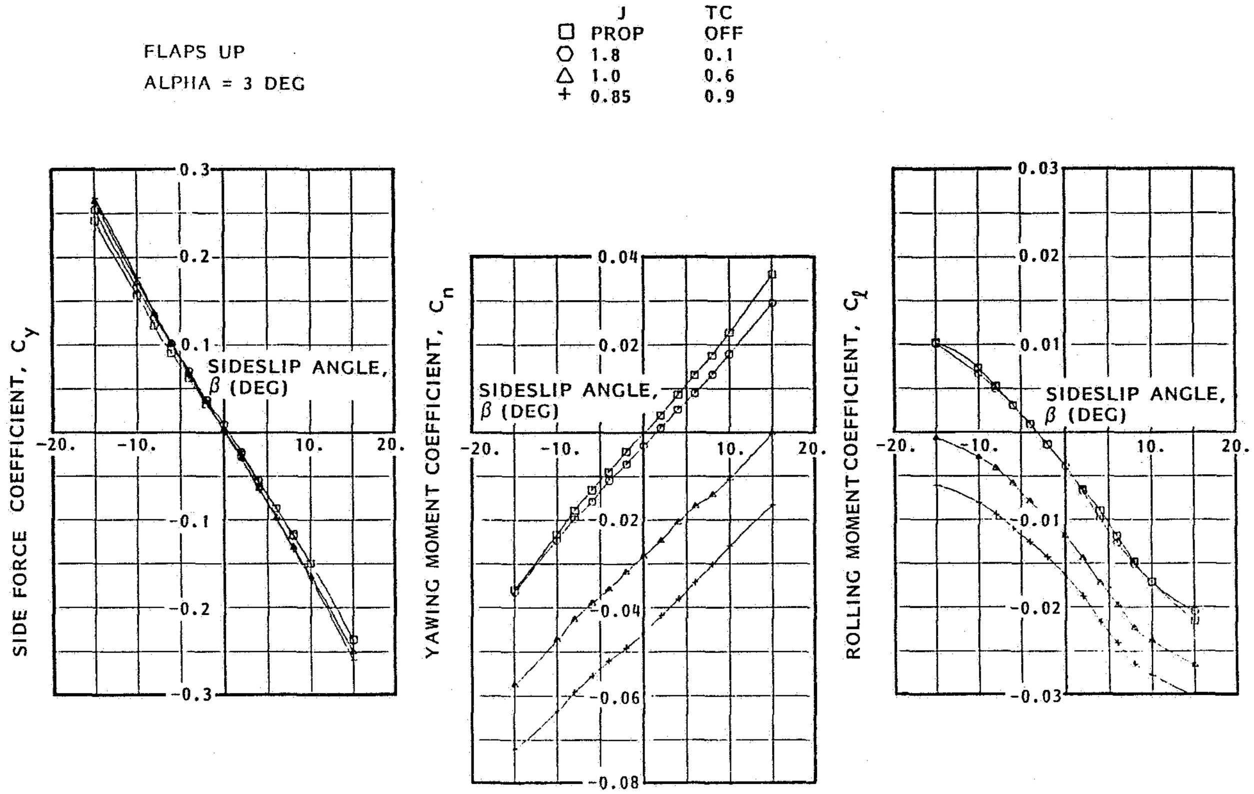

Figure 51. Effects of Propfan Power on Aerodynamic Characteristics in Sideslip - Flaps Up

Similar data are shown in Figures 52 and 53 for the takeoff and landing configurations, respectively. The same level of increase in sideforce variation and decrease in yawing moment and rolling moment with sideslip angle occurred relative to the GII as for the flaps-up configuration. The offset in rolling moment for the basic GII is again apparent.

No propfan powered data were obtained in the wind tunnel for the flaps-deflected cases because the PTA aircraft was not designed to operate under those conditions.

7.3.4 Control Effectiveness - Low Speed

Elevator effectiveness for the three flap configurations is shown in Figure 54. With the flaps up, there was slightly less pitching moment due to elevator deflection in the PTA configuration relative to the GII. Both show further losses at negative angles of attack. These differences are largely due to the variation of tail angle of attack with flap setting and show that at negative values (fuselage angle of attack less than 1.4 degrees) the effectiveness of full-up elevator deflection diminished but was not stalled. For 20 degrees of flap, the negative tail angle of attack range began at a fuselage angle of attack of 8 degrees and showed the typical decrease in effectiveness through zero. For flaps at 48 degrees, the tail angle of attack is always negative, and the secondary "plateau" has already been reached. At zero fuselage angle of attack, tail stall began with full up elevator, thus the sharp decrease in elevator effectiveness. Under these condition, the total tail lift is almost constant.

All these effects are highly Reynolds number dependent, and at full-scale conditions, it is anticipated that no loss of elevator effectiveness, either on the GII or the PTA, would actually occur. The trailing edge down elevator of 10 degrees shows little or no effect of angle of attack on PTA configuration.

Rudder effectiveness data are shown in Figures 55 through 57 for the GII and PTA models in the clean, takeoff, and landing configurations as a function of fuselage angle of attack. Very little difference in effectiveness occurred for any of the axes relative to the GII, but there does appear to be a slight increase due to propfan power, flaps up.

Spoiler effectiveness data are shown in Figure 58 as increments due to spoiler deflection about all axes for the GII and the PTA configurations. It should be noted that the single outboard spoiler panel is used for both GII and PTA data and is mounted on the right wing with the PTA nacelle. The lift decrement due to spoiler deflection is increased by the presence of the propfan nacelle. The nacelle increased the outer wing span loading, thus creating more lift for the spoiler to reduce. The addition of a feathered propfan reduced the lift decrement due to the spoiler back to the same level as the GII configuration for angles of attack up to 6 degrees and then shows further degradation at higher angles as the lift due to the nacelle increased. This occurred because the feathered propeller influenced the outer wing and reduced the lift gains from the nacelle. The pitching moment increment due to the spoilers is in the aircraft nose-up direction and is consistent with the lift reduction behind the moment center. Sideforce changes are negligible, and a small yawing moment increment due to spoiler drag is apparent. The roll due to

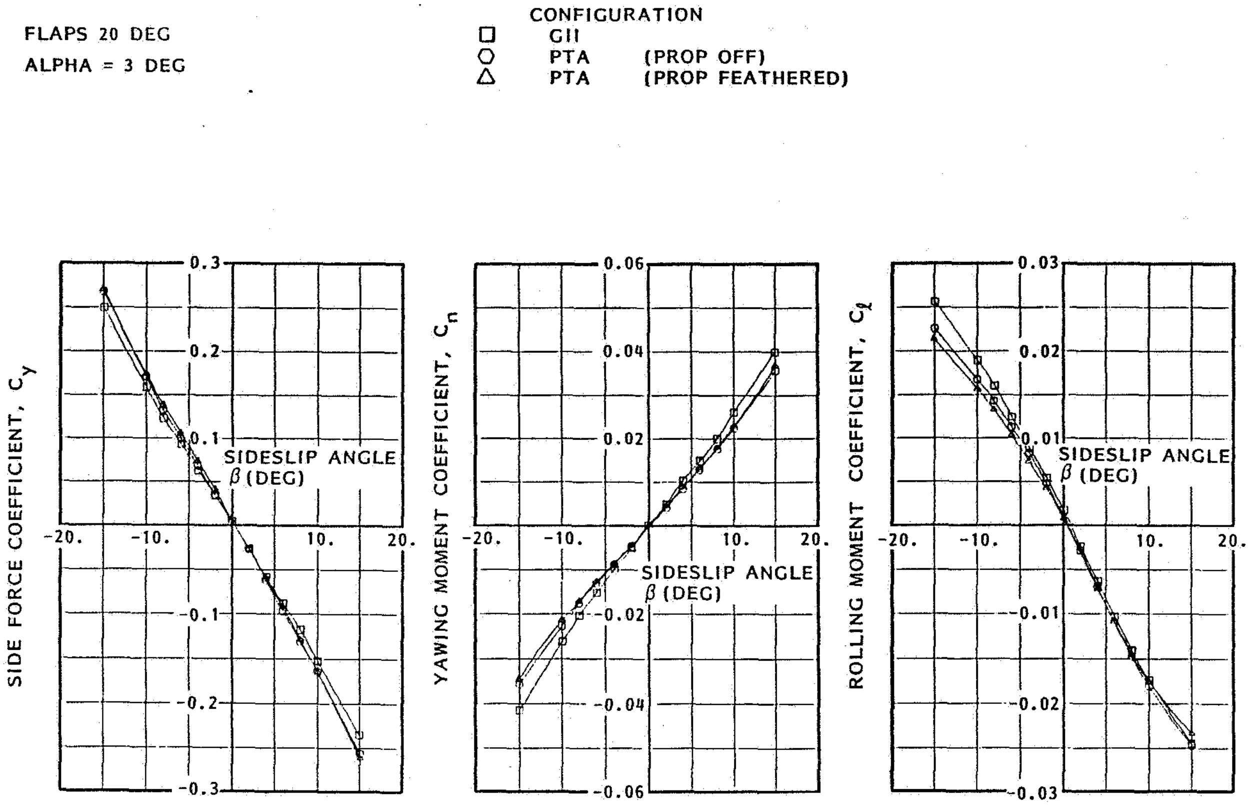

Figure 52. Effects of PTA Modifications on Sideslip Characteristics-Flaps 20-Degrees

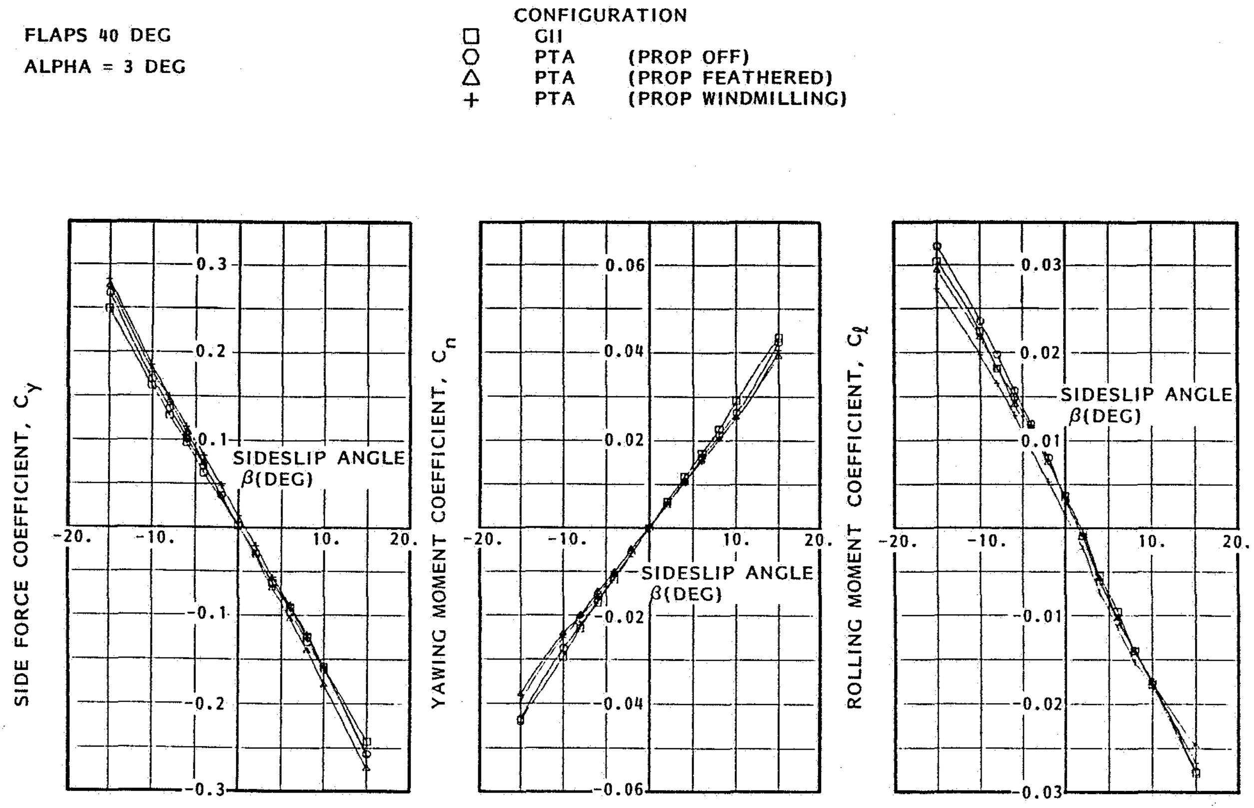

Figure 53. Effects of PTA Modifications on Sideslip Characteristics-Flaps 40-Degrees

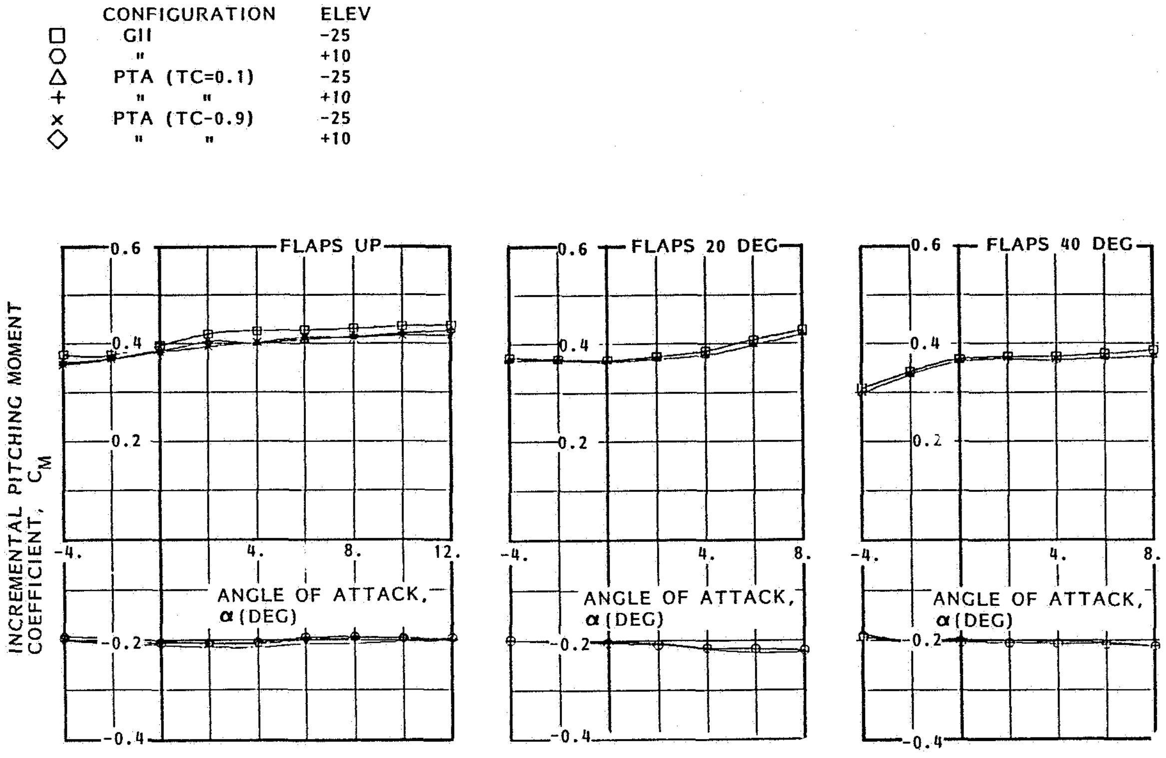

Figure 54. Elevator Effectiveness

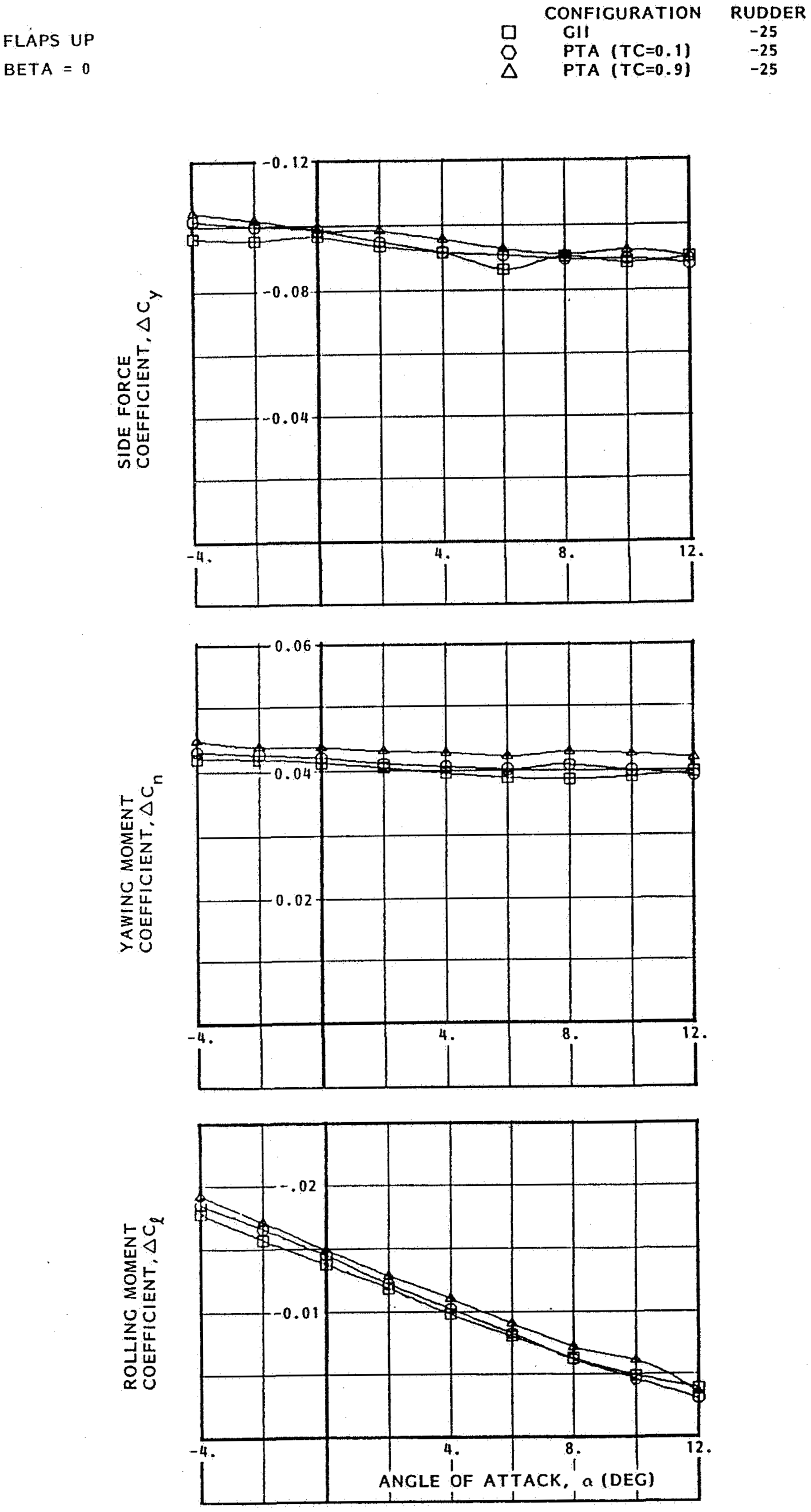

Figure 55. Rudder Effectiveness in Pitch - Flaps Up

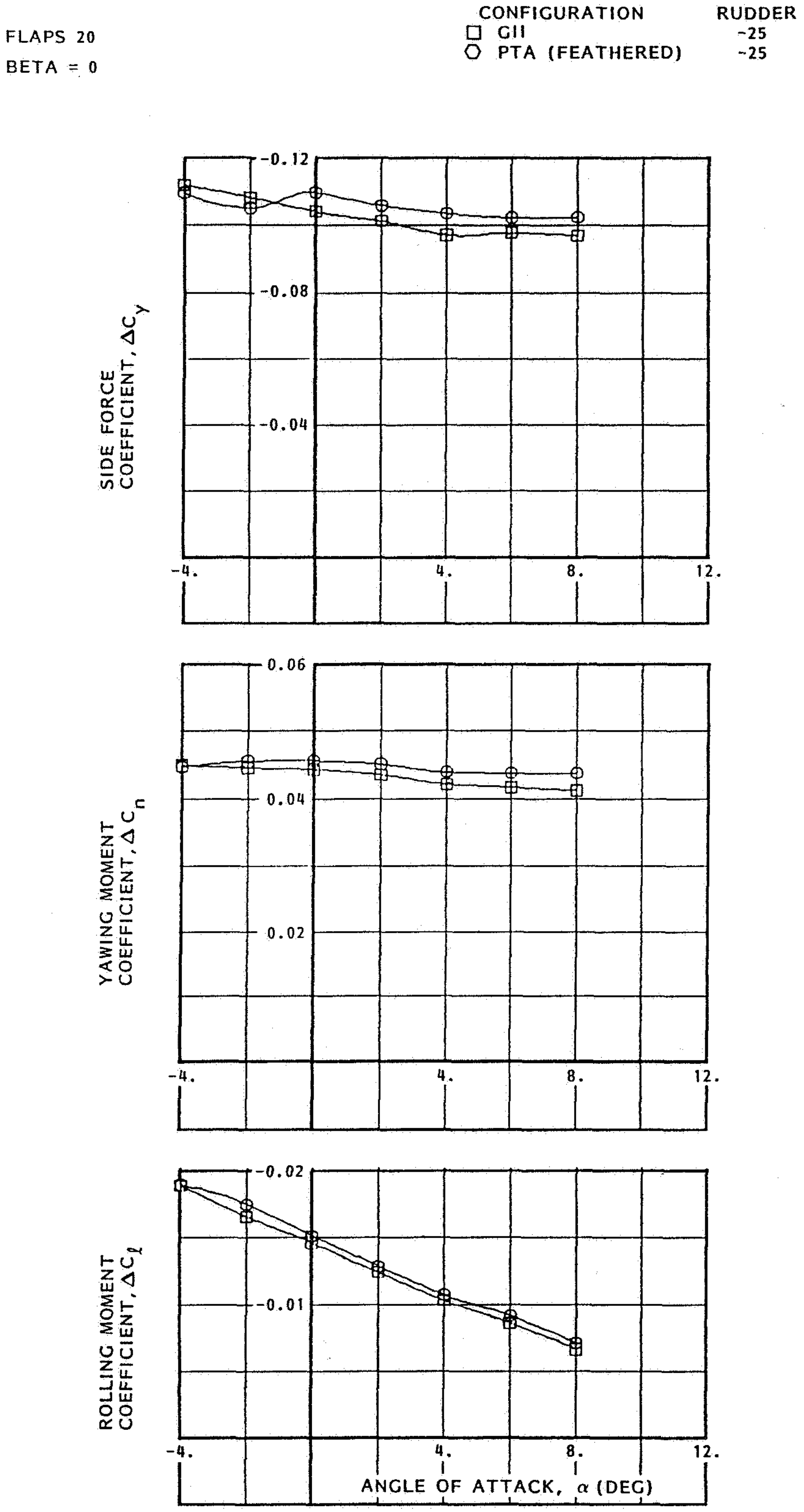

Figure 56. Rudder Effectiveness in Pitch - Flaps 20-Degrees

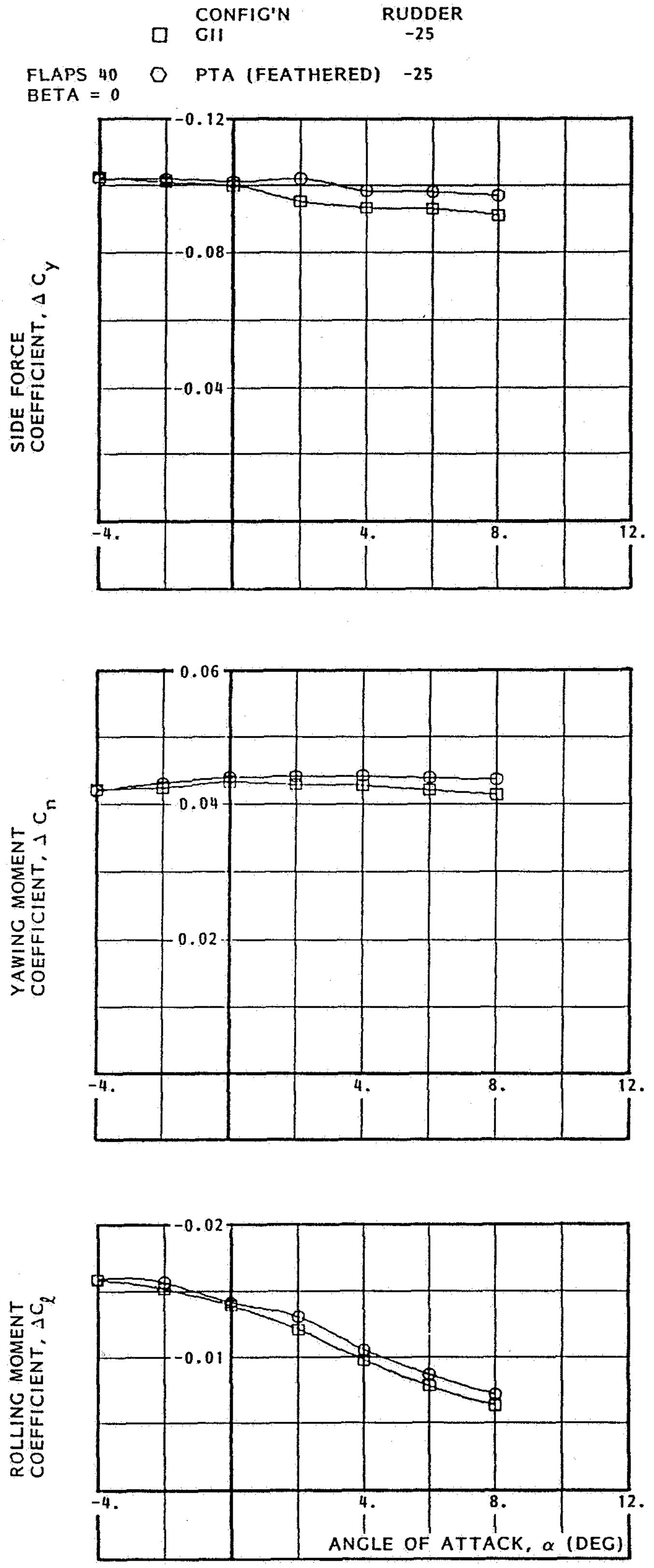

Figure 57. Rudder Effectiveness in Pitch - Flaps 40-Degrees

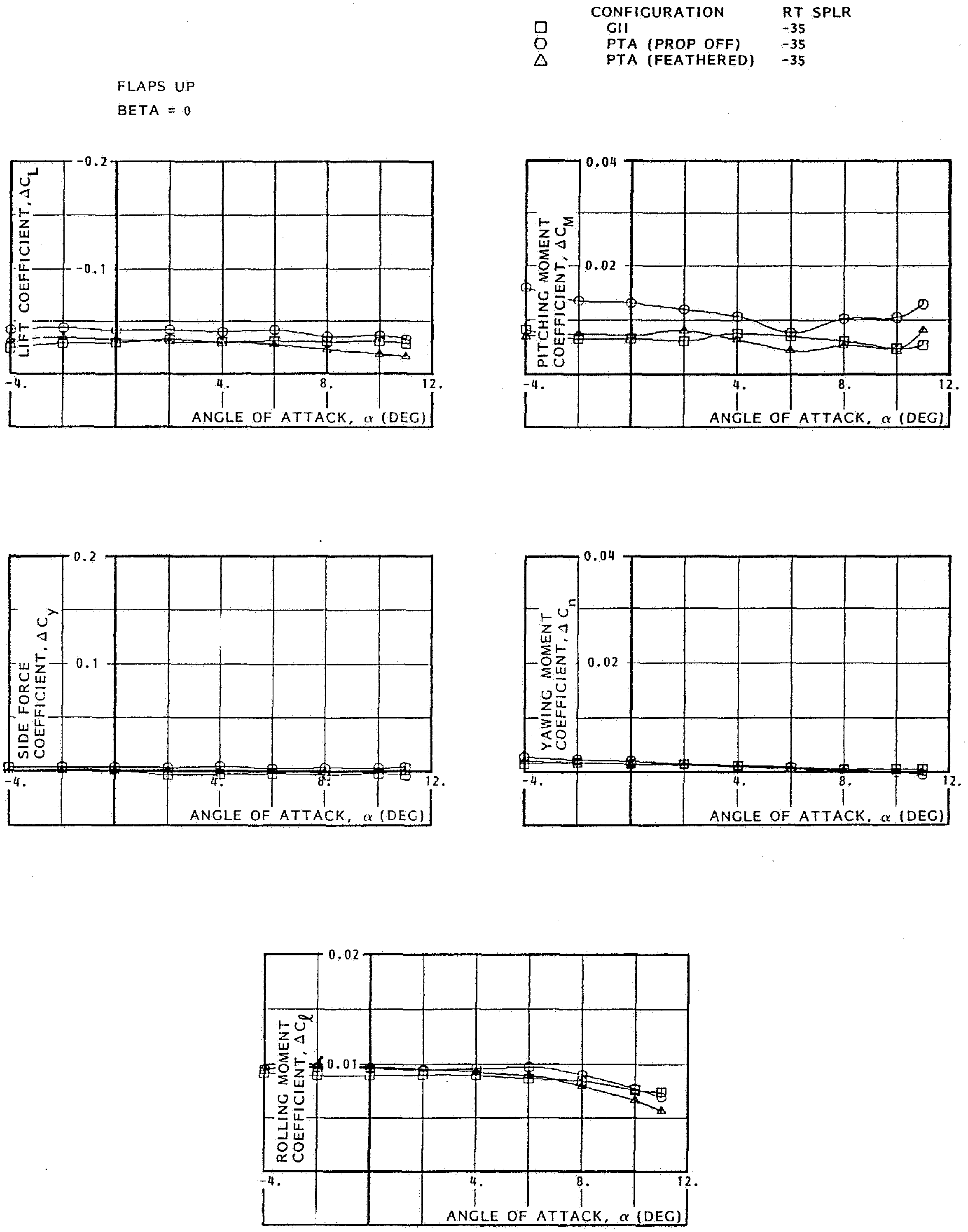

Figure 58. Spoiler Effectiveness in Pitch - Flaps Up

spoiler deflection had the same shape as the lift reduction and remained almost constant to high angles of attack. Full-scale, these values would hold to a higher angle of attack as the stall level increased. Because some of the spoiler panels were deactivated for the PTA installation, it was estimated that spoiler effectiveness would diminish to about 55 percent of the published GII values. These data indicate, however, that PTA spoiler effectiveness is about 62 percent of the GII performance.

The effect of propfan power on the roll effectiveness of the spoiler and aileron (one side only) is shown in Figure 59. The aileron contribution was not affected by power, hence the differences are entirely spoiler effects. The local increase in lift due to the propfan slipstream contributed to the increased spoiler effectiveness and the delay in the "drop-off" at high angle of attack. The effect of sideslip on spoiler roll power is also shown in this figure. At negative sideslip angles (right wing trailing), the effectiveness of the spoiler was reduced for both GII and PTA configurations and was largely due to the loss of wing lift on the trailing wing. The propfan slipstream reduced the sideslip loss and hence improved the spoiler effectiveness such that essentially no change occurred with sideslip. Operationally, this effect is of little consequence since, in general, the spoiler on the leading wing would be deflected for sideslip control.

Spoiler effectiveness with takeoff flap is shown in Figure 60. The lift loss due to spoiler increased because of the increased wing lift from the flaps, and consequently, the roll effectiveness of the spoiler increased. The full-span GII spoiler produced a rolling moment coefficient of 0.0344 compared to the PTA level (props off) of 0.0194. Thus, the PTA spoiler effectiveness was 56 percent of the GII level.

Similar data for the landing flap configuration are shown in Figure 61. Spoiler rolling moment effectiveness was further increased relative to the flaps-up level and is 60 percent of the published GII level with landing flap.

The complete roll control consists of left and right aileron deflection of ±10 degrees and spoiler deflection on "aileron up" wing. The aileron effectiveness was unchanged by the PTA configuration and does not vary with flap deflection. For low-speed flight, the total contribution from the aileron to the rolling moment coefficient was 0.020. The resultant spoiler/aileron effectiveness of the PTA configuration relative to the published GII level becomes 86 percent, 76 percent, and 71 percent for the clean, takeoff, and landing flap configurations, respectively. Operationally, these values have to be adjusted for flexibility effects, and since the PTA wings are considerably stiffer than the GII wings, the percentage loss of effectiveness due to the reduced span spoiler should be lowered.

7.3.5 Effect of Nacelle Incidence - Low Speed

The effect of nacelle incidence changes on lift and pitching moment is shown in Figures 62 and 63. Virtually no change in lift occurred over the operational range of angle of attack. Small changes in maximum lift coefficient are apparent. These are probably due to differences in wing leading edge pressure changes in the vicinity of the nacelle that would probably not exist at full-scale Reynolds number. A small positive change

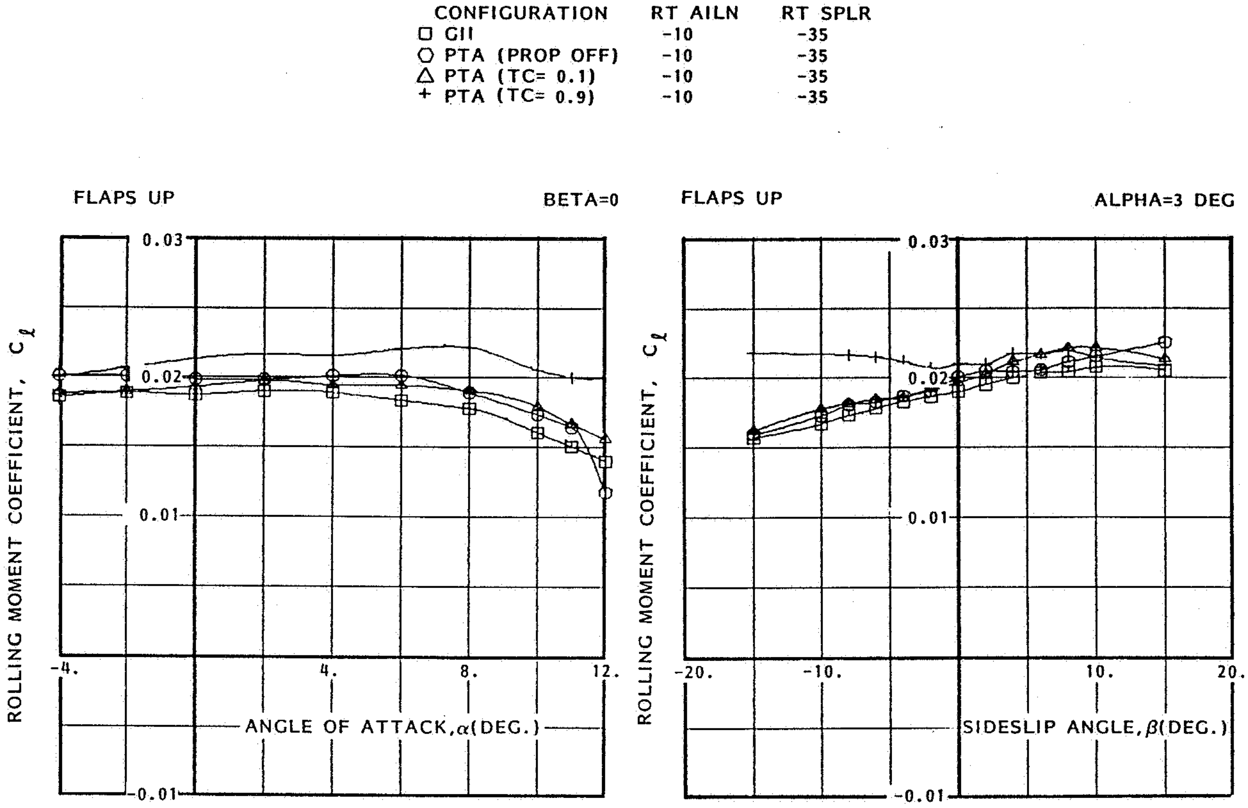

Figure 59. Rolling Moment From Aileron and Spoiler Deflections-Flaps Up

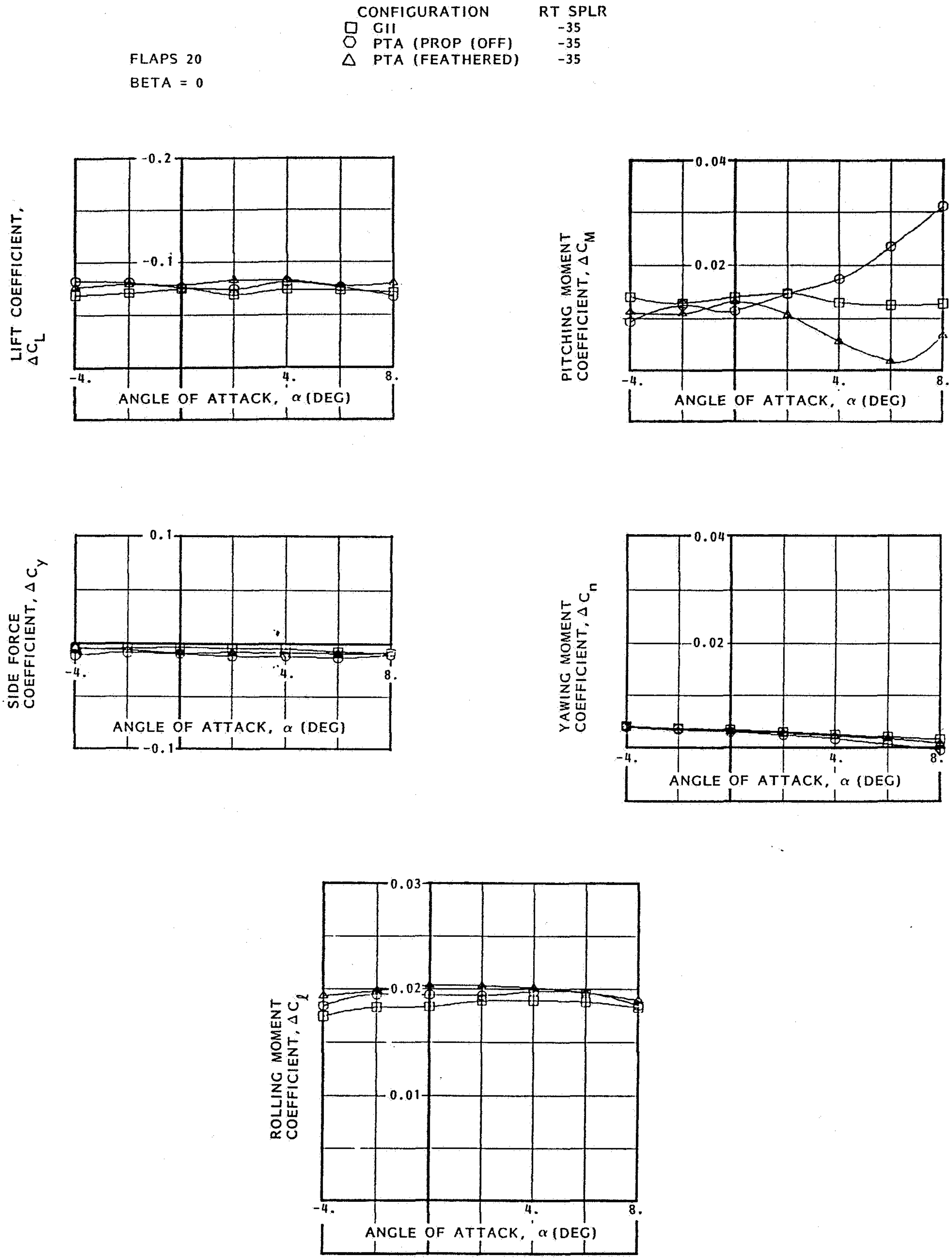

Figure 60. Spoiler Effectiveness in Pitch - Flaps 20-Degrees

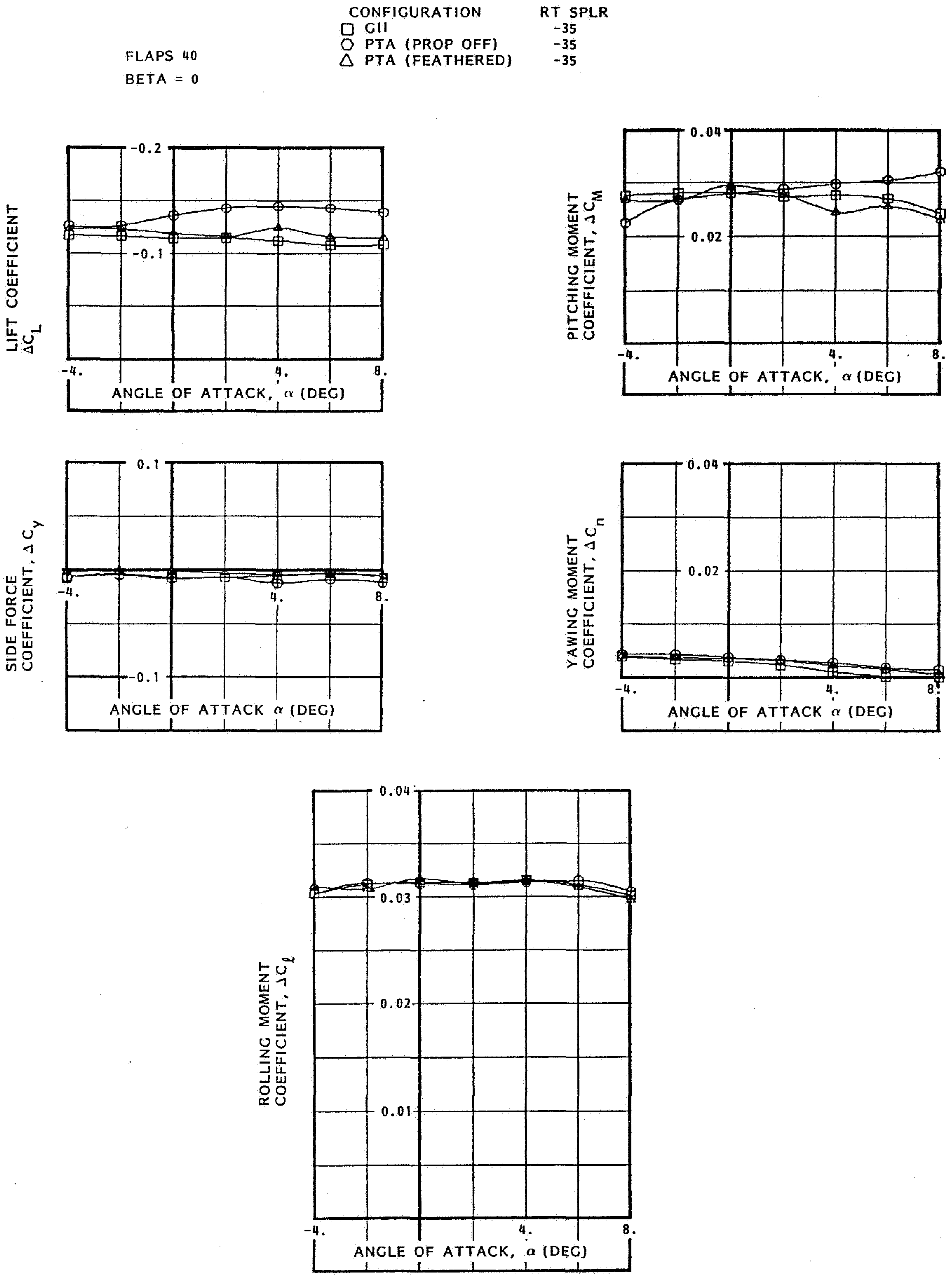

Figure 61. Spoiler Effectiveness in Pitch - Flaps 40-Degrees

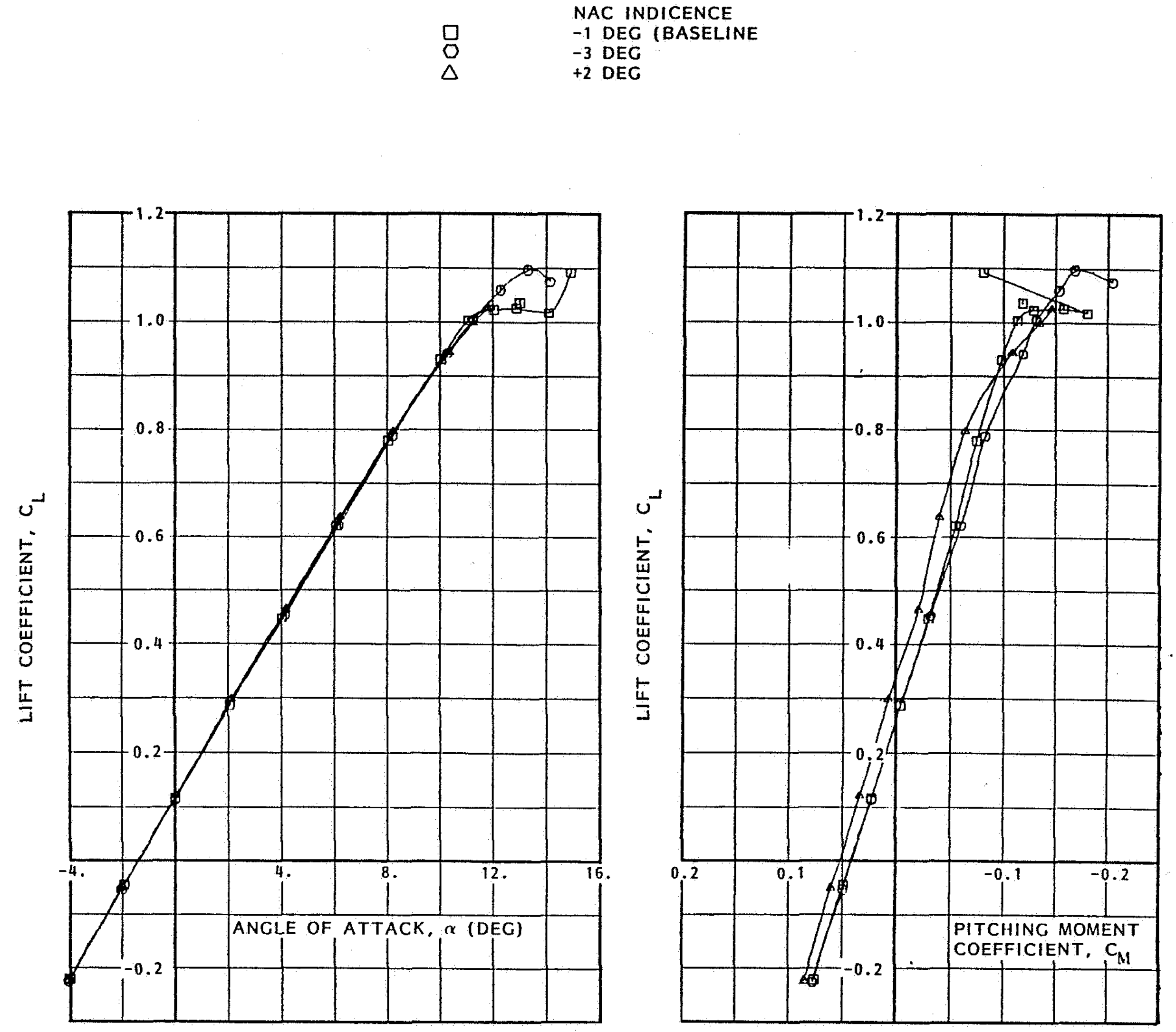

Figure 62. Effects of Nacelle Incidence on Lift and Pitching Moment - Flaps Up

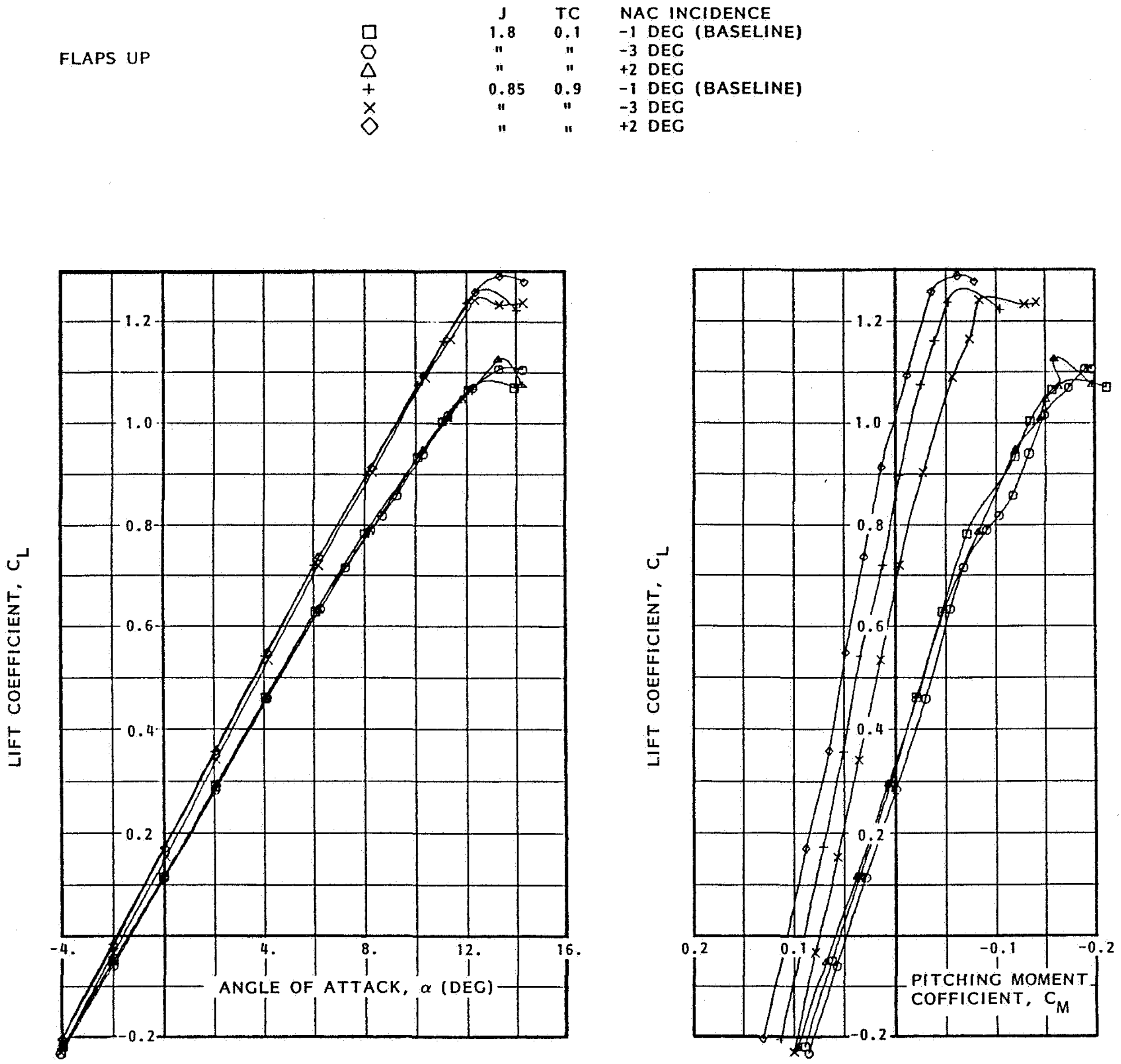

Figure 63. Effects of Nacelle Incidence on Lift and Pitching Moment - Flaps Up, Propfan Power On

in pitching moment occurs with +2 degrees of incidence relative to -1 degree that is a function of a nacelle lift change. There is also a negative pitching moment change with -3 degrees that has been masked by a similar positive change at the horizontal tail. In the presence of propfan power, these pitching moment changes are stronger and more uniform. The tail changes are small and random and insignificant. The trim changes associated with nacelle incidence are small but uniform.

The effect of the nacelle incidence changes on lateral-directional data in sideslip is very small and of no consequence. The change in sideforce with nacelle incidence is the only measurable parameter with high propfan power and should cause small changes in bank angle for trim that would be difficult to detect.

7.3.6 Lift and Pitch - High Speed

The variation of lift and pitching moment with Mach number for the GII and various PTA configurations is shown in Figures 64 through 67 for Mach numbers from 0.4 to 0.85. A lift increment due to the PTA nacelle, of the same magnitude as the low-speed data, can be seen in Figure 64 at lower angles of attack. As angle of attack increased, this lift increment changed to a loss as a result of inner wing leading edge loading shifts. This load shift also produced a stable change in pitching moment at high angles of attack that are above the angles for operational needs. For lift coefficients between 0.2 and 0.4, the pitching moment differences between the PTA and GII configurations became smaller as Mach number is increased to 0.85. Hence only small differences in trim requirements and lift at constant angle of attack are to be expected.

Composite pictures showing compressibility effects on lift data for the GII and PTA configurations are shown in Figure 68. These plots were constructed using the low-speed and high-speed test results. For these plots, the low-speed data, which were obtained at a Reynolds number of 1.65 million, have been corrected to the Reynolds number of the high-speed data (3.35 million based on wing chord). The lift correction is primarily due to wing lift-curve-slope changes.

It can be seen in Figure 68 that the PTA maximum lift was slightly reduced, and the compressibility effect peaked at a slightly lower Mach number than for the GII. It is these two parameters that define the buffet onset curve for the operational speed range. Superimposed on the GII lift data is the buffet onset curve derived from flight experience. At low Mach numbers, this curve is primarily an indication of the beginning of stall separation; at high Mach numbers, it is a result of shock shifts and boundary layer thickness adjustments causing wing load changes that result in buffeting. This latter usually becomes noticeable close to the lift peak at a particular Mach number and angle of attack combination as indicated by the 2- and 3-degree points. At 4 and 5 degrees the test data indicate a buffet onset prior to the peak lift for the GII. The PTA compressibility peak occurred a little earlier and would therefore indicate an earlier buffet onset.

Figures 69 and 70 summarize lift and pitching moment data from low- and high-speed tests. The effects of compressibility on the pitching moment at constant lift, as shown in Figure 69, indicate a typical Mach

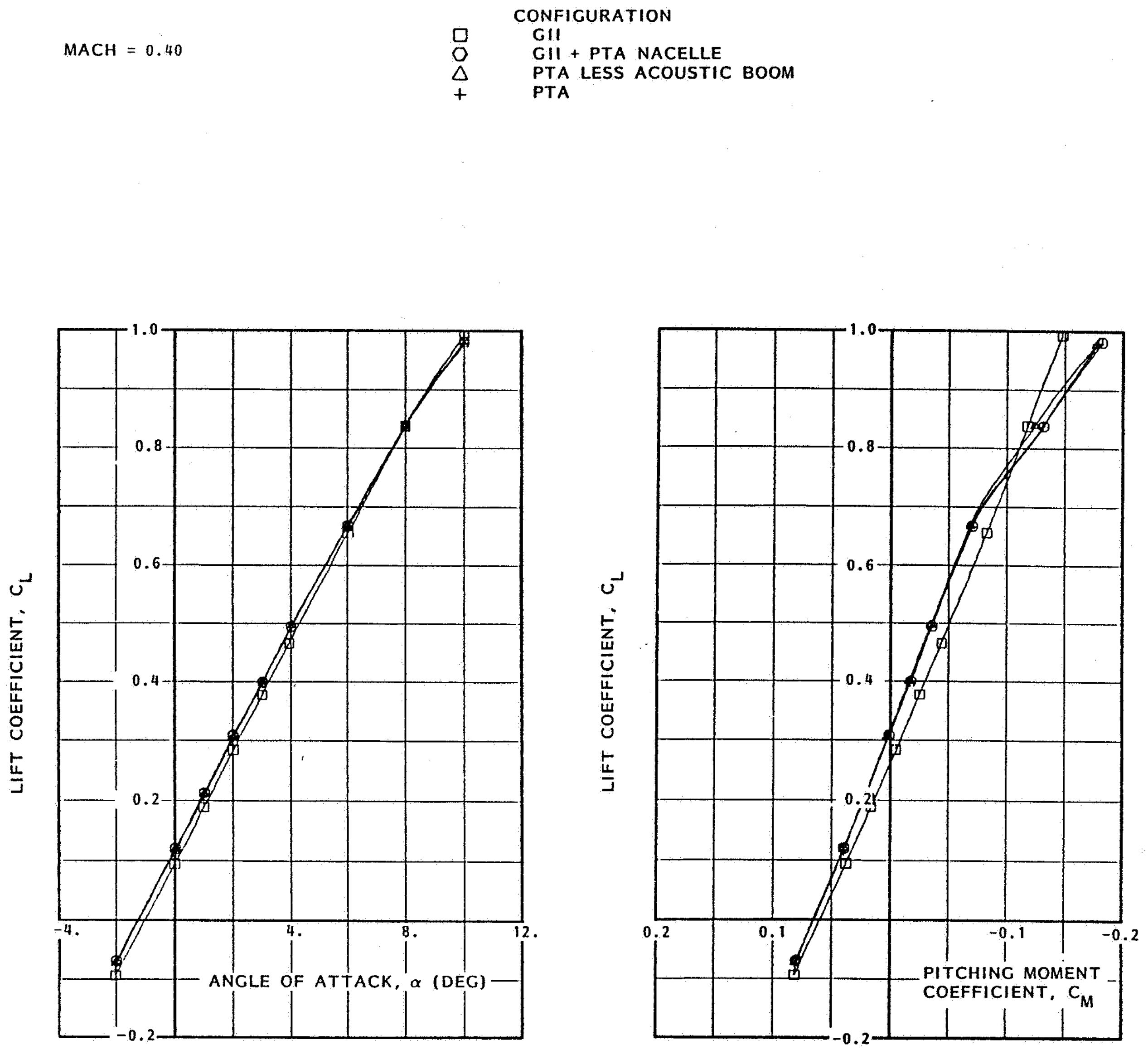

Figure 64. PTA Configuration Buildup - Mach 0.4

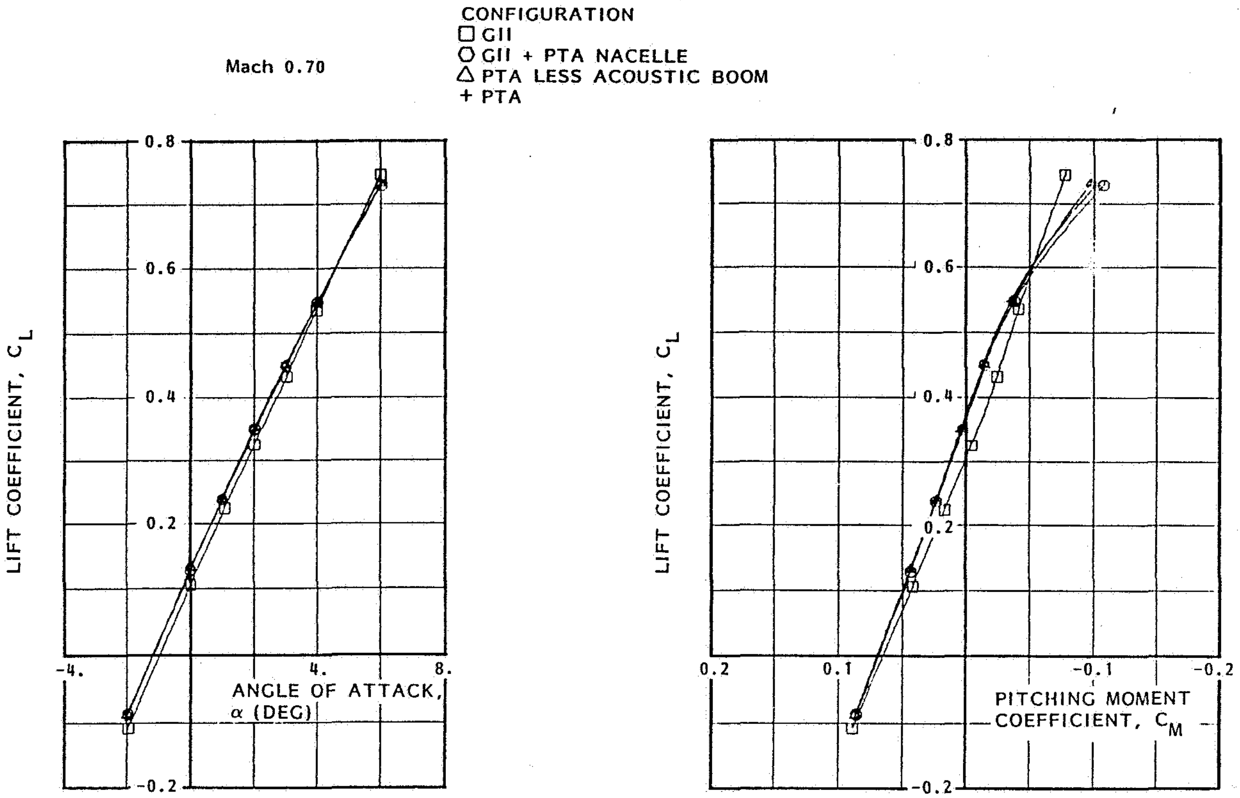

Figure 65. PTA Configuration Buildup - Mach 0.7

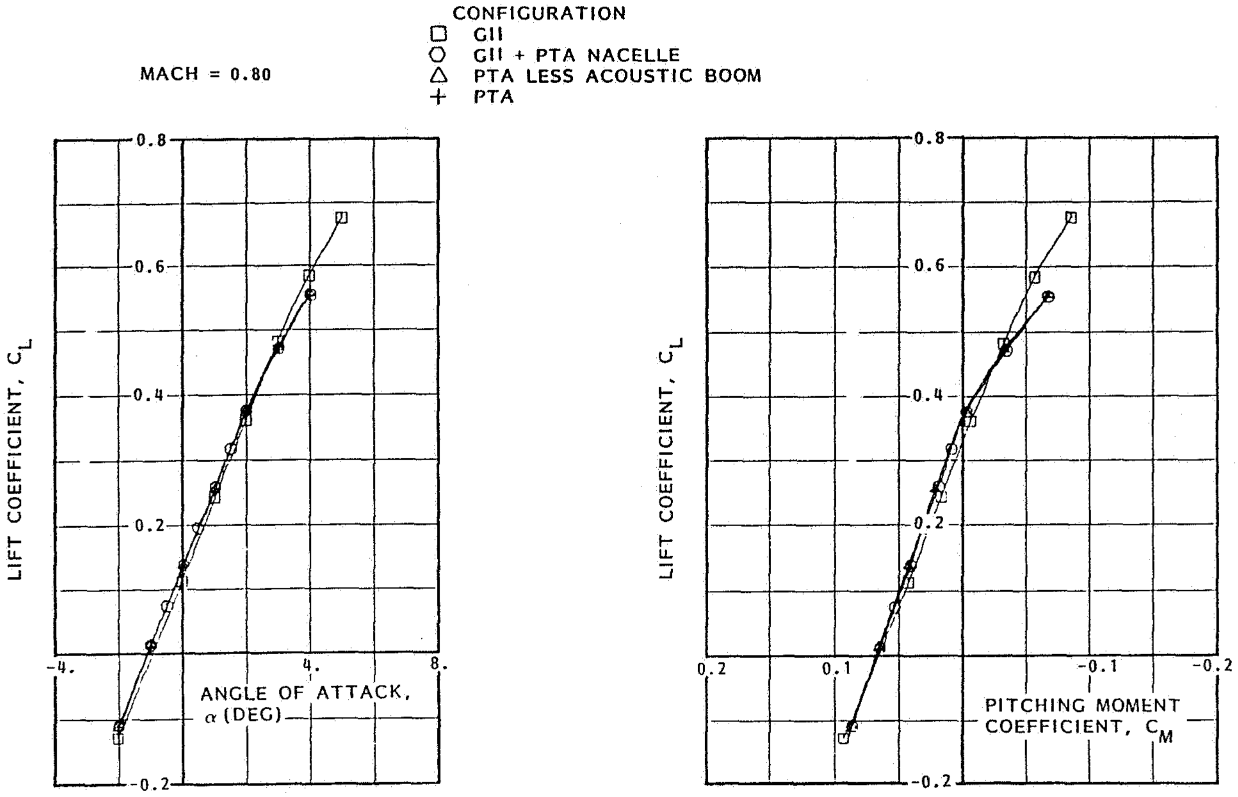

Figure 66. PTA Configuration Buildup - Mach 0.8

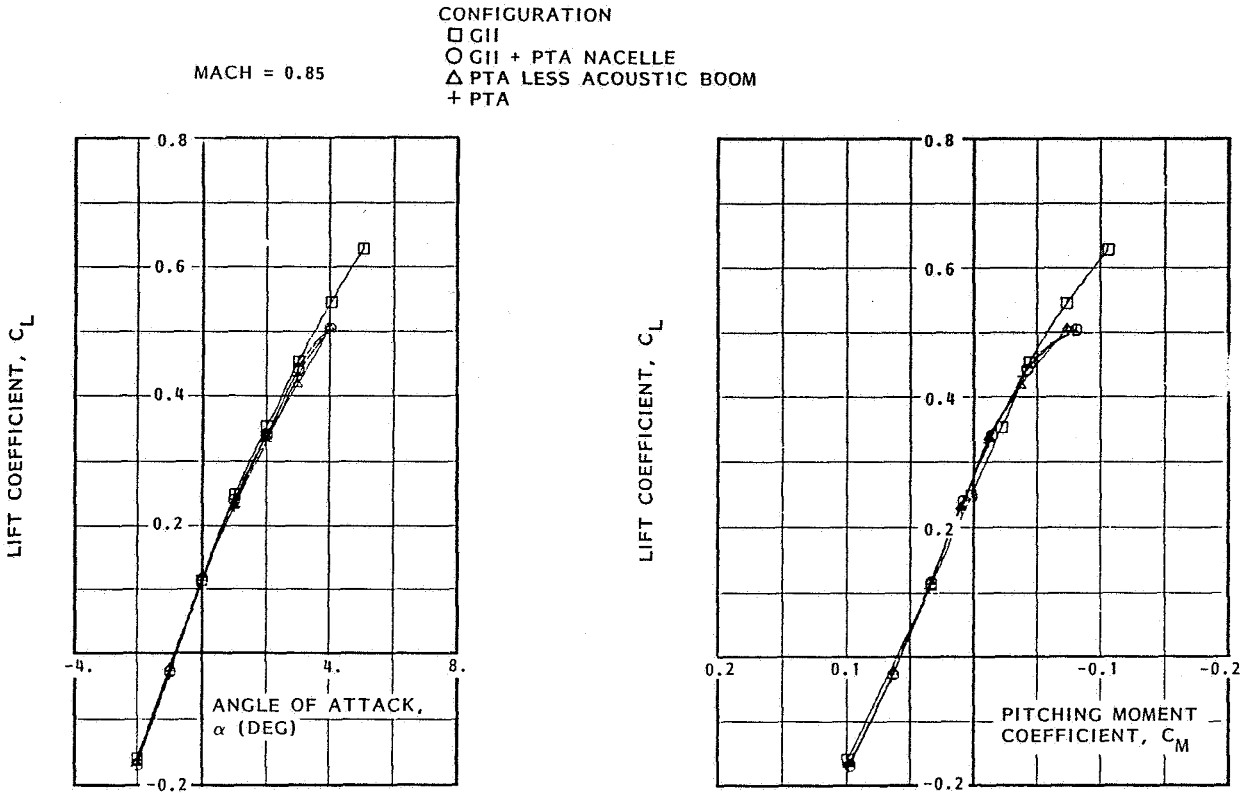

Figure 67. PTA Configuration Buildup - Mach 0.85

C-2

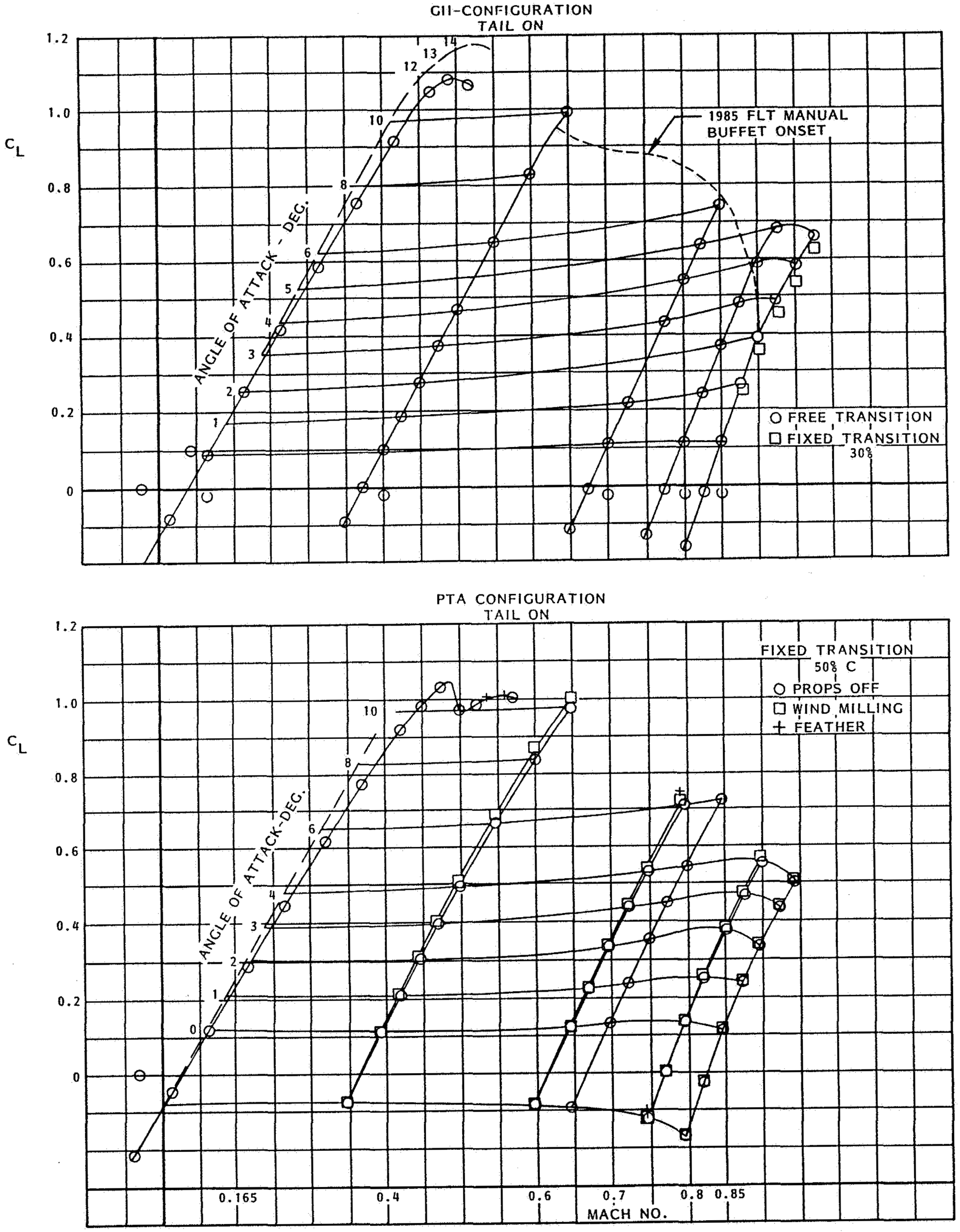

Figure 68. Mach Number Effects on Lift Characteristics

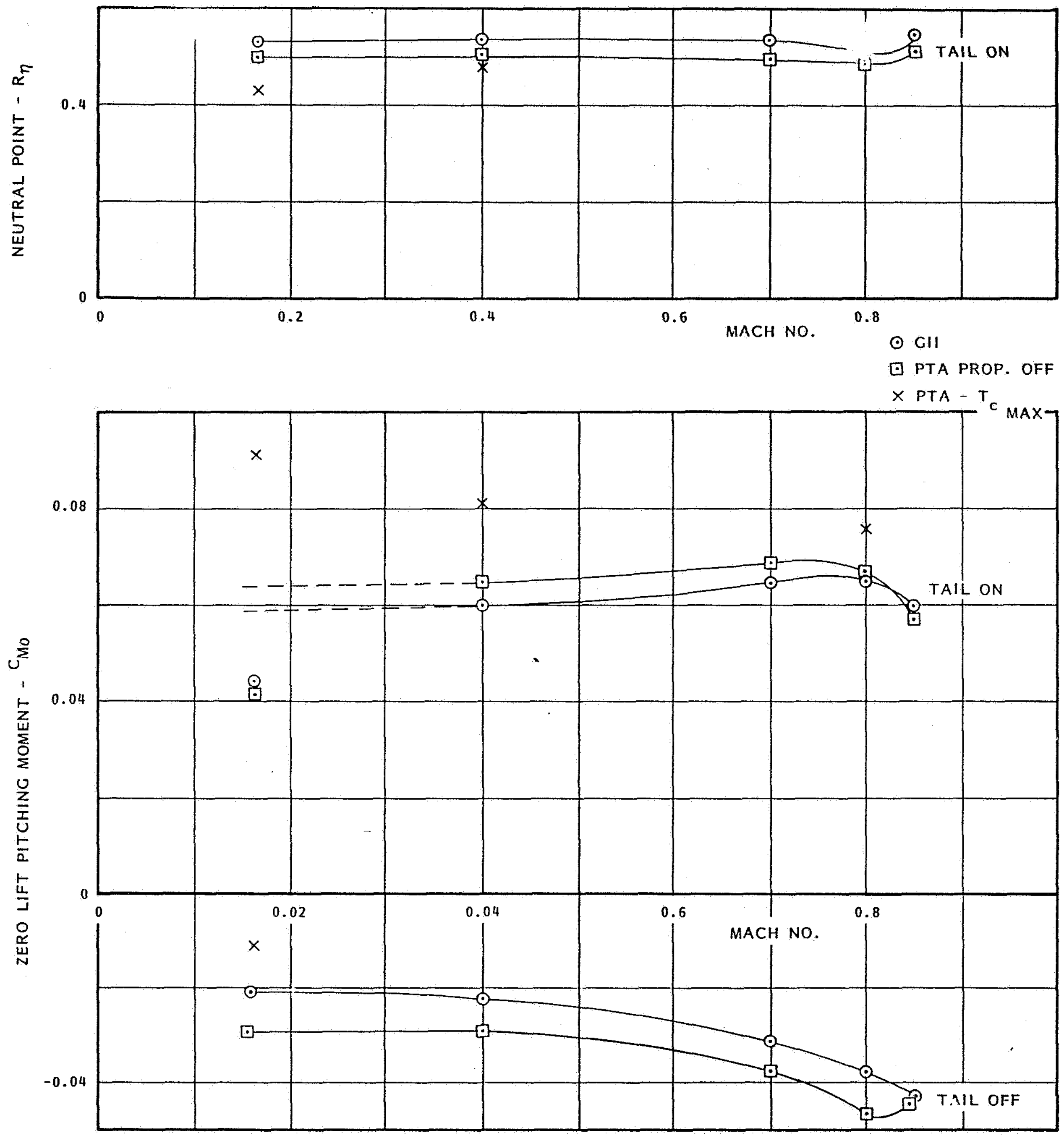

Figure 69. Comparison of Lift Data From Low- and High-Speed Test

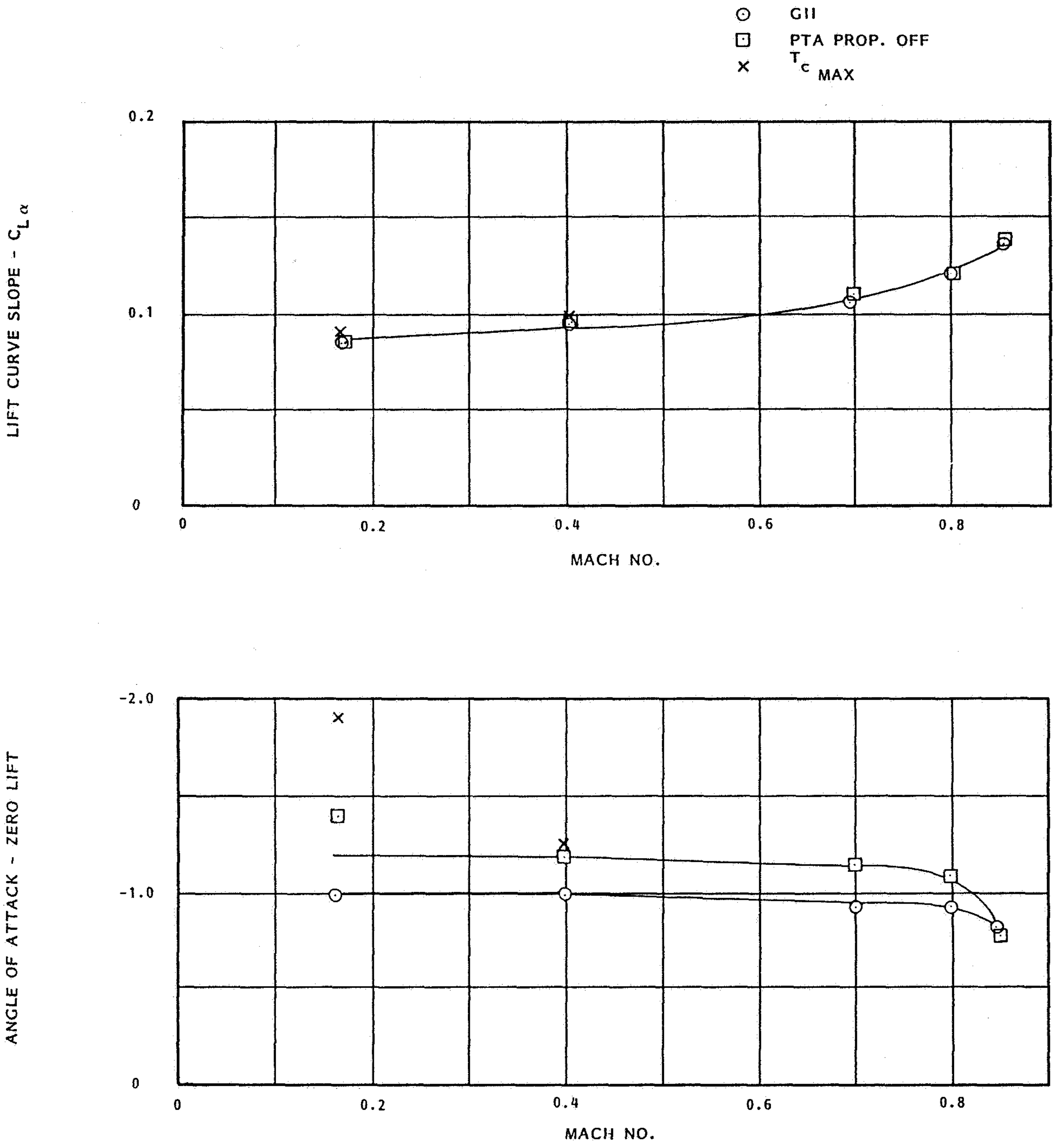

Figure 70. Comparison of Pitch Data From Low- and High-Speed Test

"tuck" above a Mach number of 0.8 for both the GII and the PTA configurations. This nose down tendency is a little more pronounced for the PTA configuration. The Mach trim compensator in the GII control system should be adequate for the PTA as well.

The lift change due to the PTA installation (Figure 70) results in a change in angle of attack for zero lift with only minor changes in lift curve slope. The lift increase due to power at low speeds results in changes in both. The decrease in angle of attack for zero lift results in an increase in pitching moment at zero lift contributed by the tail as can be seen in Figure 69 at M = 0.4. At the low-speed test point, the apparent lower tail input to pitching moment at zero lift is due to the lower Reynolds number at the tail as previously discussed. The forward movement of the neutral point due to the PTA configuration is seen to be uniform over the Mach range. The effect of power is most pronounced at low speeds (high Tc).

7.3.7 Lateral-Directional Effects - High Speed

Lateral-directional data are shown in Figures 71 through 74 in terms of side force, yawing moment, and rolling moment coefficients at ±5 degrees of sideslip as a function of angle of attack. No direct sideslip data at constant angle of attack were obtained in the high-speed test due to tunnel support constraints. The offsets at zero sideslip are also shown. The side force and rolling moment effects for the GII are a result of the aerodynamic loads on the non-metric cover at the model-to-sting interface. While it is impossible to fully extract this increment from the data, since the cover loads vary as a function of the configuration, it is felt that the incremental effect of the PTA will be representative.

From Figure 71, at Mach 0.4, the incremental effect of sideslip on side force is seen to increase, relative to the GII, when the nacelle is leading and decrease, relatively, when the nacelle is trailing. Yawing moment due to sideslip shows little variation with angle of attack and only a slight reduction relative to the GII. Roll due to sideslip is slightly reduced by the PTA configuration but has the same rate of increase with angle of attack as the GII.

Similar effects are seen in Figure 72 at a Mach number of 0.7 and Figure 73 at a Mach number of 0.8. At a Mach number of 0.85, Figure 74, the reduction in roll due to sideslip at high angles of attack is stronger for the PTA than for the GII and may be noticeable to the pilot if he attempts to pick up a wing with controlled sideslip. It may also be noted that the offset in roll at zero sideslip is reduced to zero at small angles of attack and becomes positive at higher angles. This has the effect of making the offset in weight due to the nacelle appear heavier at high Mach numbers.

A summary of the sideslip derivatives and the offsets at zero sideslip are shown as functions of Mach number in Figures 75 and 76. It can be seen that there is very little difference in the derivatives relative to the GII of significance to aircraft handling qualities for testbed operations other than the reduction in roll due to sideslip. This reduction tends to increase the dutch roll stability and increase the spiral instability. This effect is of little consequence especially with a working yaw damper.

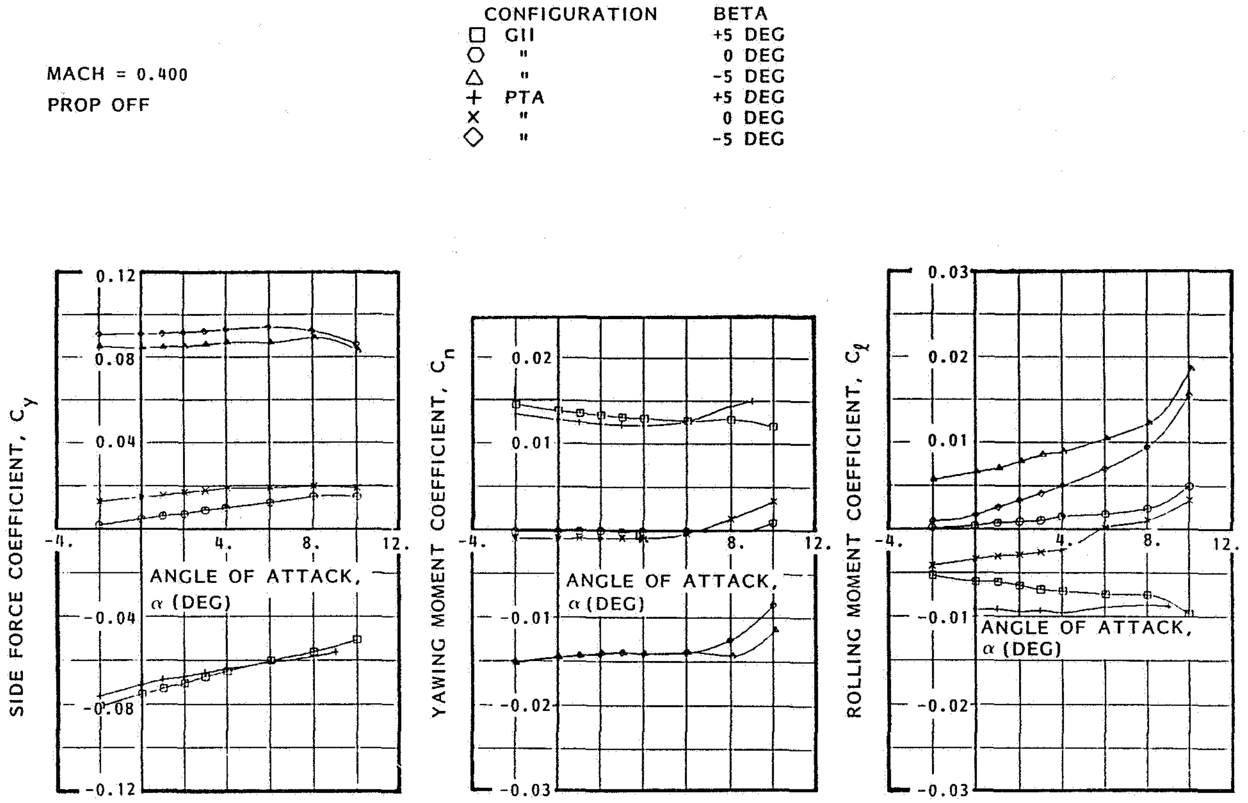

Figure 71. Comparison of GII and PTA in Sideslip - Mach 0.4

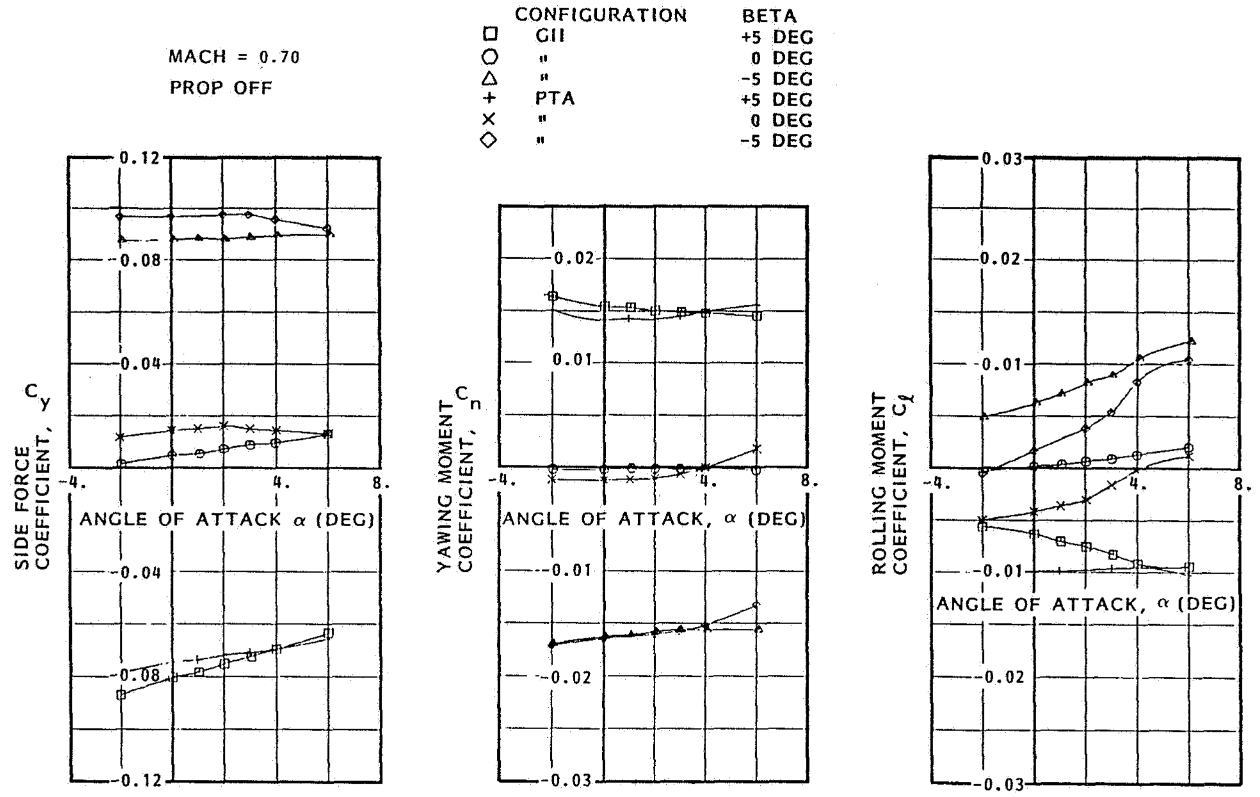

Figure 72. Comparison of GII and PTA in Sideslip - Mach 0.7

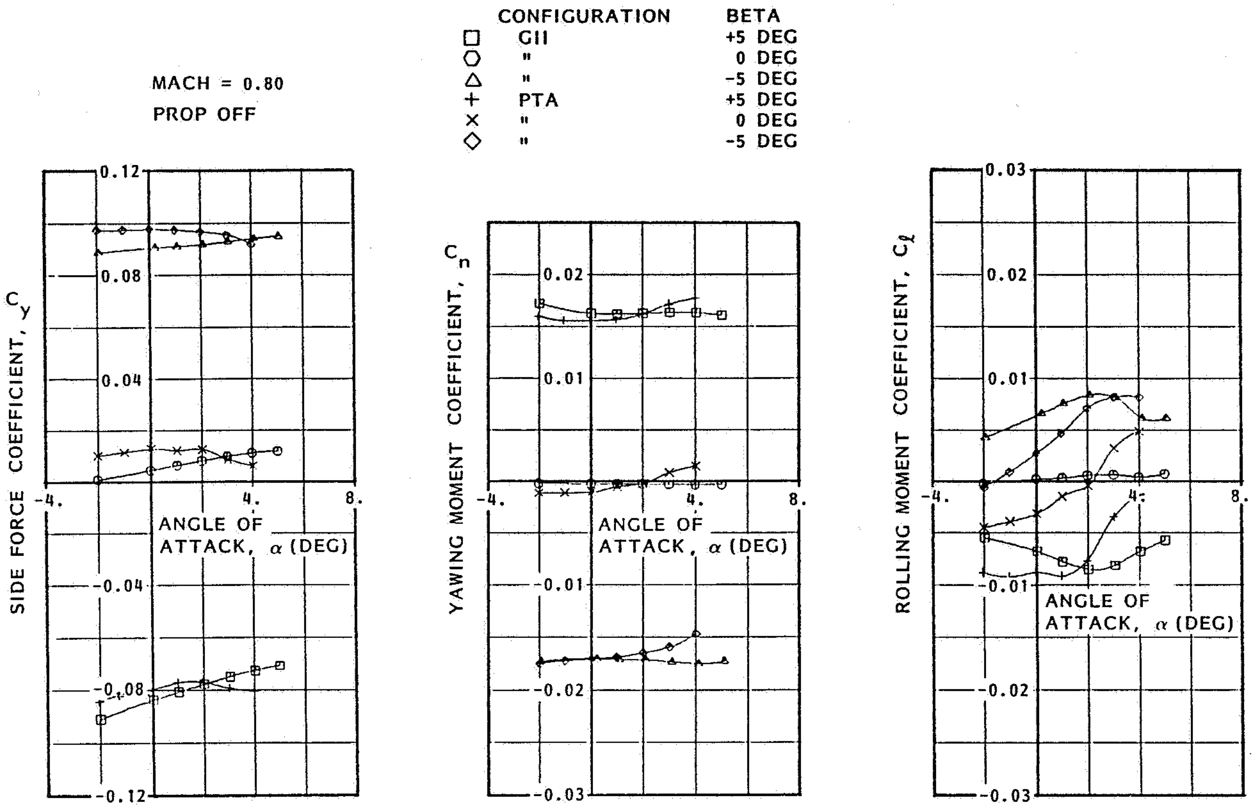

Figure 73. Comparison of GII and PTA in Sideslip - Mach 0.8

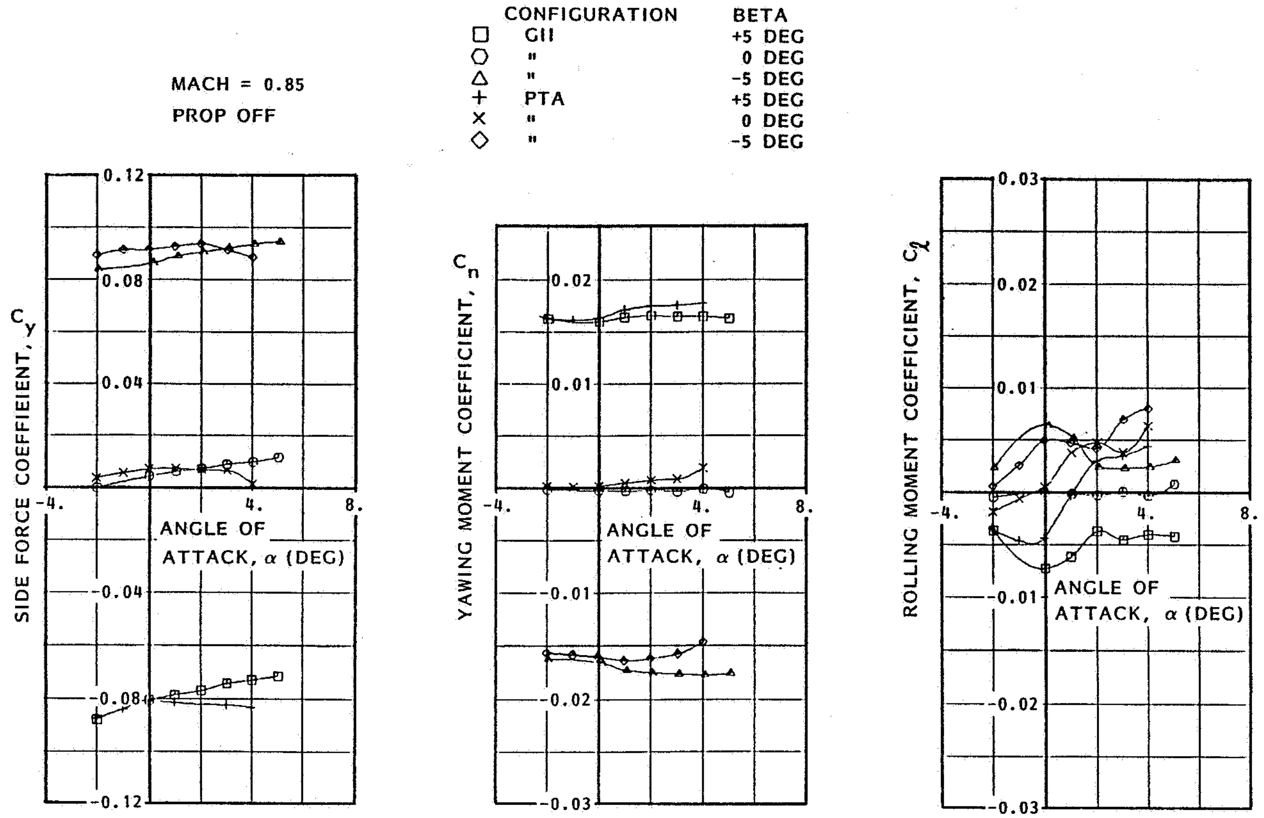

Figure 74. Comparison of GII and PTA in Sideslip - Mach 0.85

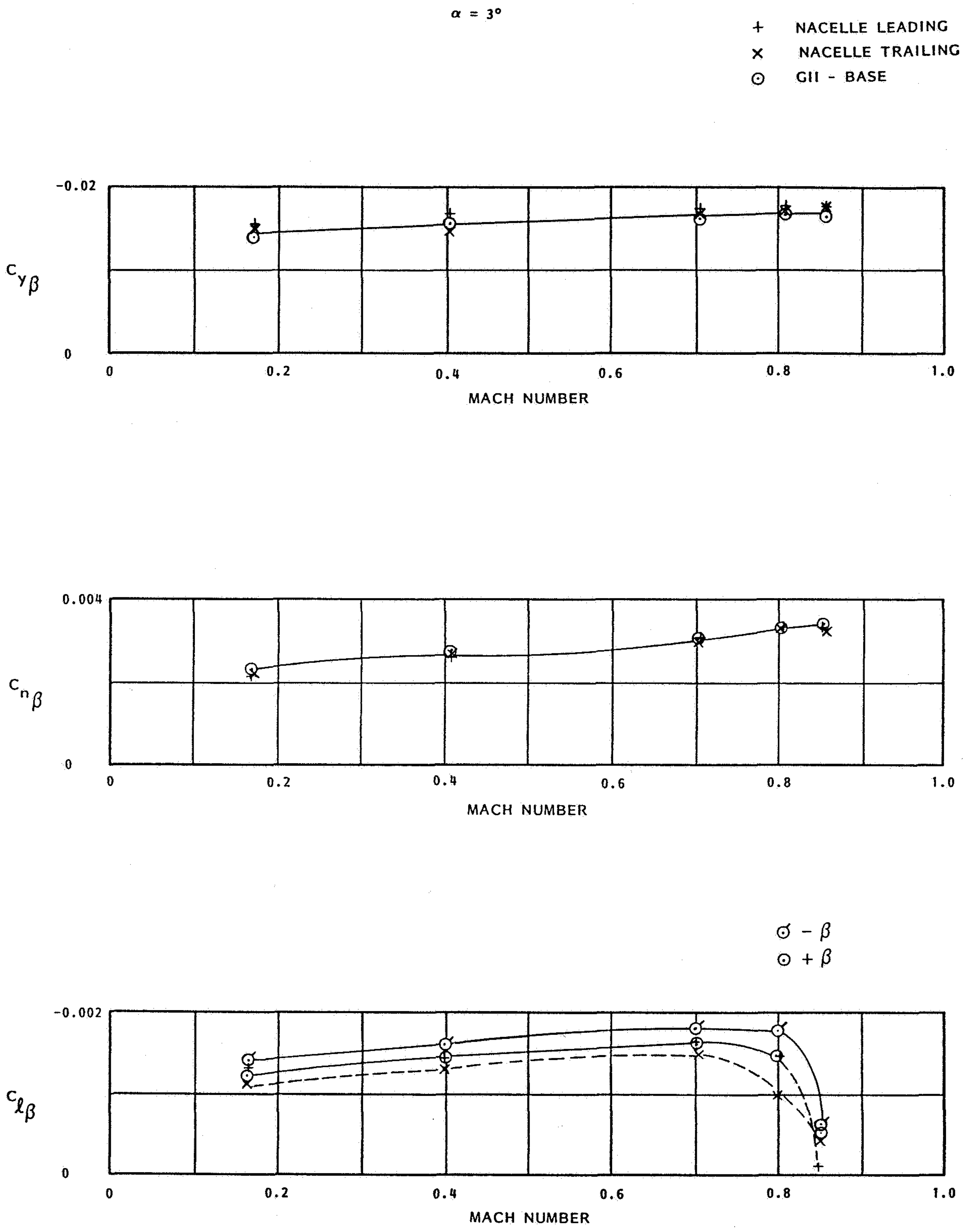

Figure 75. Effect of Mach Number on Sideslip Derivatives

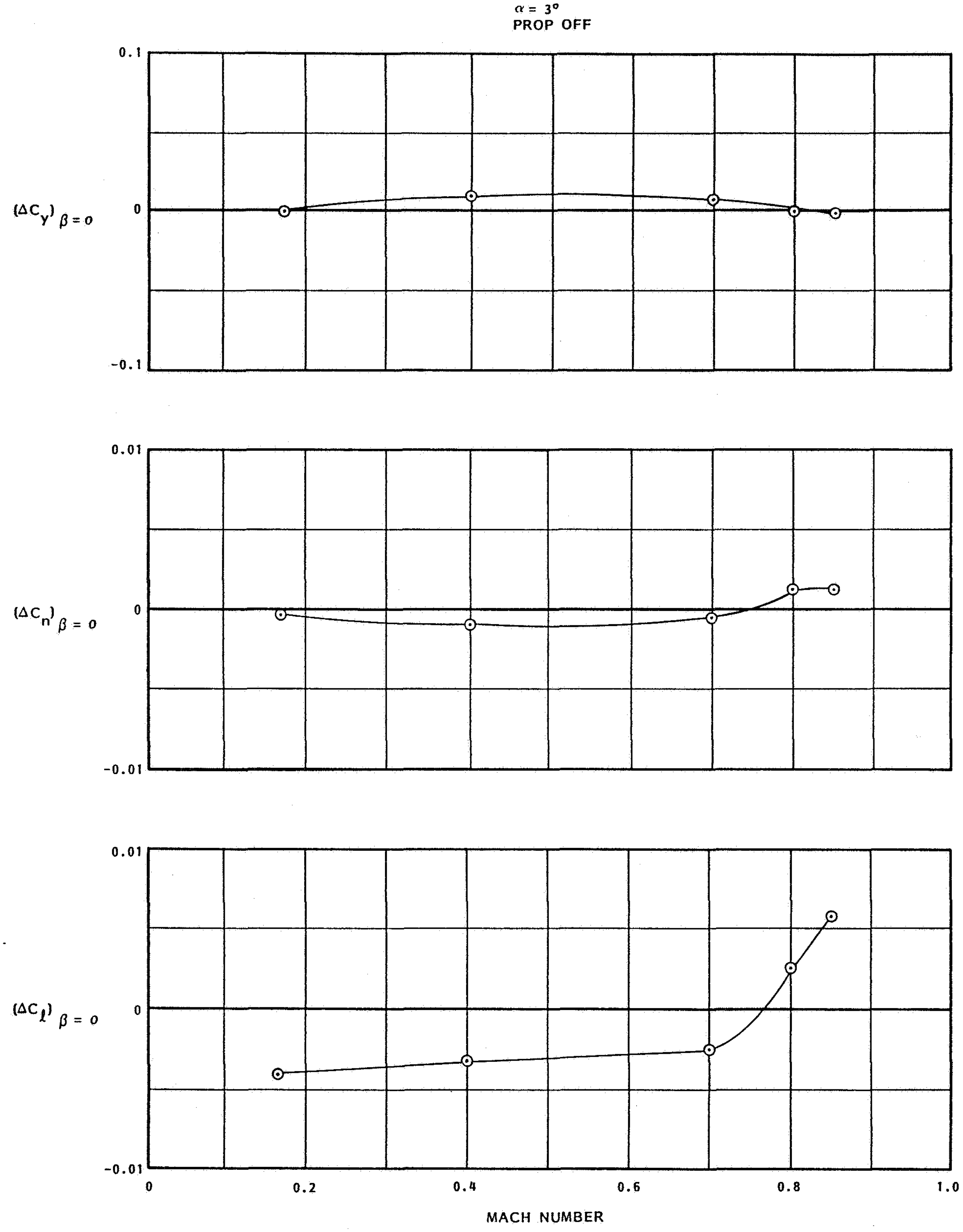

Figure 76. Effect of Mach Number on Lateral-Directional Offsets

7.3.8 Elevator Effectiveness - High Speed

No elevator data were obtained in the high-speed wind tunnel tests since no change in effectiveness was predicted. A possible change in tail angle of attack due to the nacelle, or local dynamic pressure changes, would have been the only source of a change in elevator effectiveness. The tail angle of attack change due to the nacelle is less than 0.5 degrees, and no local dynamic pressure change was detected.

7.3.9 Rudder Effectiveness - High Speed

The effectiveness of the rudder at small deflections (5 degrees) is shown in Figure 77 as a function of Mach number. These shapes are typical for a swept fin aircraft. The data show a higher level of effectiveness for the GII than is published together with a well defined compressibility effect. This is the only area of significant disagreement with published stability and control data in the whole test series. It is possible that the higher effectiveness level is due to non-metric loads on the sting cover. However, data obtained from the QUADPAN model at M = 0.45 and M = 0.8 tend to verify the level as measured. The PTA data, power on, shows a significant increase in rudder effectiveness relative to the GII at M = 0.4 and 0.7. At M = 0.8, an earlier break in the compressibility rise results in a slight reduction in rudder effectiveness. These changes would have little effect on the aircraft operation.

7.3.10 Aileron-Spoiler Effectiveness - High Speed

Aileron and spoiler effectiveness from M = 0.4 to M = 0.85 is shown in Figure 78. The aileron deflection of 10 degrees, trailing edge up, is the maximum travel. At low Mach numbers, the rolling moment due to 10 degrees of aileron is 7-percent higher than the GII published level. At high Mach number an early break in compressibility effect occurs and results in lower effectiveness beyond a Mach number of 0.7. The wind tunnel GII data has a similar Mach number effect as shown for an angle of attack of 3 degrees. The full-scale airplane has vortex generators on the upper surface of the wing outboard of the fence to take care of this phenomenon, and it is therefore assumed the PTA full-scale will have at least the GII full-scale effectiveness. Similarly, spoiler effectiveness is seen to be higher than the 55 percent of the full-scale GII level estimated for the PTA short span spoiler but with an early shock related loss. The vortex generators on the full-scale aircraft are expected to restore this level. Maximum spoiler deflection is nominally 35 degrees as shown in the low-speed section and is available at high speed.

7.4 LEX (LEADING EDGE EXTENSION) PERFORMANCE

The objectives of the LEX design and the methodology to achieve those objectives are described in Appendix A. Generally, it was desired to recontour the wing leading edge region so that it would be less sensitive to the upwash produced by the propfan slipstream.

Wind tunnel test data showing the effects of the LEX on wing pressure distributions are shown in Figures 79 and 80. Data are shown at Mach

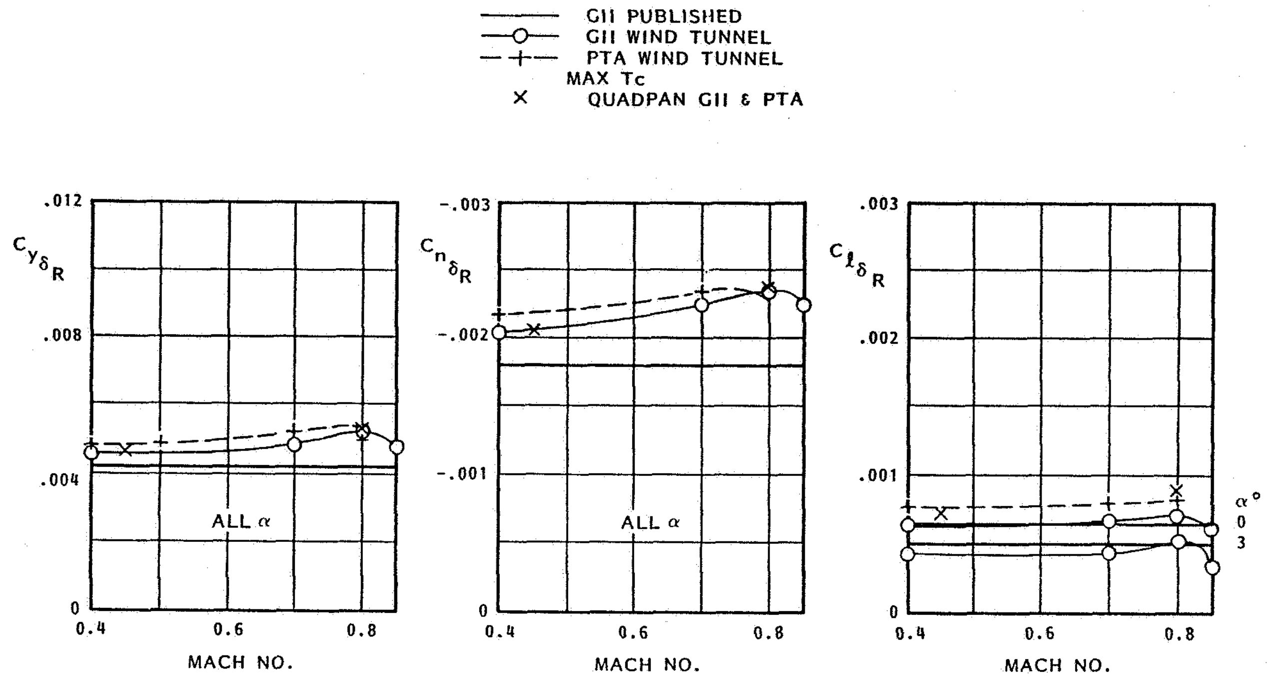

Figure 77. Comparison of Measured and Predicted Rudder Effectiveness

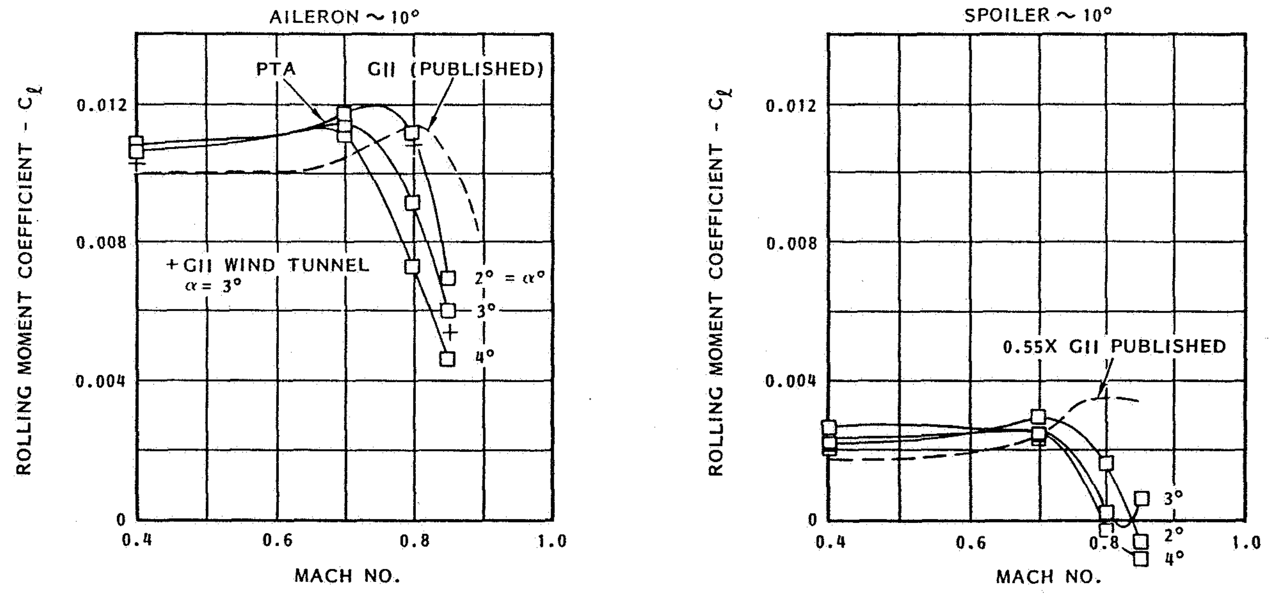

Figure 78. Aileron-Spoiler Effectiveness

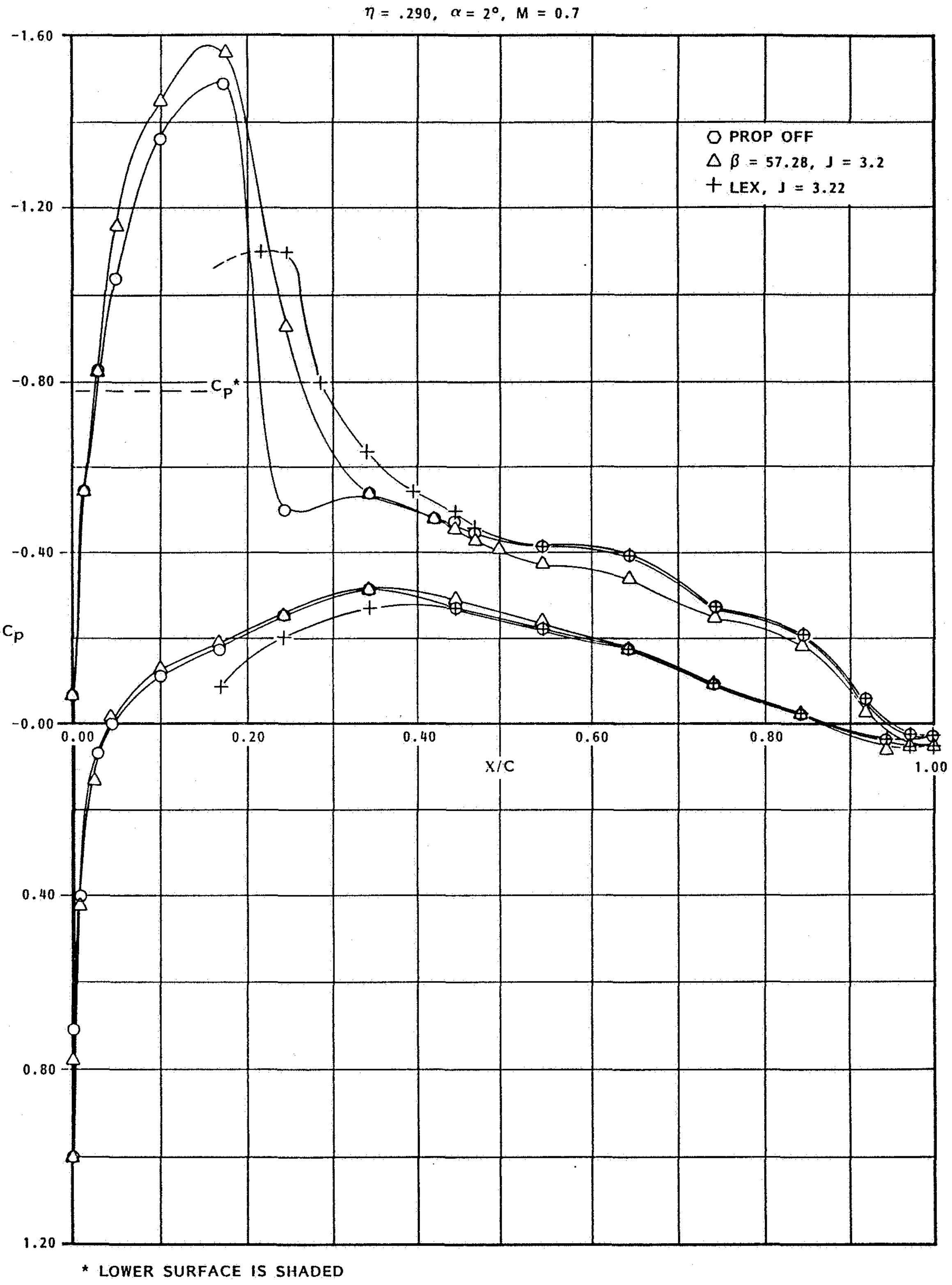

Figure 79. Effect of LEX on Wing Surface Pressures, Mach 0.70

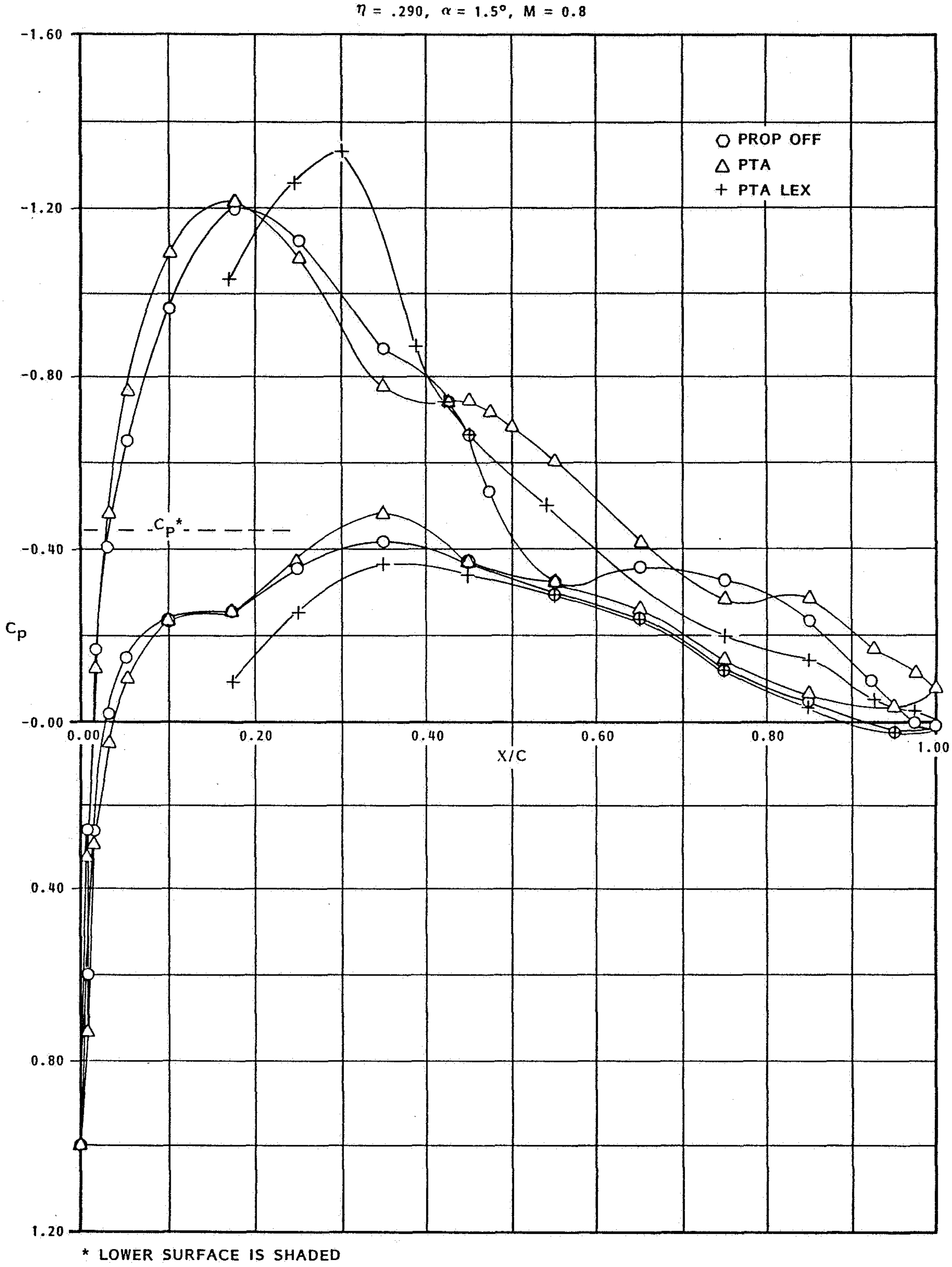

Figure 80. Effect of LEX on Wing Surface Pressures, Mach 0.80

numbers of 0.7 and 0.8 for the PTA basic configuration with and without the propfan and for the powered configuration with the LEX added. Unfortunately, there were no provisions in the LEX hardware itself for pressure measurements, so the first few points of the pressure distribution curves are missing for the LEX configuration. There are some conclusions that can be drawn, however, with the points available.

The pressure distributions shown in Figure 79 for the configuration with the LEX have the chord dimension adjusted for the additional length of the LEX. At Mach 0.7, it can be seen that the effect of power on the basic GII wing is the same as an angle-of-attack increase--there is a slight increase in Mach number (more negative C_p) and the shock wave is slightly further aft. For the same power condition with the LEX, however, there is considerably less acceleration over the front part of the airfoil. In this case, the LEX has clearly done what it was designed to do.

At Mach 0.8, the acceleration over the leading edge is not as strong with the LEX as without it, but the flow does accelerate to a higher Mach number. While this could have had a negative effect, this does not appear to be the case because the deceleration behind the peak is mild with no evidence of trailing edge separation as there was in the case without the LEX.

A drag polar plot for the Mach 0.8 case is shown in Figure 81. This plot confirms the success of the LEX design--showing that the addition of the LEX reduced drag at the design lift coefficient by approximately 29 counts. At higher lift coefficients, the effect of the softened leading edge of the LEX configuration is even greater; whereas at lower lift coefficients, the basic configuration does not get into as much trouble, and the benefits from the LEX are less.

7.5 WAKE SURVEY DATA

7.5.1 Wing Pressure Measurements

It was desired in the flow survey tests that flow about the semispan model match as closely as possible the flow about the full-span PTA model. To check that this was accomplished, comparisons were made of the wing pressure distributions from the flow field tests with those obtained in the 16-Ft Transonic Aerodynamics Wind Tunnel for the full-span model. These comparisons are shown in Figures 82 and 83 for two wing spanwise stations.

In Figure 82, for $\eta = .328$, the data from the flow field survey tests at zero angle of attack are compared with data from the 16-Ft Transonic Aerodynamics Wind Tunnel at zero and 1-degree angles of attack. It can be seen that the flow survey test data on the upper surface fall generally between the two data plots from the other tunnel. This implies that there is an effective angle-of-attack difference between the two facilities of the order of half a degree or less.

On the lower surface, there was a modification of the flow survey model to accommodate rake instrumentation tubes exiting the model. This produced a protuberance that caused the pressure distributions to be different from those in the full span model tests. However, in the leading edge region, the flow survey test data still fall between the other two curves.

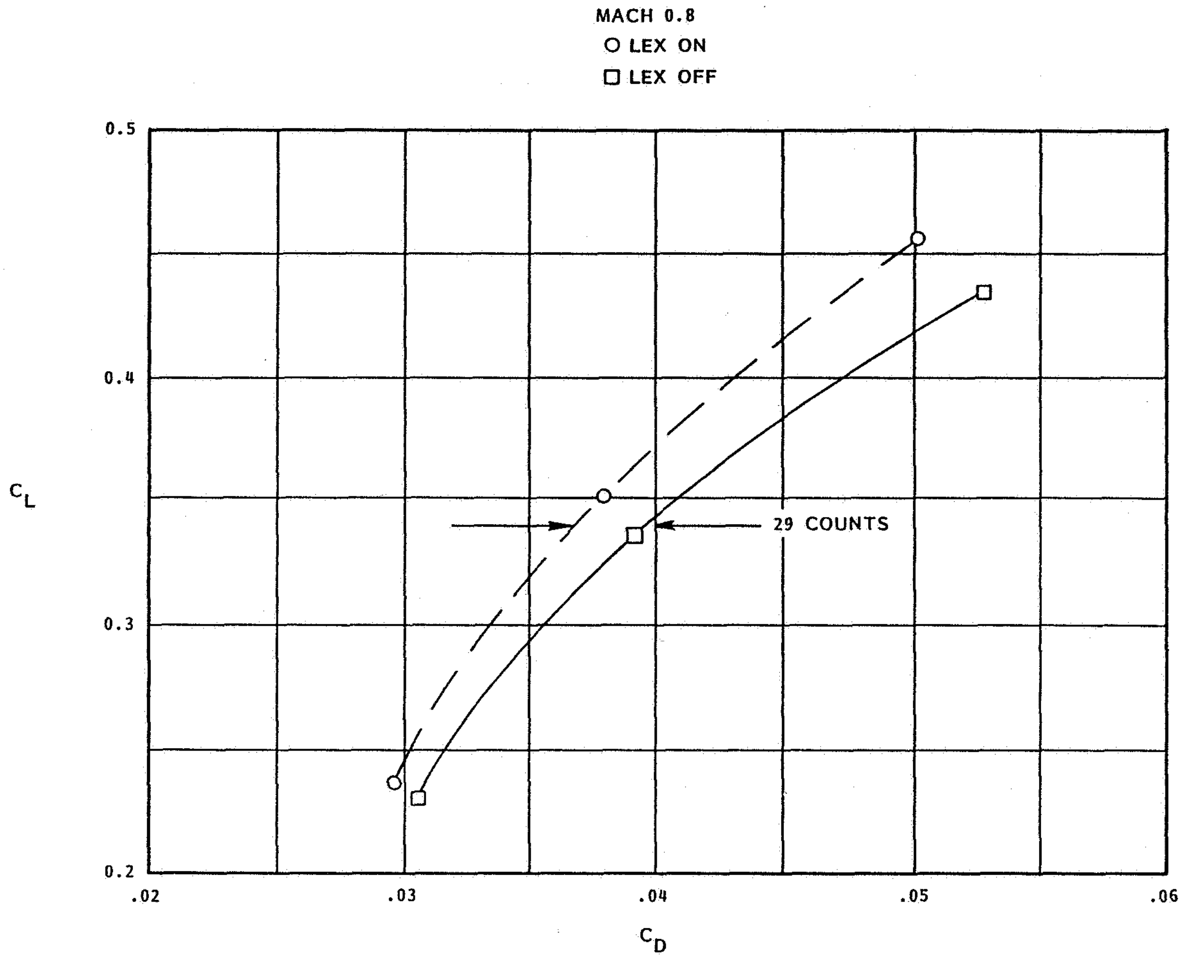

Figure 81. Effect of LEX on PTA Drag

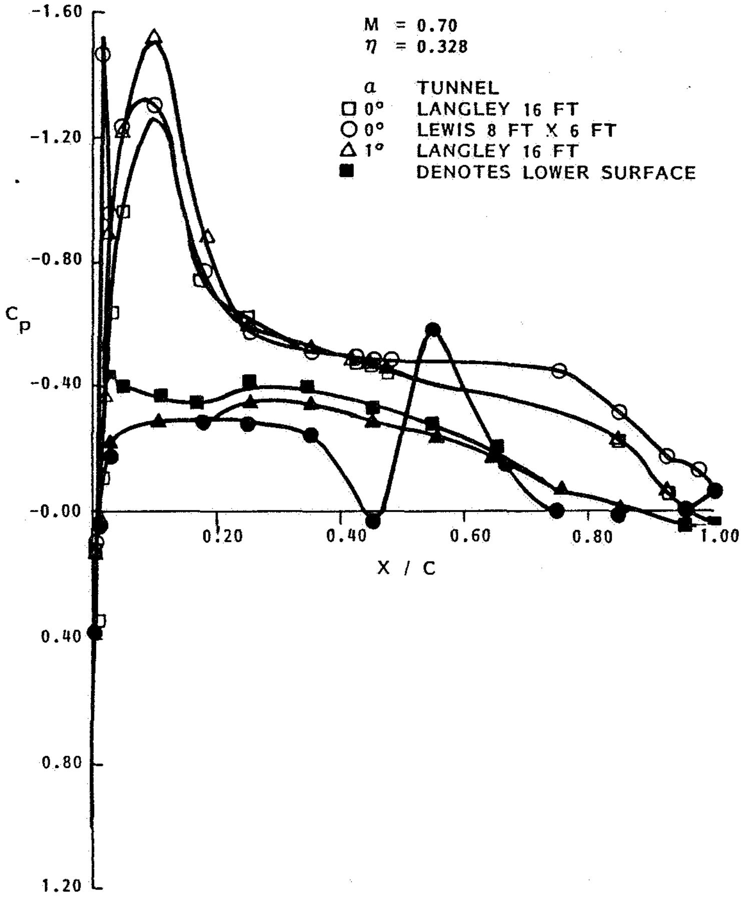

Figure 82. Pressure Distributions Inboard of Nacelle

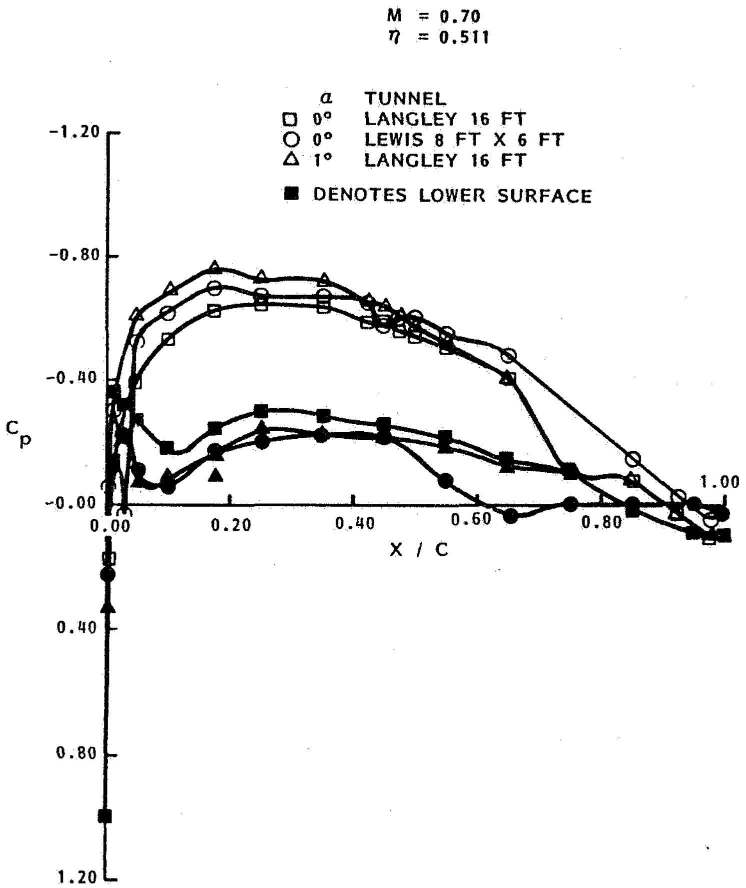

Figure 83. Pressure Distributions Outboard of Nacelle

On the outboard side of the nacelle, the data in Figure 83 exhibit the same characteristics as that seen in Figure 82. It was concluded then that the flow fields around the semispan model were basically the same as those around the full span model, but that the angle of attack in the flow field tests is effectively about one-half degree higher than that in the full-span model tests.

7.5.2 Flow Field Data

The use of 5-hole probes to measure three-dimensional velocity vectors is still somewhat an art--particularly in high speed flows. Consequently, some factors in these tests resulted in unexpected effects on the data. Looking at Figure 6, two features of the experimental set-up should be noted. First, the rakes were installed as close as possible to the inlet face on the model. This was done initially when it was thought that these tests would include powered effects; thus, the rakes were mounted so that one position would suffice for both prop-on and prop-off configurations.

The second feature to be noted is the attachment of the rake to the model. The bracket to which the rake attached presented a flow interference greater than desirable in a transonic flow. The effects of both the inlet lips and the support bracket were measured by the rake probes (as they should be). The prediction code, QUADPAN, on the other hand, was not paneled in sufficient detail to adequately model these features of the model hardware. Thus, as will be seen later, the predictions failed to reflect all of the flow nuances detected by the rakes.

Flow field data for Mach 0.6 are presented in Figures 84 through 86 in the form of values of the three velocity components U, V, and W normalized with respect to freestream velocity. In each figure data are presented for the rakes at four azimuthal positions.

In Figure 84, values are shown for the axial component U. The agreement of the data with the QUADPAN predictions is not very good. In Figures 85 and 86, the data for the vertical component W and the lateral component V show much better agreement with QUADPAN predicted values. It is natural to question whether the V and W data are credible when the U data show such poor agreement. It is believed, however, that the V and W data should be accepted for the following reasons. First, the measurement of U is an absolute value; the measurements of V and W, on the other hand, are relative--that is, they depend on differences between pressures measured at different points on the 5-hole probe. These relative measurements are inherently more accurate than the absolute. Therefore, even if the U value is in error, V and W may be correct.

The second reason is related. It has already been pointed out that the rakes are closer than desired to support and other model hardware. This proximity not only causes the rake to be in regions of local acceleration and deceleration that are not predicted by QUADPAN, but it also may produce spurious readings because the rake support is not exactly the same as that used in the calibration.

For these reasons, the approach taken in the discussion of the wake survey results has been to discount, somewhat, the data for the axial component U and to base conclusions primarily on the data for V and W.

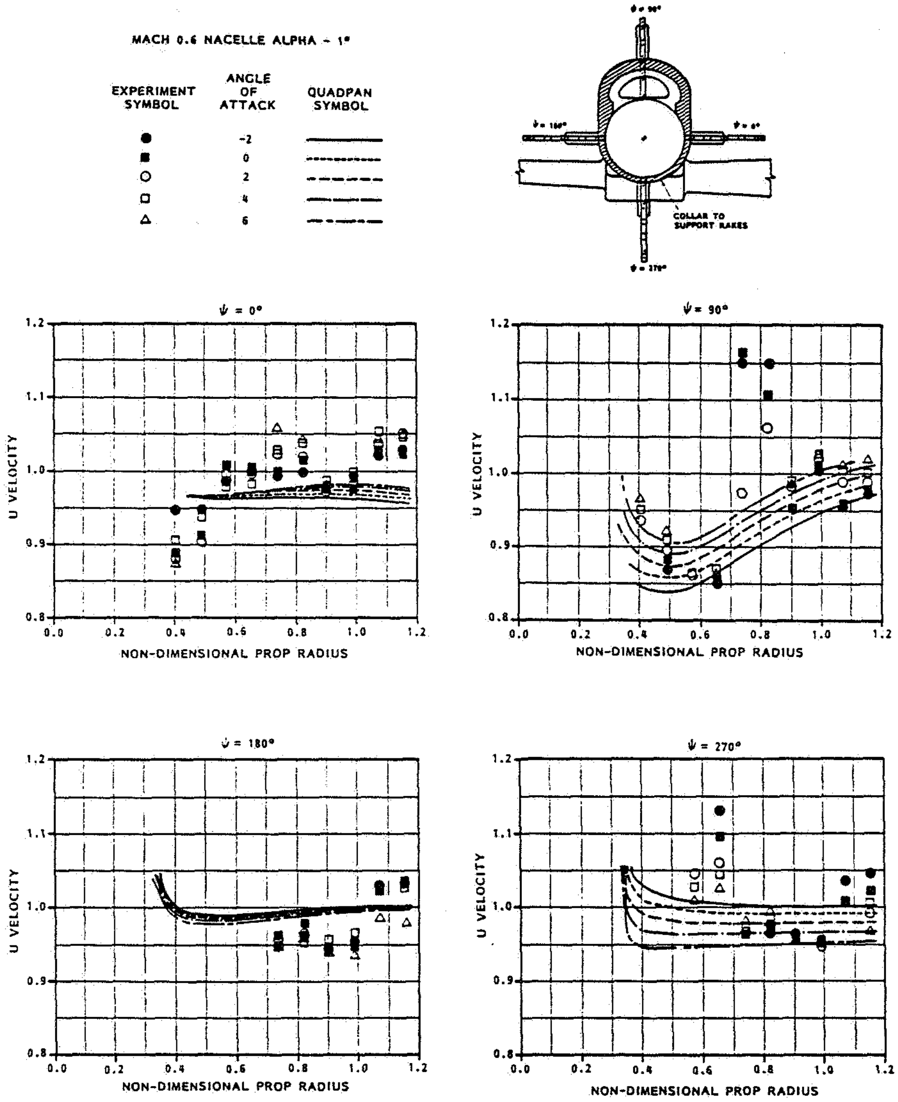

Figure 84. Rake Data for Axial Velocity Component U at Mach 0.6

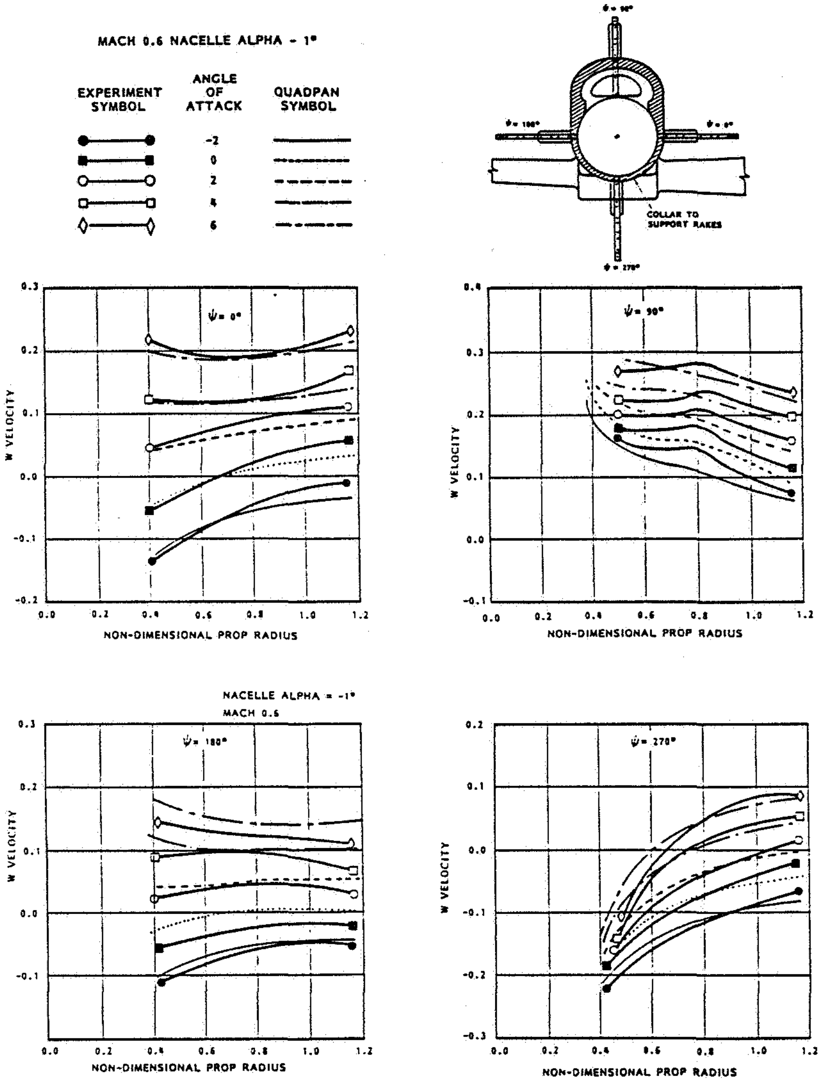

Figure 85. Rake Data for Vertical Velocity Component W at Mach 0.6

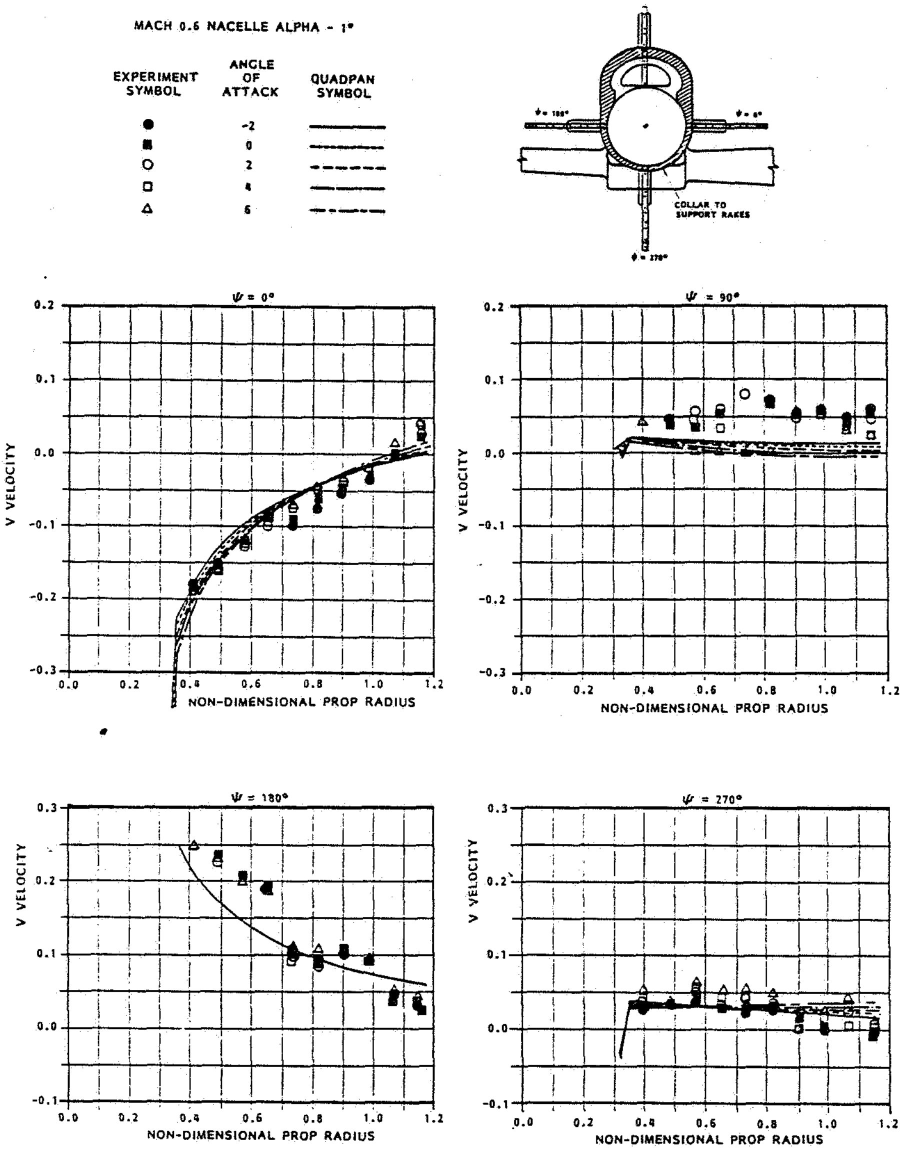

Figure 86. Rake Data for Lateral Velocity Component V at Mach 0.6

Data for the lateral component V show a much better self-consistency than those for U and a much better correlation with the QUADPAN predictions. In fact, overall, the agreement with predicted values is good except for the rake position in front of the inlet (ψ = 90 degrees). Here, the disagreement is attributed to the inadequacy of the QUADPAN paneling.

The data for the vertical component W in Figure 86 show an excellent agreement with the predicted values. At all four rake positions the variation of W with distance from the prop centerline and the variation with angle of attack are well predicted by QUADPAN.

Data recorded at Mach 0.85 are shown for the three velocity components in Figures 87 and 88. The trends observed in the lower Mach number data are generally repeated in these figures. Obviously, there is no breakdown in the QUADPAN code at the higher Mach number.

These flow field measurement tests were performed for the purpose of demonstrating that the subsonic inviscid code QUADPAN can be used to predict the propfan flow field for all the conditions of the PTA flight test program. In spite of the difficulties experienced, it is believed that the data provide this demonstration.

7.6 ISOLATED PROPELLER TEST

The goal in the isolated propeller tests was to assess the propeller performance in the absence of installation effects. In order to do this, the propeller should, ideally, have a support nacelle no larger than the hub diameter of the propeller. Because this support must enclose the propeller drive system and all the necessary instrumentation to monitor propeller performance, this ideal was impractical, so an axisymmetrical nacelle as small as possible was employed.

Tests were run at Mach 0.4 with the thrust axis angle of attack ranging from -2 to 12 degrees and propeller blade pitch set at 49 degrees (measured at the 3/4-blade radial station). Six advance ratios were set by varying the propeller rotational speed from 11,000 to 16,000 rpm. Vibration problems precluded testing at Mach numbers higher than 0.4

The data obtained from the hub balance included propeller axial force, normal force, and pitching moment. Using the air motor drive pressure, propeller rotational speed, and previous calibration data, the torque and horsepower absorbed by the propeller were deduced. These data allowed the determination of propeller performance and its variation with propeller advance ratio and angle of attack.

Thrust and power coefficients, plotted against propeller advance ratio reflect propeller performance. These are plotted in Figures 89 and 90. The data are in good agreement with analytical prediction and also correlate well with that predicted for the full-scale propeller.

Data from the isolated propeller test in the Langley 4M x 7M Subsonic Wind Tunnel are shown in Figures 91 and 92. Data are shown for blade pitch angles of 38 degrees and 40 degrees. Correlation with theory here is not as good as in the high-speed tests. One reason for this discrepancy is that the mounting system in the 4M x 7M is more intrusive (see Figure 12)--producing a nacelle of increased cross-sectional area, and the support system is closer to the propeller plane.

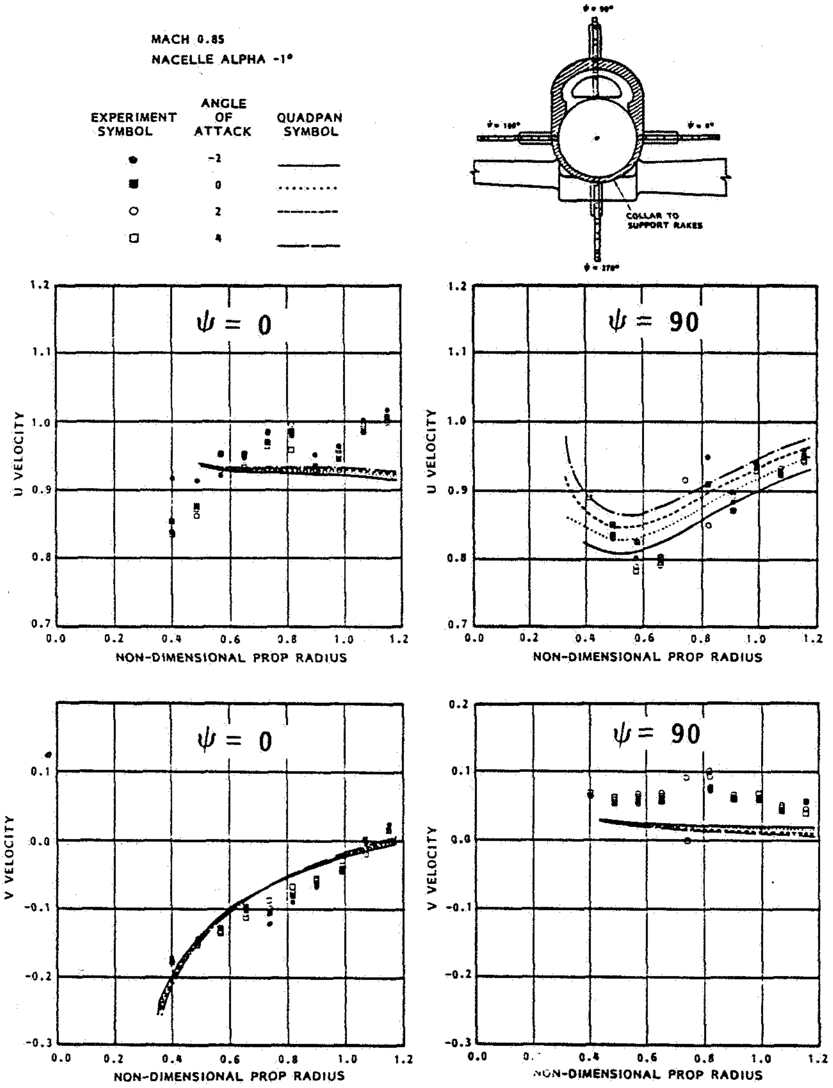

Figure 87. Rake Data for Axial and Lateral Velocity Component at Mach 0.85

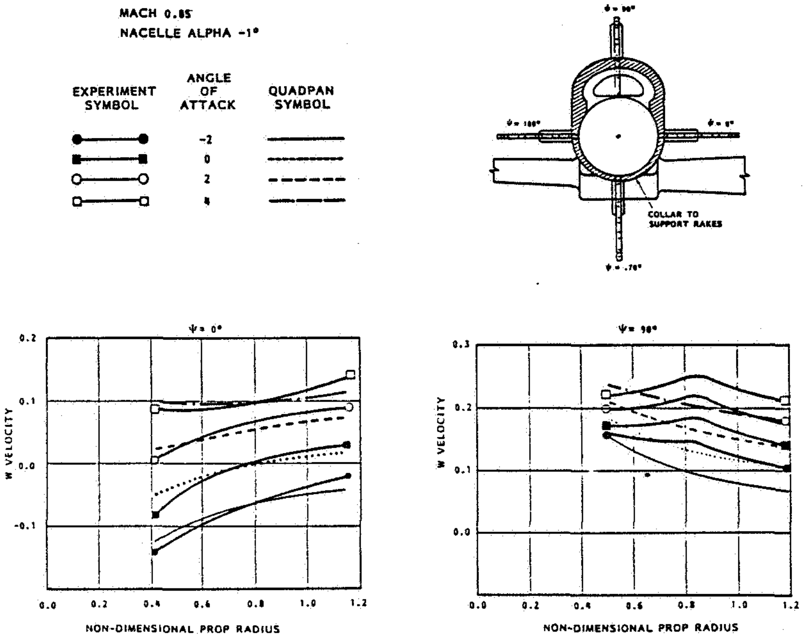

Figure 88. Rake Data for Vertical Velocity Component W at Mach 0.85

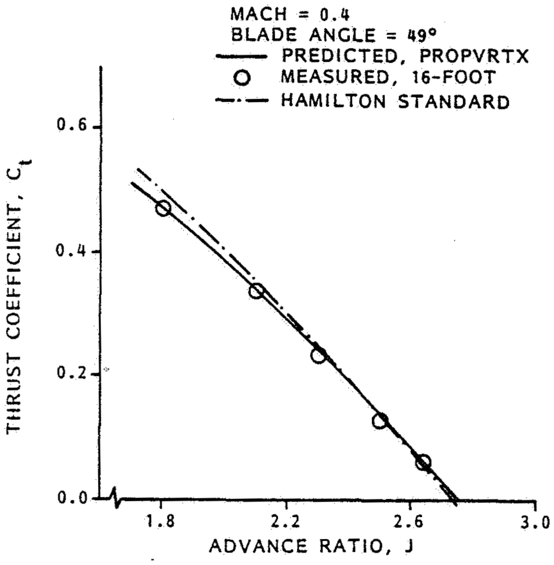

Figure 89. Thrust Coefficient Data at Mach 0.4

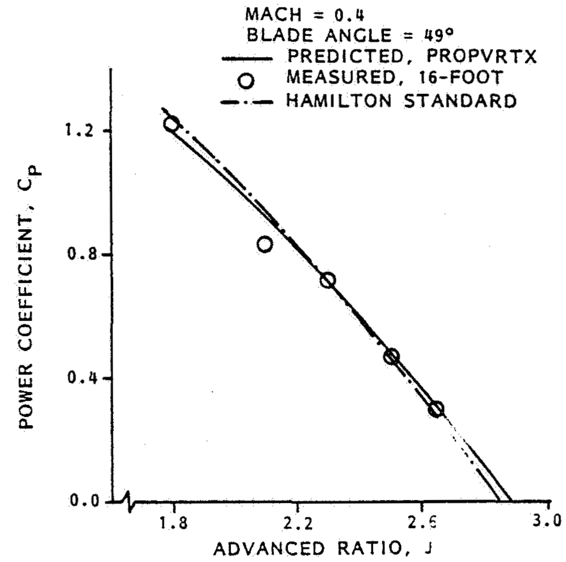

Figure 90. Power Coefficient Data at Mach 0.4

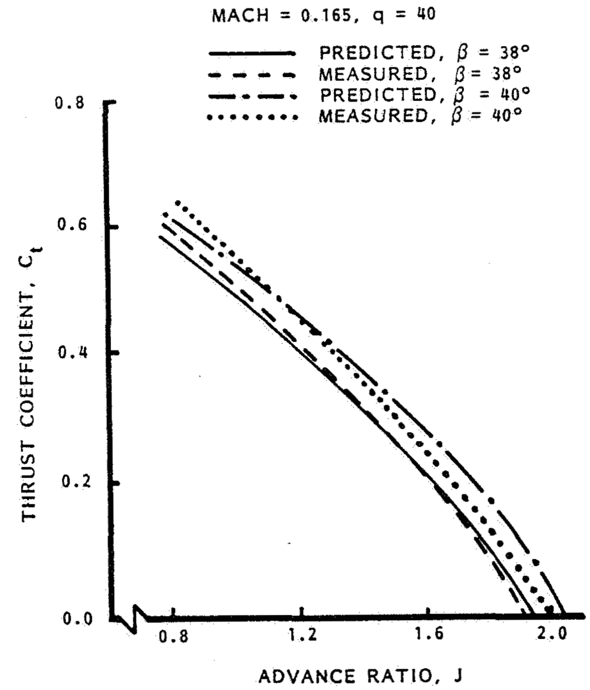

Figure 91. Thrust Coefficient Data at Mach 0.165

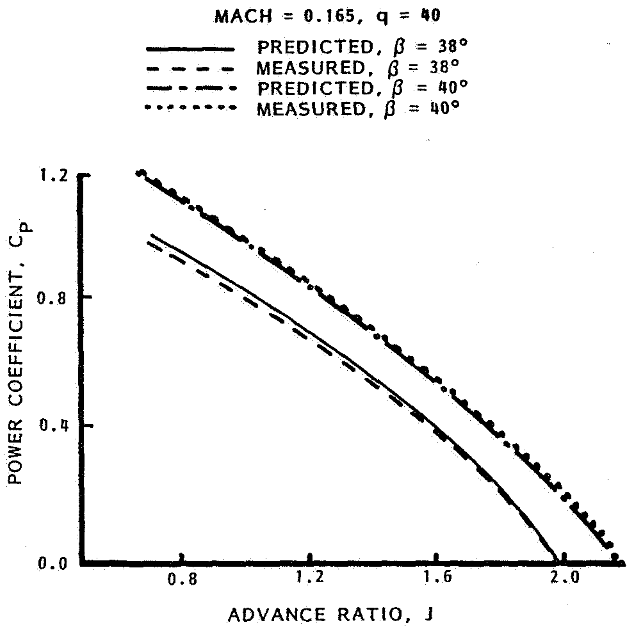

Figure 92. Power Coefficient Data at Mach 0.165

When the thrust axis of the propeller is inclined to the freestream, the propeller blades no longer experience uniform aerodynamic loading but are subject to cyclically changing forces, the magnitude, of which depends on the blades azimuthal location. The period of these changes is the same as that which the blades take to complete one revolution. Some insight into the origin of these loads can be obtained by examining the behavior of a blade element during the course of rotation. Figure 93 shows side and front views of a propeller disk with the thrust axis inclined at α_t to the freestream velocity V_0. The freestream velocity can be resolved into component $V_0 \cos \alpha_t$, normal to the plane of rotation, and component $V_0 \sin \alpha_t$ parallel to the plane of rotation.

A blade section operates with an equivalent freestream velocity of magnitude $V_0 \cos \alpha_t$ and a rotational component $\omega r + V_0 \sin \alpha_t \cos \psi$, constant in direction but varying in magnitude with azimuthal position. Consequently, the blade can be considered to operate at a varying advance ratio. This variation is sinusoidal and reaches a maximum along $\psi = 0$ degrees and a minimum along $\psi = 180$ degrees.

Consider the blade element shown in Figure 94. The blade element undergoes cyclic changes in local blade angle of attack. This variation is plotted against azimuthal location for three radial stations of 0.35, 0.55, and 0.75 in Figure 95. Subsequently, this gives rise to a cyclic blade thrust and torque. The cyclic thrust gives rise to a steady yawing moment while the cyclic torque gives rise to a normal force. The reduction in forward velocity from V_0 to $V_0 \cos \alpha_t$, reduces the advance ratio correspondingly and, as will be shown later, results in a $J \cos \alpha_t$ shift in the performance data.

Figure 96 shows the variation of steady propeller thrust coefficient with thrust axis angle of attack. The offset of the minima of these curves is due to tunnel and model support upwash. As angle of attack is increased or decreased from these minima (net zero angle of attack), the thrust increases. The sensitivity of thrust to angle change is a maximum at the highest advance ratio of 1.8 and a minimum at an advance ratio of 0.9. This is directly related to the effective advance ratio $J \cos \alpha_t$. Figure 97 shows curves of the thrust coefficient versus advance ratio at a zero angle of attack and 16 degrees angle of attack. These curves also show the increase in thrust due to thrust inclination. Figure 98 shows the two curves plotted versus $J \cos \alpha_t$, and they almost collapse to a single curve. The reason they do not completely collapse is there is some residual upwash due to the support system, and the geometric angle of attack needs to be adjusted for that interference effect.

A propeller at angle of attack produces a normal force and an accompanying yawing moment due to the fluctuating periodic loads on the blades as explained earlier. The normal force increased linearly with propeller angle of attack as shown for the 1/9-scale SR-7 at Mach 0.4 obtained in the 16-Ft Transonic Aerodynamics Wind Tunnel. On increasing the advance ratio, the normal force coefficient increased giving a family of straight lines. Theoretically, they should all pass through the origin, because there should be no normal force at zero angle of attack, but because of the residual upwash in the tunnel, there is some normal force at zero alpha.

Figure 99 shows normal force data from the 4M x 7M Subsonic Wind Tunnel at Mach 0.165. Here the data is not linear but shows the variation due to changes in upwash caused by the support system at the different angles of attack.

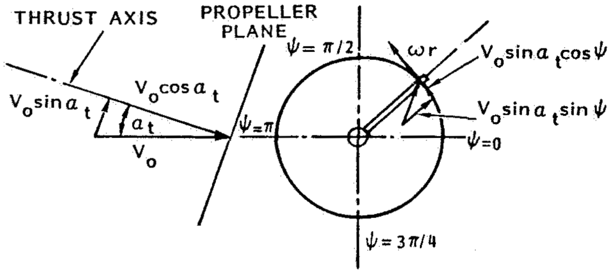

V_o - FREE STREAM VELOCITY
α_t - PROPELLER ANGLE OF ATTACK

Figure 93. Propeller at Angle of Attack

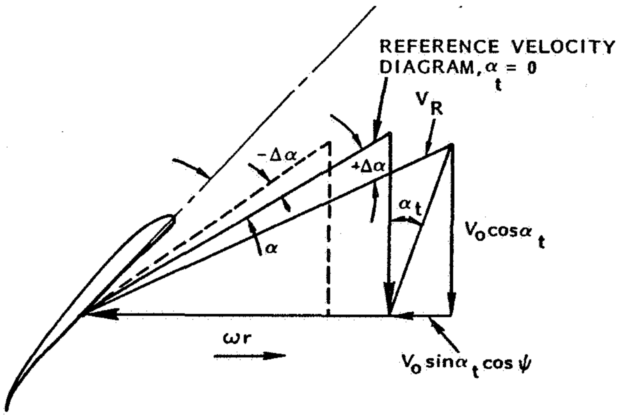

Figure 94. Changes in Blade Angle of Attack Due to Thrust Axis Inclination

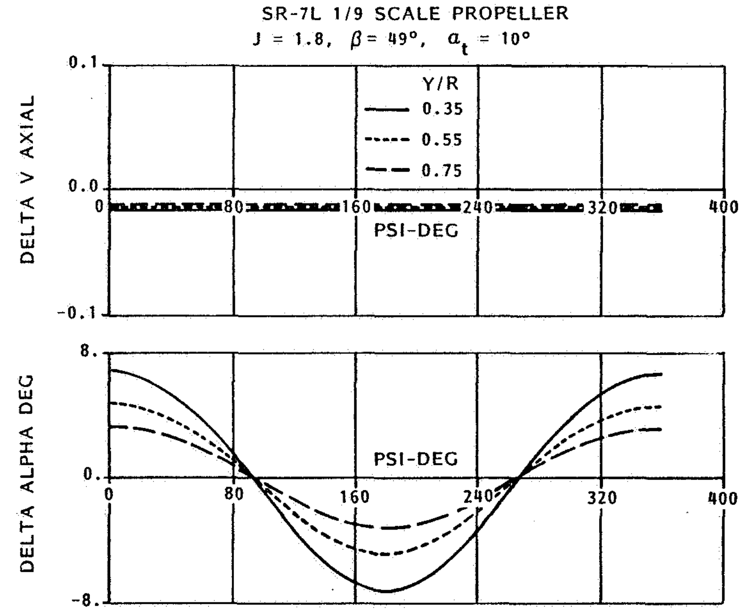

Figure 95. Cyclic Variation of Blade Environment Due to Thrust Axis Inclination

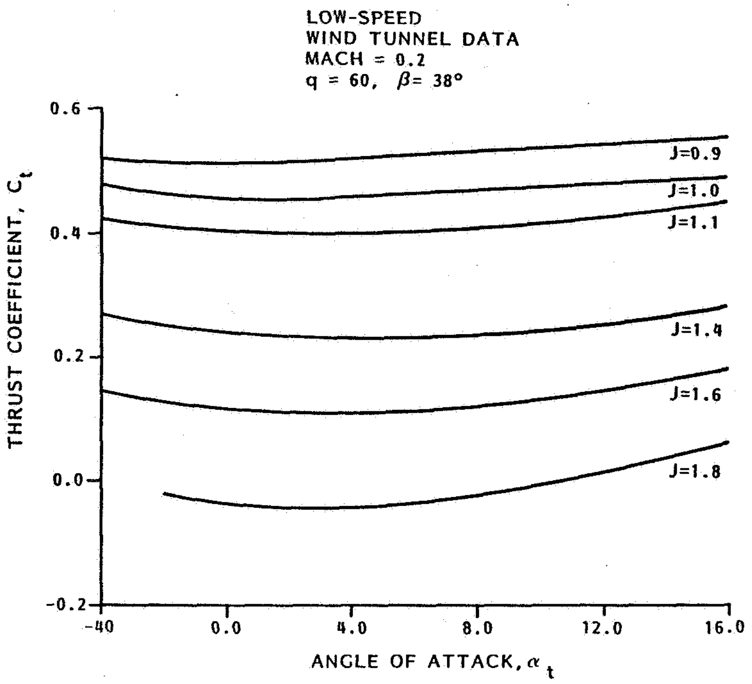

Figure 96. Thrust Coefficient Versus Angle of Attack

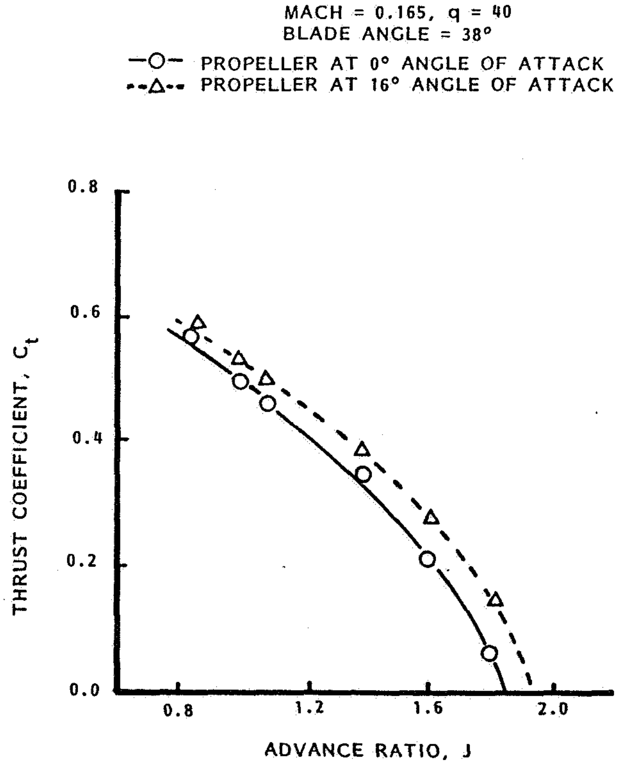

Figure 97. Thrust Coefficient Versus Advance Ratio at Two Angles of Attack

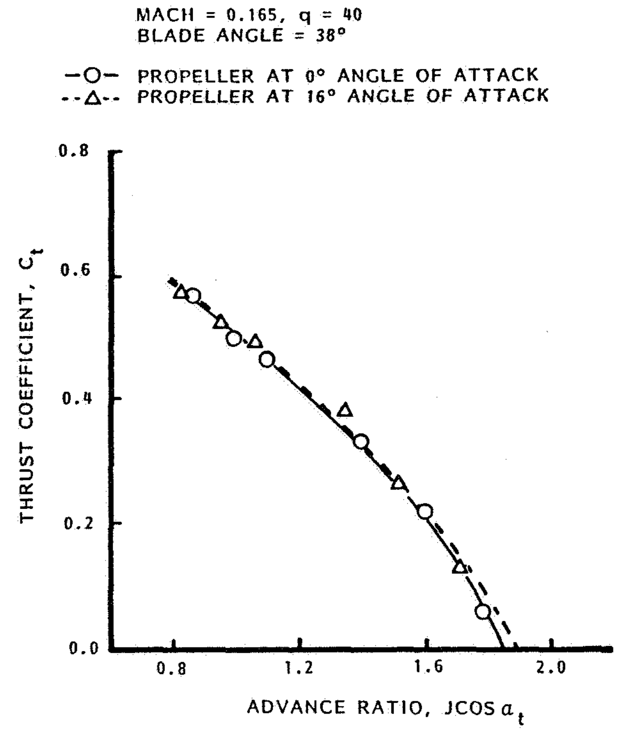

Figure 98. Collapse of Thrust Coefficient Data on J Cos a_t

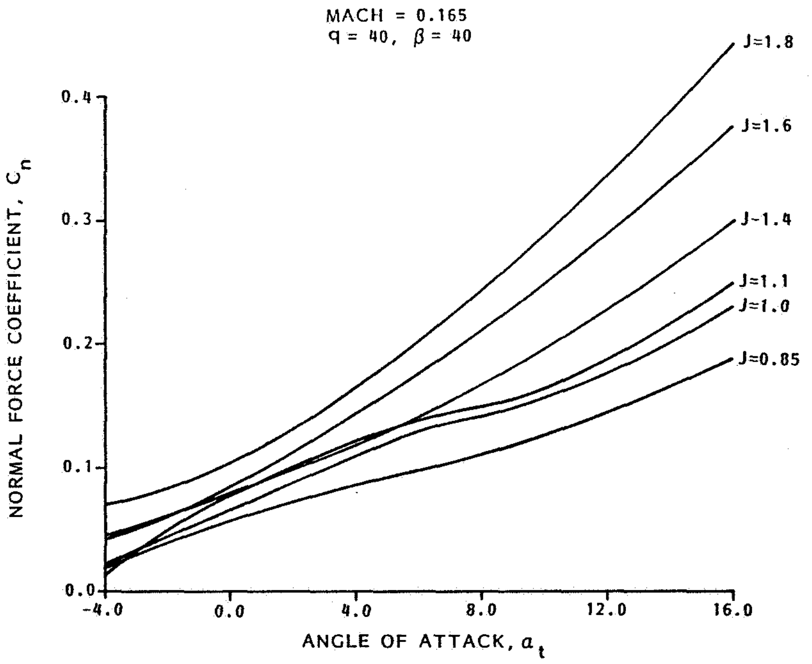

Figure 99. Normal Force Coefficient Data Versus Angle of Attack

8.0 CONCLUDING REMARKS

1. Performance data from these wind tunnel tests were validated in two ways. The data for the GII configuration were validated by comparison with published data for the GII aircraft. Good agreement was found. Data for both the GII and the PTA model configuration were compared with analytical predictions made with the Lockheed codes QUADPAN and PROPVRTX. Again, the agreement was good.

2. At moderate angles of attack and subsonic speeds, the impact of the PTA modifications on aircraft performance were to increase lift slightly and increase drag by about 15 percent. The drag increment increased rapidly above Mach 0.6, however, and at the design cruise Mach number of 0.8, the drag increment was about 30 percent of the basic GII drag. Maximum lift coefficients were reduced by the PTA modifications.

3. The PTA modifications reduced longitudinal stability slightly but had negligible effects on lateral and directional stability.

4. Roll control power was significantly reduced from the GII values--primarily because some of the GII spoiler panels were deactivated for the PTA installation. Rudder and elevator effectiveness, on the other hand, were only slightly affected.

5. Test results showed that a leading edge extension (LEX) designed for the wing on the inboard side of the nacelle would likely reduce aircraft drag in the high-speed drag rise range if it were needed.

6. Three-component velocity surveys in the high-speed flow field just behind the prop plane showed reasonable correlation with theory in some cases, and not so good correlation in others. Correlation was best for the transverse components where measurement accuracy was better. A major objective of these tests was to determine if there was a significant deterioration of the correlation at the transonic speeds. The data indicate that this was not the case.

7. A concern at the beginning of this program had to do with the design of small-scale propfan rotors to properly simulate the significant characteristics of the full-scale rotors. Isolated propfan rotor tests were performed to provide data so that scale corrections could be applied. Results showed a good correlation between predicted and measured rotor performance.

PRECEDING PAGE BLANK NOT FILMED

APPENDIX A

DESIGN OF THE LEX (LEADING EDGE EXTENSION)

Transonic drag of the PTA configuration was a major concern in the design program. It was recognized that the combination of: (a) wing unsweeping by addition of the PTA nacelle, (b) local-wing-angle-of-attack increases due to the swirl of the slipstream, and (c) flow channeling by the fuselage/wing/nacelle configuration held the potential for significant unpredictable drag rise.

In recognition of these concerns, several drag reduction devices were explored analytically, and one was selected to be tested in the tunnel program. The latter was a leading edge extension (LEX) on the inboard side of the nacelle. Its purpose was to recamber the wing in that region most likely to be negatively affected by slipstream swirl.

DESIGN OBJECTIVES

The LEX design employed a desired or target pressure distribution as the "optimization" criterion because surface pressures may be used to qualitatively evaluate the drag characteristics of a configuration. In the transonic regime, they can reveal the presence of shock waves and thus the wave drag associated with the configuration. Design experience allows one to derive a suitable target pressure distribution for a given surface. In the transonic case, the target wing sectional pressure on the upper surface should have no leading edge peaks which lead to premature shock wave compressions, but rather a pressure coefficient distribution that is well-rounded, indicating a controlled flow acceleration to supersonic velocities, followed by a return to subsonic flow through a near shockless recompression. The adverse pressure gradient approaching the trailing edge should be gentle enough so that no rear separation occurs. Collectively, the section pressure distributions can be assessed by examining the wing isobar pattern. Any loss of isobar sweep due to localized high suction peaks and steep adverse pressure gradients should be avoided. Since the original GII wing embodied the aforementioned design criterion, the target adopted in the LEX design was to restore the PTA wing flow to patterns similar to that of the GII wing.

DESIGN PROCEDURES

The planform extent of the modification was established as shown in Figure A-1, and three wing control sections were chosen. At these three sections the wing chord was extended forward and reshaped to better accommodate the upwash in the juncture area from the slipstream swirl. The extension was blended with the nacelle, care being taken to keep the frontal area a minimum.

The basic design procedure is shown schematically in Figure A-2. First, SUNTAN, a two-dimensional transonic code, was employed to produce wing sections approaching the desired contours at the control sections. The upper surface is more critical than the lower and was blended into the original wing so as not to cause premature recompression or "kinks" in the pressure distribution. On the lower surface, the junction area will cause

PRECEDING PAGE BLANK NOT FILMED

a sudden pressure drop, but since the lower surface is less critical this should not significantly affect the performance of the LEX. A section redesign is shown in Figure A-3. The three-dimensional LEX region was then built by appropriate lofting between these control sections using CATIA.

The design procedure is used a second time using a three-dimensional transonic code--a modified version of the Jameson full-potential flow code, FLO22NM, which includes nacelle and slipstream effects. Once a satisfactory wing surface was obtained, the QUADPAN program was used to contour the LEX/nacelle junction region. As might be expected, some of the steps in this process were repeated to resolve any undesired behavior.

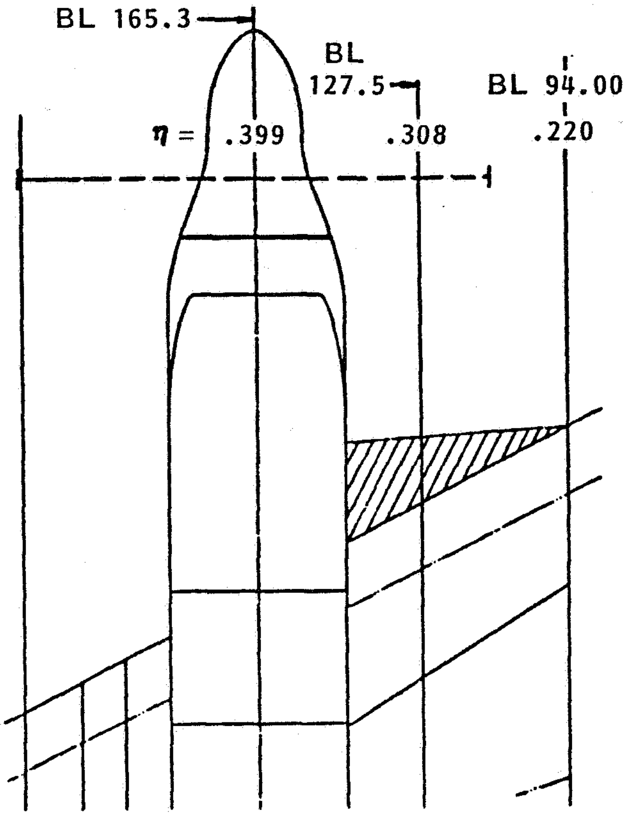

Figure A-1. Planform View of Leading Edge Extension (LEX)

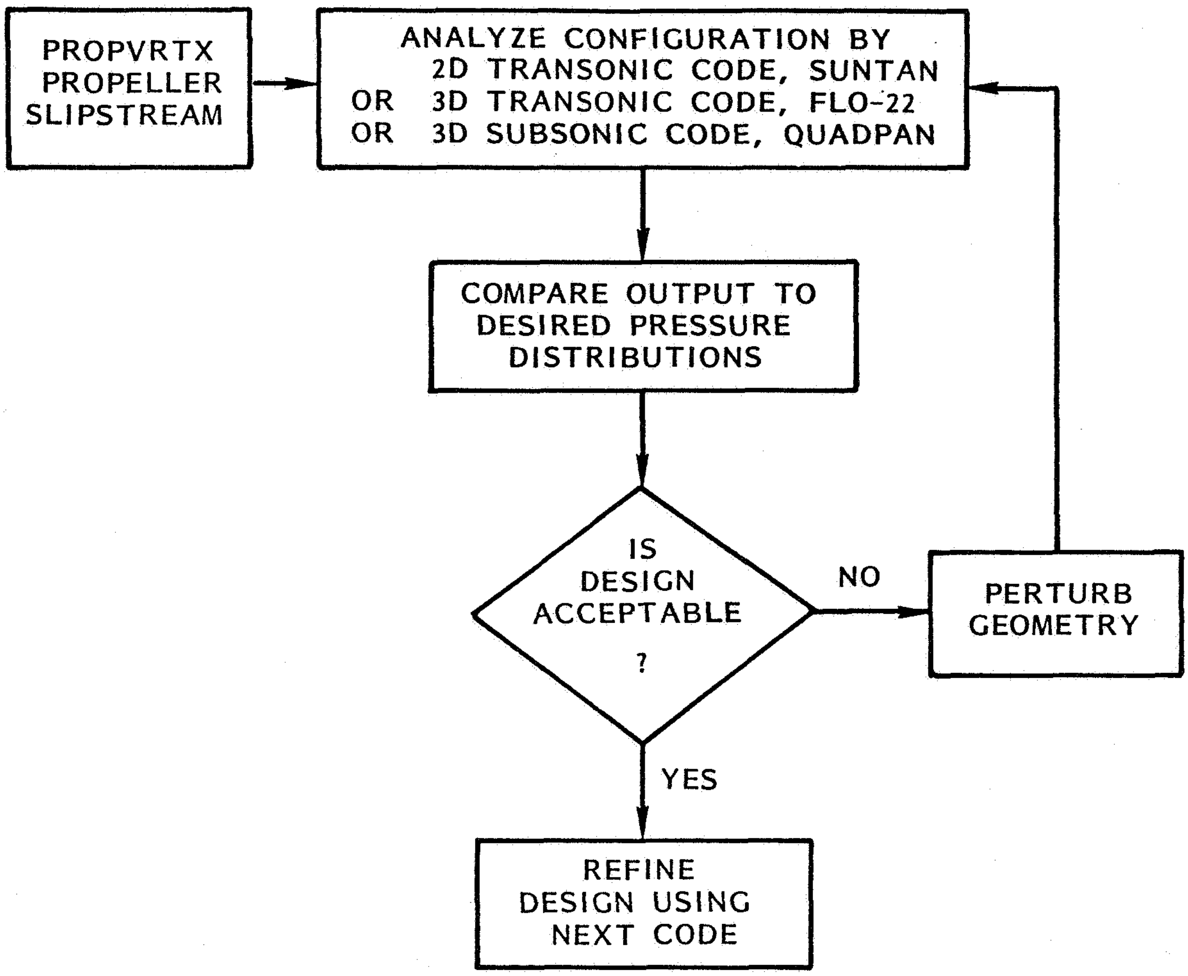

Figure A-2. Aerodynamic Design Procedure for LEX

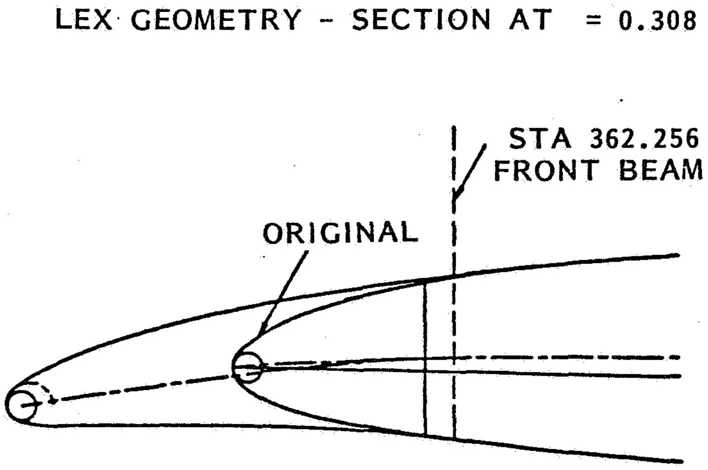
LEX GEOMETRY - SECTION AT = 0.308

Figure A-3. Airfoil Section Modification for LEX

APPENDIX B

CALIBRATION AND DATA REDUCTION FOR 5-HOLE PROBES

The 5-hole probes were calibrated in the Lockheed-Georgia Company CFWT Transonic Wind Tunnel at Mach numbers to 0.95. The calibration consisted of a procedure of placing each rake, in turn, in known flow conditions and measuring the pressure at each orifice on the rake. The flow conditions were varied by changing the roll and pitch angle settings of the rake and varying the test section Mach number. The variations in flow conditions are shown below:

Pitch Angle (Theta)	Roll Angle (Phi)	Mach Number
0 to 22 Degrees in 2-Degree Increments	0 to 360 Degrees in 15-Degree Increments	0.3, 0.6, and 0.9

The acquisition of these data required 900 runs with each run consisting of a single flow condition. Additionally, data were acquired for Mach numbers from 0.2 to 0.90 in M = 0.1 increments and, in the range from 0.90 to 0.95 in M = 0.05 increments for pitch angles of 0, 10, and 20 degrees and roll angles of 0 and 90 degrees.

The first rake was a prototype and was not fully calibrated. It was tested for development of the calibration procedure and checkout of the rake design. Rakes 2 and 3 were fully calibrated in test CFWT 101 and test CFWT 104, respectively.

The pressure data measured at each orifice on a probe was used to calculate functions for probe-sensed flow pitch angle (alpha), yaw angle (psi), total pressure (H), and dynamic pressure in the following manner:

$$f(q) = Cp_5 - Cp_m \quad \text{where } Cp_m \text{ is the minimum of } Cp_1,\ Cp_2,\ Cp_3,\ \text{and } Cp_4$$

$$f(\text{alpha}) = (Cp_3 - Cp_1) / f(q)$$

$$f(\text{psi}) = (Cp_2 - Cp_4) / f(q)$$

$$f(H) = (1.0 - Cp_5) / f(q)$$

The data from the cone static were not used in generating the calibration due to difficulties in obtaining consistent data from them.

The calibration procedure first produced a set of f(alpha) and f(psi) functions for constant probe pitch and yaw angles. These functions, through interpolation, were used to determine maps of alpha versus psi for constant f(alpha) and f(psi). This map provided a direct look-up table for alpha and psi once the angle functions were calculated.

The f(H) and f(Q) pressure functions were also interpolated and stored in look-up tables against constant values of f(alpha) and f(psi). This uniquely identified the pressure functions over the calibrated angle range.

In the current computer software implementation of the probe calibration procedure, the range of f(alpha) and f(psi) was set to consistent values for all calibrated probes. This resulted in the calibrated range of alpha and psi for each probe to be slightly different from the other probes. The variation from probe to probe was caused by small differences in the probe tips and possibly curvature of the probe shafts. The range of f(alpha) and f(psi) was determined by the performance of the worst probe of the group of probes that a calibration was to be prepared for. This limitation could be overcome by storing more detailed calibration information about each probe.

The steps taken in using the calibrations to determine the unknown local flow conditions from the known five probe pressures during a flow survey test were as follows:

1. Calculate f(alpha) and f(psi) as shown above.

2. Perform double interpolation using alpha values stored versus f(alpha) and f(psi) to get flow pitch angle.

3. Perform double interpolation using psi values stored versus f(alpha) and f(psi) to get flow yaw angle.

4. Perform double interpolation using f(H) values stored versus f(alpha) and f(psi) to get f(H) value.

5. Perform double interpolation using f(q) values stored versus f(alpha) and f(psi) to get f(q) value.

6. Calculate local dynamic pressure (q) using:
   $q = f(q) * q_0$

7. Calculate local total pressure (H) using:
   $H = f(H) * q_0 + p_0$

8. Calculate local velocity vector components using:
   U = (f(q) / (1.0 + tan(alpha)**2 + tan (psi)**2))**0.5
   V = U * tan(psi)
   W = U * tan(alpha)

   All data are in the probe axis system which can then be transformed into any desired axis system.

After the above calculations were performed, the basic flow parameters at each survey point were known.

APPENDIX C

ANALYTICAL PREDICTIONS

Developments in computational aerodynamics in the past 15 years have permitted rapid, efficient, and relatively accurate numerical solutions of complex subsonic and transonic flows. The complex aerodynamic flowfields that present computational methods are capable of analyzing are exemplified by numerical simulations for wing-mounted tractor turboprop installations with integrated nacelles and swirling slipstreams. The following paragraphs describe the computational methods which were used to assess the PTA configuration, identify potential problem areas, assess possible design modification remedies and design the LEX region.

PROPELLER/PANEL METHOD THEORY

Two primary computer programs are utilized. The first is a reliable propeller performance code, (PROPVRTX), which allows major characteristics of the slipstream to be determined. The code predicts the slipstream properties produced by a propeller of given geometry and advance ratio. The undisturbed slipstream is defined by its boundary shape and the radial distribution of the local vorticity, induced velocity, and swirl angle. The results from this code are in very good agreement with test data. The second primary code is QUADPAN, Lockheed's advanced low-order, three-dimensional panel method. QUADPAN has been widely used in the airplane design process for the analysis of geometrically complex configurations and the results have been highly reliable. For the PTA configuration, QUADPAN is uniquely qualified to provide a good geometric resolution in the intricate nacelle/inlet region. Additionally, the method is relatively insensitive to the size and shape of the panel elements because it employs an internal potential (Dirichlet) boundary condition. The solution output consists of local pressure coefficients for all surface panels, flow conditions at specified points in the external flow field, and forces and moments for the total configuration as well as for its component parts. The two codes are interfaced with the effect of the slipstream being simulated through a restatement of the surface boundary conditions to include velocity perturbations due to the propeller. The pressure on the surfaces washed by the slipstream are appropriately corrected for the pressure increase across the propeller disk. This approach is similar to one previously employed on a wing analysis program with satisfactory results.

PROPELLER EFFECTS SUBROUTINE

The effect of the propeller on the nacelle is calculated by means of a rigid slipstream model which provides the variation of axial velocity with a semi-infinite helical vortex system. The slipstream contraction is found from the application of the continuity principle to the slipstream. As there is a pressure rise through the propeller disk due to the additional energy input from the propeller, it is necessary to include this explicitly in the calculation. The pressure rise can be expressed in terms of the velocity of the fully contracted slipstream. The proper level of thrust is simulated by scaling the axial and tangential velocity distributions to correspond to a desired power coefficient Cp, and advance ratio J. The slipstream data were derived from experimental rake data for a given power coefficient and advance ratio and integrated to give an average swirl angle and average axial velocity increment. The radial distribution is kept the same for all advance ratios and the magnitude is corrected by scaling the integrated values to give the desired thrust level.

COMPUTATIONAL MODELING

The basic steps in computational aerodynamic design are: (1) the surface geometric definition, (2) aerodynamic analysis, and (3) performance evaluation. The geometry must be in a form that allows rapid access, and it must define the configuration to the appropriate degree of accuracy and detail.

The engineering analysis is carried out by either tests or by a computation of a mathematical simulation. Certain requirements for the computational codes must be met to ensure their effectiveness in the design procedure. The numerical model must adequately simulate the pertinent physics of the flow, such as the influence of the propeller slipstream and of the presence of shock waves in the transonic regime. The computer codes should be capable of handling complex geometric shapes such as the intricate nacelle-inlet region typical of a tractor turboprop configuration. The codes are also required to have a rapid turn-around time, and they must not depend on extensive manipulation of the input data to achieve a successful run. The input and output data management should preferably be automated. Performance evaluation is carried out using the acquired data to determine the extent to which the design objectives have been met and to decide what configurational changes are needed. To carry out the evaluation rapidly, automated plotting routines of the important parameters must be available and where the capability exists plotting contours and surface color shading is a big help in examining the enormous amount of information that can be extracted from these computational codes.

Surface Geometric Definition

The CATIA computer system, which was developed by Dassault of France, was used to manipulate and store the configuration geometry. CATIA, is an interactive, three-dimensional geometry system for computer-aided design and manufacturing. The system allows the rapid generation of either the complete configuration or any part of the configuration, and allows the part to be viewed as a three-dimensional drawing from any view point. A two-dimensional section at any plane can also be defined. In addition, the geometric definition can be obtained in any desired coordinate system. These features of the CATIA system permit rapid and simplified successive configuration changes.

Engineering Analysis

The QUADPAN program meets the code requirements stipulated above with the exception of calculating transonic flows with shock waves. QUADPAN allows adequate representation of the complex inlet geometry by subdividing the surface into a large number of small panels. Unfortunately, run time and run cost increase almost with the third power of the number of panels, so compromises must be made. A full model with 5,000 panels typically took 20 to 30 minutes of CPU time and 500 megabytes of high-speed disk storage on the Lockheed CRAY XMP/24 dual processor supercomputer and is currently seen as the limit of modeling density.

In order to properly simulate the physics of the flow, three flow situations require special attention. These are flow from the wing trailing edge, the jet from the engine exhaust, and the internal flow through the engine.

Aircraft Wake Treatment

In the real world, a fluid leaves from the sharp trailing edge of a wing as a result of viscous effects, creating the so-called Kutta condition, where the outflow is smooth and nearly tangent to the trailing edge. Since a panel program does not model viscosity, it is necessary to introduce a thin vortex sheet at the separation line along the trailing edge. This sheet of vorticity or wake locates the leading edge stagnation point, and so fixes the wing's circulation, or lift. Clearly, the proper treatment of the wake is of importance in a method that assumes the flow is otherwise irrotational and inviscid.

The situation for the PTA configuration is complicated by the large over-the-wing nacelle, since, in reality, a Kutta condition is also satisfied along the sharp edges of the nacelle's aft end, and around the circumference of the turboshaft engine's exhaust nozzle. To model this geometry, it was decided to approximate the aft end of the nacelle as a cone tapering down to a very long cylinder representing the engine exhaust plume. Although both the exhaust cone and exhaust plume are represented in the model as solid surfaces, the aerodynamic forces on them are not directly included as forces on the aircraft. The wing wake is then attached to the taper of the exhaust cone in a fashion similar to the treatment of the wing/fuselage juncture, sealing ultimately along the sides of the (solid) plume.

Since a theoretically ill-posed problem can result from over-specifying surface boundary conditions, the exhaust plume terminates in a disk where only the potential boundary condition is applied. The doublet strength is thus set, and the required source strength for this condition may be calculated.

Internal Flow Simulation

It is most important to be able to simulate flow into the inlet, and it should correspond to a prescribed mass flow ratio. Panel programs provide a natural means of modeling inlet flow ingestion by a simple restatement of the panel boundary condition. The QUADPAN code has the option to use permeable panels on which the normal velocity is specified by the user to correspond to the required mass flow at the engine compressor face. For incompressible flow, the velocity induced by the singularities at the control point of the permeable panel will exactly equal the specified velocity. This is not true for compressible flow, as the compressibility correction in QUADPAN assumes that the panels are nearly parallel to the freestream, and the linearization of the Prandtl-Glauert equations upon which the panel method is founded is accurate only to first order. Therefore, a panel that stands normal to freestream flow, as in the case of an inlet face or stagnation point, violates these assumptions and will have considerable leakage of fluid through its surface. Consequently, a specified velocity corresponding to a higher mass flow than that desired is input for compressible cases. The primary powerplant turbojet engine nacelles are much easier to simulate and are treated as simple flow-through ducts. Power effects can be simulated by placing a disk with a prescribed normal velocity at the engine compressor face, and treating the exhaust in the same way as the aft end of the turboshaft engine exhaust plume, with a cylindrical wake to enforce the Kutta condition.

Performance Evaluation

The configuration performance is evaluated by first determining the extent to which the design objectives have been met, and then identifying regions where aerodynamic behavior is unacceptable or improvements are desirable. To make the evaluation rapidly, automated plotting for the pertinent parameters is available. The mathematical simulation results can be displayed in four different ways: (1) pressure distribution plots, (2) velocity vector plots, (3) force and moment plots, and (4) iso-parameter plots. Pressure plots help locate adverse pressure gradient regions, as is the case due to the upwash from the propfan slipstream. Velocity-vector plots allow flowfield data at the propeller plane to be examined. Force and moment plots are essential to determine the loads on various components of the configuration. Iso-parameter plots help locate regions of unusual airflow activity in areas such as the nacelle/wing juncture, and allows an assessment of the blending to be made. Surface color shadings that represent local pressure coefficients are a big help in examining the enormous amount of information that can be extracted from these computational codes.

APPENDIX D

DRAG DATA ANALYSIS

TURBOPROP DRAG BOOKKEEPING

The prediction of full scale turboprop aircraft performance from wind tunnel data requires appropriate tests to identify the effect of installation on propeller performance and likewise the effect of the slipstream on airframe performance. Isolated propeller performance is a prerequisite to the proper identification of the various thrust and drag components such that manufacturers acting with isolated engine, propeller, and aircraft data can predict the whole aircraft performance. In the PTA Program, isolated propulsion characteristics were to be obtained by calibration of the wind tunnel propulsion hardware, i.e., the propeller and exhaust nozzle prior to complete model tests.

Thrust generated by the installed propeller is then compared to that of the isolated propeller at the same freestream Mach number, advance ratio, and blade pitch setting. Propeller performance is extremely sensitive to blade pitch setting, and because it is so difficult to accurately repeat pitch setting for the isolated propeller and the installed configuration, three propfan rotor sets were employed with different blade-pitch angles fixed and undisturbed throughout the tests.

The drag polars for each specific configuration include interference effects due to the installation of the propulsion unit. The effective drag coefficient is defined as:

$$C_{D_{EFF}} = C_{D_{BAL}} - C_{t_{ISO}} - C_{t_{JET}}$$

where the isolated propeller thrust, C_t , is found from the isolated propeller performance test at the same freestream Mach number, advance ratio, and blade pitch setting. C_t is the thrust due to the exhaust and is obtained from the exhaust nozzle calibration.

Propeller interference drag is obtained for the given configuration by subtracting the propeller-off drag from the effective drag:

$$C_{D_{PID}} = C_{D_{EFF}} - C_{D_{POFF}}$$

PRESENT WIND TUNNEL DRAG DATA ANALYSIS

During the PTA wind-tunnel testing, dynamic vibrations with the isolated propeller/nacelle configuration precluded the calibration of the 1/9-scale propeller at Mach numbers above 0.4; thus, the effective drag coefficient cannot be obtained. The wind tunnel data is reduced using the hub-balance thrust measurement to obtain the model propeller-on drag. This is defined as follows:

$$C_{D_{PO}} = C_{D_{BAL}} - C_{t_{HB}} - C_{t_{JET}}$$

The propeller-on drag is the drag of the configuration with the propeller thrust ($C_{t_{HB}}$), as measured by the hub-balance, and the jet thrust ($C_{t_{JET}}$) removed. $C_{D_{PO}}$ has all the effects of the slipstream on the wing which includes a thrust term resulting from the derrotation of the slipstream and scrubbing drag due to the additional dynamic pressure within the slipstream. At high Mach numbers, the slipstream alters the shock wave pattern on the wing and the resultant increment in force is dependent on the mutual transonic interactions which may or may not be favorable.

In the reduction of the thrust/drag data for the PTA 1/9-scale model, a number of data sources were utilized. These included the correlation of the balance temperature correction, internal drags for the Spey and powered nacelles, propfan drive motor horsepower correlation, unpowered model drag polar, and finally, force components for the full-up PTA airplane model running under power. Additional components, such as tares and base drag components, were included where appropriate.

INTERNAL DRAG, SPEY NACELLES

The Spey nacelles for the PTA model were instrumented more than is normally done for flow-through nacelles on a wind tunnel model. In addition to the statics near the exit, there were four rakes with three probes each located at the simulated compressor face. These were designed to measure possible flow distortion caused by the propfan nacelle slipstream.

An internal drag computation procedure for the Spey nacelles was developed and allows for inlet total pressures different from freestream. Entry total pressures were obtained by working forward from the rakes assuming the only duct loss to be that of internal friction. A duct pressure loss factor was included for the effect of the rakes themselves. The cosine effect on the recovered exit thrust produces a slight angle-of-attack (Alpha) and nacelle incidence effect on internal drag and there is also a lift effect which is a relatively small percentage of the total lift, but is nevertheless a significant number. Both the internal drag and the internally generated incremental lift increments have been computed.

INTERNAL DRAG, POWERED NACELLE

The inlet for the powered nacelle is followed by flow-through duct with a fairly complex internal shape. It has a 5-tube total pressure rake assembly at the inlet entry to measure the total pressure. Since the inlet is located behind the prop, the total temperature as well as the total pressure of the stream is affected. The internal drag computation for this nacelle includes this temperature change. The procedure also accounts for friction, expansion, and turning loss, which occurs inside the duct.

APPENDIX E

SYMBOLS

AF	Balance axial force
BL	Butt-Line - lateral position measured from aircraft centerline
C_D	Drag coefficient
C_1	Rolling moment coefficient
C_L	Lift coefficient
C_m or C_M	Pitching moment coefficient
C_{M_0}	Pitching moment coefficient at zero lift
C_n	Yawing moment coefficient
C_p	Pressure coefficient
$C_p{}^*$	Pressure coefficient corresponding to Mach 1.0
C_P	Power coefficient
C_t	Thrust coefficient
C_y	Side force coefficient
d	Prop diameter
D	Drag
FRL	Fuselage reference line
H	Total pressure
H_0	Freestream total pressure
HP	Horsepower
J	Propeller advance ratio, $V_0/\omega d$
L	Lift
M	Mach number
M_0	Freestream Mach number
MAC	Mean aerodynamic chord

SYMBOLS (CONTINUED)

NF	Balance normal force
NT	Nacelle Incidence Angle
PM	Balance pitching moment
p	Static pressure
p_0	Freestream static pressure
q	Dynamic pressure
q_0	Freestream dynamic pressure
RM	Balance rolling moment
R_η	Neutral point
SF	Balance side force
SQRT	Square root
TC or T_C	Thrust coefficient
U	Axial velocity in propeller coordinates
V	Lateral velocity in propeller coordinates
W	Vertical velocity in propeller coordinates
V_0	Freestream velocity
V_R	Resultant velocity
X/C	Chordwise wing position $\left(\frac{\text{distance from leading edge}}{\text{wing chord}}\right)$
X/L	Lengthwise nacelle position $\left(\frac{\text{distance from nacelle stations}}{\text{zero nacelle length}}\right)$
YM	Balance yawing moment

Greek Symbols

α	Aircraft angle of attack
α_t	Propeller angle of attack
β	Aircraft yaw angle
B	Propeller blade pitch angle

SYMBOLS (CONTINUED)

δ_A	Aileron deflection
δ_R	Rudder deflection
δ_S	Stabilizer deflection
η	Spanwise wing station in percent of semi-span dimension
ψ	Azimuth angle in propeller plane
ω	Propeller rotational speed

REFERENCES

1. Hackett, J. E., C. G. Phillips, and D. E. Lilley, "Three-Dimensional Wake Flow Measurements for a Wing and a Bluff, Car-Like Body," Lockheed-Georgia Company, LG81ER0201, Submitted to the Georgia Institute of Technology, August 1981.

2. CATIA APAR Coordinator, IBM Corporation, "Computer-Graphics Aided Three-Dimensional Interactive Application (CATIA) User Manual, Program Numbers 5796-PQG, 5796-PQH, 5796-PQJ, and 5796-PQL, Second Edition," SH20-2629-4, March 1984.

3. Youngren, H. H., E. E. Bouchard, R. M. Coopersmith, and L. R. Miranda, "Comparison of Panel Method Formulations and Its Influence on the Development of QUADPAN, an Advanced Low Order Method," AIAA-83-1827, AIAA Applied Aerodynamics Conference, 3-15 July 1983.

4. Aljabri, A. S., and J. M. Swearengen, "Analysis of Mach Number 0.8 Turboprop Slipstream Wing/Nacelle Interactions," NASA CR166419 (prepared by Lockheed-Georgia Company and issued as LG82ER0169), December 1982.

5. Aljabri, A. S., and B. H. Little, Jr., "High Speed Wind Tunnel Tests of the PTA Aircraft," SAE 861744, Aerospace Technology Conference and Exposition, 13-16 October 1986.

6. Aljabri, A. S., and C. A. Hughes, "Wind Tunnel Investigation of Propeller Slipstream Interaction with Nacelle/Wing/Flap Combinations," AGARD Paper 21, presented to AGARD Symposium on Aerodynamics and Acoustics of Propellers, Toronto, Canada, 1-4 October 1984.

PRECEDING PAGE BLANK NOT FILMED

NASA
National Aeronautics and Space Administration

Report Documentation Page

1. Report No. NASA CR-182121	2. Government Accession No.	3. Recipient's Catalog No.

4. Title and Subtitle PROPFAN TEST ASSESSMENT TESTBED AIRCRAFT STABILITY AND CONTROL/PERFORMANCE 1/9-SCALE WIND TUNNEL TESTS	5. Report Date May 1988
	6. Performing Organization Code
7. Author(s) B. H. Little, Jr., K. H. Tomlin, A. S. Aljabri, and C. A. Mason	8. Performing Organization Report No. LG88ER0056
	10. Work Unit No.
9. Performing Organization Name and Address Lockheed Aeronautical Systems Company 86 South Cobb Drive Marietta, Georgia 30063	11. Contract or Grant No. NAS3-24339
	13. Type of Report and Period Covered Contractor Report Task 7 Final
12. Sponsoring Agency Name and Address National Aeronautics and Space Administration Lewis Research Center Cleveland, Ohio 44135-3191	14. Sponsoring Agency Code

15. Supplementary Notes

Project Manager, John B. Whitlow, Propfan Test Assessment Project
NASA Lewis Research Center

16. Abstract

One-ninth scale wind tunnel model tests of the Propfan Test Assessment (PTA) aircraft were performed in three different NASA facilities. Wing and propfan nacelle static pressures, model forces and moments, and flow field at the propfan plane were measured in these tests. Tests started in June 1985 and were completed in January 1987.

These data were needed to assure PTA safety of flight, predict PTA performance, and validate analytical codes that will be used to predict flow fields in which the propfan will operate.

17. Key Words (Suggested by Author(s)) Aerodynamics Wind Tunnel Testing Propfan Aircraft Design	18. Distribution Statement Unclassified - Unlimited Subject Category 05

19. Security Classif. (of this report) Unclassified	20. Security Classif. (of this page) Unclassified	21. No of pages	22. Price*

NASA FORM 1626 OCT 86

*For sale by the National Technical Information Service, Springfield, Virginia 22161